successful application of MQCM based sensor. QCMs in MQCM platform are selectively deposited with different gas-sensitive layers. Most gas-sensing materials employed in MQCM are organic and polymeric materials, which can physically adsorb gases at room temperature. Several gas sensor arrays based on conventional MQCM structure have been reported [71]. For example, a 10 MHz MQCM selectively coated with three sensing films including ionic liquid butylmethylimidazolium camphorsulfonate (BMICS), ionic liquid butylmethylimidazolium tetrafluoroborate ($BMIBF_4$) and poly(vinyl ferrocene) (PVF) by solvent casting are developed for classification and detection of humidity (water vapor) and volatile organic compounds (VOCs) including ethanol, dichloromethane (CH_2Cl_2) and hexane. The study results show that the sensors with different coatings exhibit different frequency shift characteristics towards various analytes. For example, BMICS is highly sensitive to ethanol while PVF is more sensitive to CH_2Cl_2. From the sensing patterns, VOCs and humidity can be well discriminated by the sensor array with LDA analysis.

Another interesting instance is a 10 MHz QCM gas sensor array coated with Poly-vinyl-pyrrolidon (PPy) and DM-189 organic precursor material for humidity and ammonia sensing [66]. A remarkable feature of this QCM array is that it has integrated heater for gas sensing in temperature modulation (TM) mode. In TM mode, gas adsorption on QCM is purged by rapid heating over a short period and gas sensing response is obtained from the frequency difference between gas-sensing and gas-purging periods. The advantages of this scheme are fast recovery and possible elimination of reference QCM. However, it requires additional heater and can suffers from short life time due to rapid heating and cooling. Moreover, the magnitude of resonance frequency shift from conventional MQCM gas sensor array is only on the order of hundreds of Hertz, which is considered small and not sufficient for many applications involving much lower vapor concentration.

Several strategies have been employed to enhance sensitivity of MQCM gas sensor array. Firstly, MQCM can be designed to operate at high resonance frequency in order to increase mass-sensitivity for gas molecule detection. This scheme is very effective because the resonance frequency shift is proportional to the square of resonance frequency. For instance, an odor sensor based on MQCM utilizing plano-inverted-mesa structure has been demonstrated [75]. QCMs are designed to operate a high frequency of ~21 MHz and are coated with three amphiphilic organic materials, including dimyristylphosphatidylchorine (DMPC), dimyristylphosphatidylserine (DMPS) and cholesterol by solvent casting. It has shown high sensitivity and ability to discriminate six kinds of odorants including ethanol, methanol, benzene, methyl-benzene, CH_2Cl_2 and CH_3COCH_3.

Another important strategy is to use highly sensitive gas-sensing films based on nanostructured materials. A wide variety of nanomaterials have been applied to QCM gas sensor array [97,98]. Following highlights some interesting examples of nanostructure materials integrated on QCM gas sensor arrays. Mesoporous silica hybrids are interesting nanostructure materials, which have successfully been applied to QCM gas sensor array. Conventional MQCM are coated with unmodified mesoporous silica and mesoporous silica hybridized with β-cyclodextrin (β-CD) and triphenylphosphine (PPh3) for alcohol and benzene discrimination [67]. The results show that nanohybrid structures provide enhanced sensitivity while β-CD and PPh3-silica composites are very effective for discrimination between benzene and alcochol.

Carbon nanotubes (CNTs) are one of the most widely studied nanomaterials with promising properties for gas-sensing [99–102]. They have been applied to several QCM and MQCM gas sensing platforms. An interesting example of CNTs applications is the use of isolated single walled (SW) CNTs on QCM sensor array for highly sensitive detection of small gas molecules including helium, nitrogen, oxygen, argon and sulfurhexafluoride (SF_6) [76]. The MQCM has plano-inverted-mesa structure with mesa thickness of ~56 μm and SW-CNTs are coated on gold electrodes by spray coating of SW-CNTs in NMP (N-methyl-2-pyrrolidinone). It has been demonstrated that SW-CNTs provide highly sensitive detection of small gas molecules with large frequency and *Q*-factor changes and they are logarithmically proportional to the mass of gas molecules. *Q*-factor change is attributed to viscoelastic dissipation of non-rigidly adsorbed gas molecules around CNT walls.

Molecularly imprinted polymer (MIP) is a class of nanostructured organic materials, which can be designed as analyte receptors with various specificities [2,103]. MIPs are synthesized by polymerization of monomers in the presence of analytes acting as templates, which are subsequently removed by evaporation leaving cavities within the polymer matrix. Different analytes will distinctively bind to molecular cavities, resulting in desired selectivities. This approach can be used to sensitively distinguish similar isomers with sufficient selectivity. MIPs have been applied to MQCM to sense a group of terpenes, which are biogenic volatile compounds emanating from herbaceous vegetation [74]. Six MIPs are synthesized from six terpenes templates including α-pinene, limonene, eucalyptol, β-pinene, terpinene and estragole with polystyrene (PS) and divinylbenzene (DVB) copolymer matrix. MIPs are synthesized by mixing terpene templates to styrene functional monomer, DVB cross-linker, AIBN radical initiator and diphenylmethane. The mixtures are polymerized for 40 min at 70 °C and then selectively deposited on electrodes by spin coating with photoresist patterning. It has been shown that each analyte shows maximum selectivity towards its corresponding template. In addition, it shows selectivity between isomeric compounds, α-pinene and β-pinene. These selectivity patterns are successfully analyzed by a neural network methodology.

MQCM based e-noses have recently been demonstrated in real-world applications. For instance, MQCM based enose has been used for plant-degradation monitoring [104]. MQCM comprises six QCM electrode coated with six different polymer and MIP layers that can distinctively detect humidity, alcohol, ester and terpene compounds. It has been used to monitor VOCs emitted from grass and pine composting processes. The e-nose system has successfully provided real time data of VOCs compositions, which have been validated by gas chromatography mass-spectrometry (GC–MS) and given direct insight into the differences between grass and pine composting batches, which are beneficial for composting process control. This demonstrates that MQCM based e-noses should be potential for other real world applications such as environmental monitoring, industrial/agricultural gas monitoring, food/drink quality control, detection of emitted diseases, etc. Nevertheless, more experimental work needs to be done to realize these target applications.

5.2. Chemical sensor array

Chemical sensor array and electronic tongue are devices for multiple detection of chemical and chemical compound. In chemical sensor array, QCMs are coated with different chemical receptors, which absorbed analyte, resulting in negative resonance frequency shift. In general, chemical receptors are not specific and several chemical receptors are normally used to identify and quantify an analyte. For instance, flow injection MF-QCM for detection of toluene has been reported [7]. In this system, three organic materials including polystyrene, amyl-calix [8] arene and β-cyclodextrine are used as toluene receptors. The receptors are coated using electrostatic spray or airbrush techniques. Resonance frequency and equivalent resistance of QCMs are monitored during flow injection of toluene in water stream. It is found that polystyrene and amyl-calix [8] arene give similar response while β-cyclodextrine

exhibits an unusual response. For the first two sensors, the resonance frequencies decrease whereas the equivalent resistances increase upon toluene injection. The frequency decrease is due to mass accumulation caused by the penetration of toluene into the coating while the increased resistance indicates that acoustic dissipation decreases due to the reduced shear modulus of the surface. However, the frequency shift is relatively lower whereas the resistance increase is much larger and response is notably faster for QCM coated with amyl-calix [8] arene. For β-cyclodextrine case, the frequency temporarily increases and decreases while equivalent resistance decreases strongly and steadily upon toluene and water injections. This indicates that toluene is not rigidly absorbed into β-cyclodextrine unlike other coating cases. The difference in response of QCMs with different coating can be used to uniquely identify and determine the concentration of analyte. However, it is known that the responses in liquid are considerably more complicated than those in gas phase. The behaviors of QCM based chemical sensor are more complex due to contribution by viscoelastic properties of both sensing film and solution. In addition, liquid-film interaction such as swelling can further complicate the sensing response. Thus, the analysis of response requires sophisticated methods that may require human intervention and there is no standard formulation and method for this purpose. Presently, there has been no report of MQCM based electronic tongue due to complicated response and interference in liquid. Owing to its wide real world applications such as food, drink and medicine analysis, MQCM based electronic tongue is a challenging topic that is currently under exploration.

5.3. Biosensor array

Research on QCM for biosensor has grown steadily by increasing health care, agricultural and security needs. Various classes of QCM biosensors including immune [27,105–107], enzyme [108,109], nucleic acid [83,110,111] and cell [112,113] based sensors have been presented. Biosensor arrays based on simple combination of QCMs have also been developed for multiple and simultaneous detection of bioanalytes of the same or different classes [114,115]. However, this scheme requires large sample consumption and environmental control among different sensors is difficult. MQCM technology is thus a key to realize efficient miniaturized biosensor array. MQCM Biosensor array can be achieved by the selective application of different functional bioreceptors atop various QCM elements to provide molecular hooks or active sites for a range of analytes of interest. In addition, multi-sensitivity and multi-dynamic-range QCM platforms allow simultaneous detections of biological species of different sizes ranging from virus, DNA, protein to complex arrays of biomacromolecules and large cells on one chip.

Functionalization of biological receptors on QCM's gold electrodes are most commonly done by the use of self-assembled monolayer (SAM) techniques. SAMs of alkanethiols are typically formed on gold by adsorption from dilute solutions [116–119]. The general structure of alkanethiols is $HS(CH_2)nX$, where n is an integer and typically varies between 14 and 16 in. long chain molecules, and X is terminal group in a series including $-CH_3$, $-CH_2OH$, $-CO_2H$, $-CO_2CH_3$, $-CONH_2$ and more complex functional groups [77]. The thiol group (SH) binds spontaneously to gold with a relatively strong binding energy approximately of 120 kJ mol^{-1}, producing very stable and uniform layer. Terminal groups of SAMs are selected to provide match binding to target species or their biological receptors.

Recently, a fair number of studies on MQCM based biosensor arrays have been reported [72,77,79]. However, most reports have only demonstrated functionalizations of a few distinct biological receptors on one chip and detection of a few biological analytes. For instance, 8-pixel QCM array for bovine serum albumin (BSA) and avidin detections have been reported [79]. Some pixels are selectively functionalized with 3,3′-dithiobis (sulfosuccinimidylpropionate) (DTSSP) for avidin detection while others are masked using photoresist and octadecanethiol (ODT) SAMs are subsequently functionalized for BSA detection. The resonance frequency shifts of 460 and 76 Hz are obtained from selectively functionalized QCMs for 10 mg mL^{-1} BSA and 1 mg mL^{-1} avidin, respectively.

A MQCM based biosensor has also been reported for yeast cell detection utilizing MIP methodology [72]. Yeast-sensitive receptors are generated by molecular imprinting of single and duplex yeast cells in polyurethane films. Synthetic *Saccharomyces cerevisiae* yeast cells is blended with 4,4′-diisocyanato diphenylmethane, bisphenol and phloroglucinol prepolymer mixture at 70 °C and spun on conventional 10 MHz MQCM electrodes. The mixture is then polymerized over night and yeast templates are removed by ultrasonication in water. Yeast cells are detected by flow injection analysis and flow injection response to a single yeast cell solution of MQCM with four different MIP coated electrodes. It is demonstrated that MIP imprinted with single and duplex cells has strong response to their respective yeast cells while two non-imprinted electrodes and the one imprinted with different cell type give only a minor frequency decrease. Thus, MIP layers exhibit very good selectivity for yeast cell detection.

There have been several efforts to develop MQCM based immunosensors, which immobilized several antibodies for detection of various species. Nevertheless, no study succeeded in establishing the MQCM based immunosensors because of intricate QCM sensing response and ineluctable interference among channels operating in real biological solutions [120]. QCM based biosensor's responses are more intricate than that of chemical sensor due to the complex nature of biological receptors and analytes. In addition, biological samples such as antigen-antibody and cells are often formed heterogeneously on electrode surface, making response analysis even more complicated. Thus, a lot more work on MQCM based biosensors including selective functionalization of micro-QCM array, inference reduction, advanced analysis and characterizations of multiple biosensing in real environment need to be done to realize effective biosensor arrays for real world applications including clinical diagnosis, agricultural, horticultural, veterinary and microbial contamination analyses and other biomedical applications.

5.4. Miscellaneous applications

In addition to gas, chemical and biosensor arrays, several specific and special applications for MQCM have been proposed. Photocatalytic reaction measurement is a new potential application for QCM [121,122]. Photocatalytic materials have attracted great attention due to their ability to decompose organic pollutants under near UV irradiation and photocatalytic activity has normally been measured by monitoring the color degradation of dyes on photocatalytic materials [123]. It is desirable to study photocatalytic effect without addition of dye molecules. QCM can be used to measure the mass change effects caused by photocatalytic reactions with no dye molecule. However, QCM is sensitive to decomposition reaction's conditions including UV radiation intensity and temperature and such dependence must be effectively compensated. Recently, dual QCM scheme based on antiparallel coupled resonator (ACR) structure (ACR is a new type of thickness field excited QCM, which has two electrodes one side of AT-cut quartz and a conducting layer on the other side [73]) has successfully been applied for photocatalytic activity of methylene blue (MB) measurement [81]. It has been demonstrated that the environmental effects induced by UV irradiation and gradual temperature changes can be well compensated by the referenced QCM on the same quartz substrate. In addition,

Table 2
Summary of MQCM platforms and applications.

MQCM platforms	Reported structures	Application areas	Potential applications	Reported applications
Static multichannel detector	Conventional QCM Plano-inverted-mesa QCM	Multi-component analysis with selective receptors Multi-component analysis with low selectivity receptors for quantification of component Multi-component analysis with low selectivity receptors for mixture recognition	Electronic noses Chemical sensor array Electronic tongues Biosensor array Multi-photocatalytic measurement Multi-EQCM	Electronic noses: VCO and humidity detection [66,67,71,74–76,104] Biosensor array: Avidine and BSA detection [79]
Series MQCM as a multichannel detector for the flow injection analysis	Conventional QCM Plano-inverted-mesa QCM	High throughput multi-component analysis		Chemical sensor array: toluene detection [7] Biosensor array: yeast cell detection [72]
Multifrequency QCM for multi-sensitivity and multi-dynamic range detection	Plano-inverted-mesa QCM	Multi-sensitivity detection Multi-dynamic range detection Multi-component analysis		Chemical sensor array: Toluene [7]

the resulting frequency shift versus irradiation intensity of UV light exhibits a linear relationship, making MQCM highly practical for this application. This scheme should be extended to multiple simultaneous activity measurements of several photocatalytic materials.

A large number of applications in the field of electroanalytical chemistry of single EQCM have been reported [124,125]. These include studies of formation, viscoelastic behavior, and ion/solute transport properties of electropolymerized films. For example, EQCM has been used to monitor the electropolymerization of polypyrrole and to investigate the film evolution from elastic behavior early in the polymerization process to visoelastic, energy dissipating properties in the subsequent synthesis of a thicker film. The details of ion and solvent transport between the film and solution can be sensitively followed through mass change related to concentration changes in any small diffusing species that migrate in the film. The diverse applicability should be extended to multiple EQCMs based on MQCM structure so that multiple studies can be simultaneously performed. However, there has been no report of multi-EQCMs based on MQCM structure. In EQCM array systems, channels of MQCM can be used as different working electrodes operating at distinct applied potentials and one of channel may be used as a counter electrode. However, strong electric and acoustic interference and other problems in multi-EQCM system are still major barriers for the development. Therefore, multi-EQCMs based on MQCM platform are one of challenging topics that should be further explored.

Table 2 summarizes the MQCM platforms, reported structures, application areas, potential and reported applications and Table 3 lists sensing materials, target analytes, sensitivity and sensing range of reported MQCM based sensors. It can be seen that only conventional MQCM and plano-inverted-mesa MQCM structures have been applied to various MQCM platforms. This should be due to the fact that conventional MQCM can be most easily implemented while plano-inverted-mesa structure provides numerous advantages in terms of interference, resonance frequency and mass sensitivity and it is applicable to flow injection and multi-frequency/multi-dynamic-range platforms. Moreover, it can be seen that among implemented MQCM potential applications, only electronic noses have been most successfully demonstrated in laboratories as well as real world applications while chemical/biosensor arrays have only been demonstrated to a few examples of analytes. From Table 3, sensing materials are mostly organics or polymer, which sometimes hybrid with inorganic nanomaterials, while only limited groups of target analytes have been studied over some

Table 3
Summary of sensing parameters of reported MQCM based sensors (up to September 2010).

MQCM application	Sensing materials	Target analytes	Sensitivity	Sensing range	Ref.
Electronic noses	CPH, DM 189, PPy	Ammonia, humidity	~1, ~0.1 Hz ppm^{-1}	0-1000, 0-20000 ppm	[66]
	β-CD-, PPh_3-Meso silica	Benzene, alcohol	0.05-0.09, 0.01-0.02 Hz ppm^{-1}	0-5000 ppm	[67]
	BMICS, BMIBF4, PVF	Ethanol, CH_2Cl_2, hexane, humidity	0.2-1, 2-6, 0.1-1, 0.1-0.5 Hz %$^{-1}$	10%	[71]
	MIP: α-Pinene, β-Pinene Limonene, Terpinene, Estragole, Eucalyptol	α-Pinene, β-pinene, limonene, terpinene, estragole, eucalyptol	n/a	n/a	[74]
	DMPC, DMPS, cholesterol	Ethanol, methanol, benzene, methyl-benzene, CH_2Cl_2, CH_3COCH_3	n/a	n/a	[75]
	PVA, PS, PU, MIP:PS/DVB	Alcohol, limonene, ethyl acetate, humidity	n/a	0–300 ppm	[104]
	SW-CNTs-NMP	Helium, nitrogen, oxygen, argon, SF_6	50–100 Hz amu^{-1}	4–100 amu	[76]
Chemical sensor array	PS, amyl-calix[8]arene, β-CD	Toluene	10–100 Hz ppm^{-1}	400 ppm	[7]
Biosensor array	DTSSP, ODT	Avidine, BSA	30–70 Hz (mg mL)$^{-1}$	0–1 mg mL^{-1}	[79]
	MIP: yeast cell	Yeast cell	~1 cell mL^{-1}	5×10^5 cell μL^{-1}	[72]

CPH: cryptophane, PPy: β-CD:β-cyclodextrine, PPh_3: triphenylphosphine, BMICS: ionic-liquid-butylmethylimidazolium-camphorsulfonate, BMIBF4: ionic-liquid butylmethylimidazolium-tetrafluoroborate, PVF: polyvinyl-ferrocene, DMPC: dimyristylphosphatidylchorine, DMPS: dimyristylphosphatidylserine, PVA: polyvinyl-alcohol, PS: polystyrene, PU: polyurethane, MIP: molecularly imprinted polymer, DVB: divinylbenzene, SW-CNTs-NMP, DTSSP: 3,3′-dithiobis (sulfosuccinimidylpropionate), ODT: octadecanethiol, BSA: bovine serum albumin, amu: atomic mass unit.

reported sensing ranges and sensitivities. Furthermore, electronic tongue, multi-biosensor and multi-EQCM have not yet been developed. Therefore, most MQCM based sensors require much further development before they can be routinely used in laboratories and real world applications.

6. Conclusion

In conclusion, MQCM technology has been extensively reviewed. The theoretical/experimental analysis, design, acoustic interference and other problems of conventional MQCM's have been discussed. Various MQCM schemes devices based on modification of quartz substrate structure including mesa, convex and *x*-axis inversion structures are then presented. Among these, plano-inverted-mesa has been the most frequently reported because it simultaneously offers low interference, high resonance frequency, high mass sensitivity and compatibility with flow injection and multi-frequency system. Next, MQCM sensing platforms comprising static multichannel detector, series MQCM as a multichannel detector for the flow injection analysis, multi-frequency QCM for multi-sensitivity/multi-dynamic range detection are described. The combination of multi-frequency QCM and flow injection analysis platforms are seen to be most promising for various application areas. Lastly, potential and prospective MQCM applications are illustrated. Electronic noses is found to be the most successful application with real world demonstration while electronic tongue, biosensor array and other applications are still at an early stage of development. Therefore, MQCM is a relatively new and promising research area worthy for further exploration.

Acknowledgement

This work is supported by National Electronics and Computer Technology Center (NECTEC) under QCM biosensor project and Thailand Research Fund (TRF). A.T. would like to acknowledge TRF for career developing fund.

References

[1] K.A. Marx, Biomacromolecules 4 (2003) 1099–1120.
[2] B. Wyszynski, T. Nakamoto, IEEJ Trans. Elec. Electron. Eng. 4 (2009) 334–338.
[3] J.F. Alder, J.J. McCallum, Analyst 108 (1983) 1169–1189.
[4] Y. Uludag, S.A. Piletsky, A.P.F. Turner, M.A. Cooper, FEBS J. 274 (2007) 5471–5480.
[5] X. Su, F.T. Chew, S.F.Y. Li, Anal. Sci. 16 (2000) 107–114.
[6] K.D. Pavey, Expert Rev. Mol. Diagn. 2 (2002) 173–186.
[7] J. Rabe, S. Büttgenbach, J. Schröder, P. Hauptmann, IEEE Sens. J. 3 (2003) 361–368.
[8] G. Sauerbrey, Z. Phys. 155 (1959) 206–222.
[9] K. Keiji Kanazawa, J.G. Gordon Ii, Anal. Chim. Acta 175 (1985) 99–105.
[10] M.D. Ward, E.J. Delawski, Anal. Chem. 63 (1991) 886–890.
[11] Z. Lin, C.M. Yip, I. Scott Joseph, M.D. Ward, Anal. Chem. 65 (1993) 1546–1551.
[12] M. Rodahl, B. Kasemo, Sens. Actuators B 37 (1996) 111–116.
[13] H. Muramatsu, E. Tamiya, I. Karube, Anal. Chem. 60 (1988) 2142–2146.
[14] M. Rodahl, F. Höök, C. Fredriksson, C.A. Keller, A. Krozer, P. Brzezinski, M. Voinova, B. Kasemo, Faraday Discuss. 107 (1997) 229–246.
[15] M. Penza, G. Cassano, P. Aversa, F. Antolini, A. Cusano, A. Cutolo, M. Giordano, L. Nicolais, Appl. Phys. Lett. 85 (2004) 2379–2381.
[16] M. Matsuguchi, T. Uno, Sens. Actuators B 113 (2006) 94–99.
[17] L.C. Brousseau Iii, T.E. Mallouk, Anal. Chem. 69 (1997) 679–687.
[18] B. Ding, J. Kim, Y. Miyazaki, S. Shiratori, Sens. Actuators B 101 (2004) 373–380.
[19] X. Wang, J. Zhang, Z. Zhu, Appl. Surf. Sci. 252 (2006) 2404–2411.
[20] M.D. Ward, in: I. Rubenstein (Ed.), Physical Electrochemistry: Principles Methods & Applications, Marcel Dekker, New York, 1995.
[21] N. Asakura, T. Kamachi, I. Okura, Res. Chem. Intermed. 32 (2006) 341–355.
[22] M. Lukaszewski, A. Czerwhiski, J. Electroanal. Chem. 606 (2007) 117–133.
[23] C.K. O'Sullivan, G.G. Guilbault, Biosens. Bioelectron. 14 (1999) 663–670.
[24] A. Janshoff, H.J. Galla, C. Steinem, Angew. Chem. Int. Ed. 39 (2000) 4004–4032.
[25] J. Wegener, A. Janshoff, L. Steinem, Cell Biochem. Biophys. 34 (2001) 121–151.
[26] B.A. Čavić, G.L. Hayward, M. Thompson, Analyst 124 (1999) 1405–1420.
[27] F. Ricci, G. Volpe, L. Micheli, G. Palleschi, Anal. Chim. Acta 605 (2007) 111–129.
[28] P.D. Skottrup, M. Nicolaisen, A.F. Justesen, Biosens. Bioelectron. 24 (2008) 339–348.
[29] E.R. Hirst, Y.J. Yuan, W.L. Xu, J.E. Bronlund, Biosens. Bioelectron. 23 (2008) 1759–1768.
[30] T.S. Hug, Assay Drug Dev. Technol. 1 (2003) 479–488.
[31] V.E. Bottom, Introduction to Quartz Crystal Unit Design, Van Nostrand Reinhold, New York, 1982.
[32] S. Bruckenstein, A. Fensore, Z. Li, A.R. Hillman, J. Electroanal. Chem. 370 (1994) 189–195.
[33] S. Bruckenstein, M. Michalskl, A. Fensore, L.I. Zhufen, A.R. Hillman, Anal. Chem. 66 (1994) 1847–1852.
[34] G.C. Dunham, N.H. Benson, D. Petelenz, J. Janata, Anal. Chem. 67 (1995) 267–272.
[35] T. Uno, Frequency Control Symposium, 1996, in: 50th, Proceedings of the 1996 IEEE International, 1996, pp. 526–531.
[36] S. Berg, D. Johannsmann, Anal. Chem. 73 (2001) 1140–1145.
[37] F. Shen, K.H. Lee, S.J. O'Shea, P. Lu, T.Y. Ng, IEEE Sens. J. 3 (2003) 274–281.
[38] T. Tatsuma, Y. Watanabe, N. Oyama, K. Kitakizaki, M. Haba, Anal. Chem. 71 (1999) 3632–3636.
[39] V.N. Hung, T. Abe, P.N. Minh, M. Esashi, Appl. Phys. Lett. 81 (2002) 5069–5071.
[40] F. Lu, H.P. Lee, P. Lu, S.P. Lim, Sens. Actuators A 119 (2005) 90–99.
[41] S.J. Martin, V.E. Granstaff, G.C. Frye, Anal. Chem. 63 (1991) 2272–2281.
[42] R.W. Cernosek, S.J. Martin, A.R. Hillman, H.L. Bandey, IEEE Trans. Ultrason. Ferroelectr. Freq. Control 45 (1998) 1399–1407.
[43] H.F. Tiersten, Linear Piezoelectric Plate Vibrations, Plenum, New York, 1969.
[44] F. Shen, P. Lu, IEEE Trans. Ultrason. Ferroelectr. Freq. Control 51 (2004) 249–253.
[45] R.D. Mindlin, P.C.Y. Lee, Int. J. Solids Struct. 2 (1966) 125–139.
[46] Y.-K. Yong, J.T. Stewart, J. Detaint, A. Zarka, B. Capelle, Y. Zheng, IEEE Trans. Ultrason. Ferroelectr. Freq. Control 39 (1992) 609–617.
[47] L. Li, T. Abe, M. Esashi, Proceedings of the IEEE International Conference on Micro Electro Mechanical Systems (MEMS) (2005) 327–330.
[48] A. Ishizaki, H. Sekimoto, D. Tajima, Y. Watanabe, Proceedings of the IEEE Ultrasonics Symposium 2 (1995), 913–916.
[49] S. Goka, H. Sekimoto, Y. Watanabe, Proceedings of the Annual IEEE International Frequency Control Symposium 1 (1999) 441–444.
[50] K. Hirama, Y. Aoyama, M. Naito, Jpn. J. Appl. Phys., Part 1 36 (1997) 6432–6436.
[51] K.M. Lakin, G.R. Kline, K.T. McCarron, Proceedings of the Annual IEEE International Frequency Control Symposium, (1995), 827–831.
[52] H. Sekimoto, S. Goka, Y. Watanabe, IEEE Trans. Ultrason. Ferroelectr. Freq. Control 48 (2001) 1302–1307.
[53] C. Kreutz, J. Lörgen, B. Graewe, J. Bargon, M. Yoshida, Z.M. Fresco, J.M.J. Frèchet, Sensors 6 (2006) 335–340.
[54] S. Goka, H. Sekimoto, Y. Watanabe, Proceedings of the Annual IEEE International Frequency Control Symposium, (2000) 397–400.
[55] H. Iwata, IEEE Trans. Ultrason. Ferroelectr. Freq. Control 51 (2004) 1026–1029.
[56] H. Iwata, IEEE Trans. Ultrason. Ferroelectr. Freq. Control 52 (2005) 1435–1442.
[57] F. Shen, S.J. O'Shea, K.H. Lee, P. Lu, T.Y. Ng, IEEE Trans. Ultrason. Ferroelectr. Freq. Control 50 (2003) 668–675.
[58] F. Shen, P. Lu, S.J. O'Shea, K.H. Lee, Sens. Actuators A 111 (2004) 180–187.
[59] S. Goka, K. Tamura, H. Sekimoto, Y. Watanabe, T. Sato, Proceedings of the Annual IEEE International Frequency Control Symposium, (2003) 694–697.
[60] Y. Nagaura, K. Kinoshita, S. Yokomizo, Frequency Control Symposium and Exhibition, 2000, in: Proceedings of the 2000 IEEE/EIA International, 2000, pp. 255–259.
[61] L. Li, T. Abe, M. Esashi, Sens. Actuators A 114 (2004) 496–500.
[62] Z. Nagaura, K. Nagaura, K. Imani, Y. Nagaura, Frequency Control Symposium and Exposition, 2005, in: Proceedings of the 2005 IEEE International, 2005, pp. 588–593.
[63] S. Noge, E. Kamiyama, Y. Ueoka, T. Uno, Ultrasonics Symposium, 1997, in: Proceedings., 1997 IEEE, 1042, 1997, pp. 1043–1046.
[64] S. Noge, M. Kurita, T. Uno, Ultrasonics Symposium, 1999, in: Proceedings. 1999 IEEE, 631, 1999, pp. 633–636.
[65] S. Noge, T. Uno, Frequency and Time Forum, 1999 and the IEEE International Frequency Control Symposium, 1999, in: Proceedings of the 1999 Joint Meeting of the European, 471, 1999, pp. 477–480.
[66] P. Boeker, G. Horner, S. Rösler, Sens. Actuators B 70 (2000) 37–42.
[67] A. Palaniappan, X.D. Su, F.E.H. Tay, IEEE Sens. J. 6 (2006) 1676–1682.
[68] S. Pantalei, E. Zampetti, A. Macagnano, A. Bearzotti, I. Venditti, M.V. Russo, Sensors 7 (2007) 2920–2928.
[69] E. Zampetti, S. Pantalei, A. Macagnano, E. Proietti, C. Di Natale, A. D'Amico, Sens. Actuators B 131 (2008) 159–166.
[70] K. Jaruwongrungsee, T. Maturos, P. Sritongkum, M. Sangworasil, A. Wisitsoraat, A. Tuantranont, Int. J. Appl. Biomed. Eng. 2 (2009) 50–54.
[71] X.X. Jin, Y. Huang, A. Mason, X.Q. Zeng, Anal. Chem. 81 (2009) 595–603.
[72] K. Seidler, M. Polreichova, P.A. Lieberzeit, F.L. Dickert, Sensors 9 (2009) 8146–8157.
[73] T. Abe, IEEE Sens. J. 11 (2011) 86–90.
[74] N. Iqbal, G. Mustafa, A. Rehman, A. Biedermann, B. Najafi, P.A. Lieberzeit, F.L. Dickert, Sensors 10 (2010) 6361–6376.
[75] T. Abe, M. Esashi, Sens. Actuators A 82 (2000) 139–143.
[76] A. Goyal, P. Joshi, S. Tadigadapa, A. Gupta, P. Eklund, Proceedings of IEEE Sensors (2005) 841–844.
[77] P. Kao, A. Goyal, D. Allara, S. Tadigadapa, TRANSDUCERS and EUROSENSORS '07-4th International Conference on Solid-State Sensors, Actuators and Microsystems (2007) 2311–2314.
[78] S. Winters, G. Bernhardt, D.J. Frankel, J. Vetelino, Proceedings of the IEEE Ultrasonics Symposium (2008) 272–275.

[79] P. Kao, S. Doerner, T. Schneider, D. Allara, P. Hauptmann, S. Tadigadapa, J. Microelectromech. Syst. 18 (2009) 522–530.
[80] V.N. Hung, T. Abe, P.N. Minh, M. Esashi, Sens. Actuators A 108 (2003) 91–96.
[81] T. Abe, H. Kato, J. Micromech. Microeng. 19 (2009) 094019.
[82] M. Wark, S. Winters, C. York, W. Pinkham, G. Bernhardt, J.F. Vetelino, Ultrasonics Symposium, 2006, IEEE (2006) 880–883.
[83] I. Mannelli, M. Minunni, S. Tombelli, M. Mascini, Biosens. Bioelectron. 18 (2003) 129–140.
[84] F. Höök, M. Rodahl, B. Kasemo, P. Brzezinski, Proc. Natl. Acad. Sci. U. S. A. 95 (1998) 12271–12276.
[85] A.M. Etorki, A. Robert Hillman, K.S. Ryder, A. Glidle, Electroanal. J. Chem. 599 (2007) 275–287.
[86] S. Mildner-Szkudlarz, H.H. Jeleń, Food Chem. 110 (2008) 751–761.
[87] A.M. Martinez, A.C. Kak, IEEE T. Pattern. Anal. 23 (2001) 228–233.
[88] A. Pavlou, A.P.F. Turner, N. Magan, Lett. Appl. Microbiol. 35 (2002) 366–369.
[89] P. Boilot, E.L. Hines, M.A. Gongora, R.S. Folland, Sens. Actuators B 88 (2003) 80–88.
[90] A. Branca, P. Simonian, M. Ferrante, E. Novas, R.M. Negri, Sens. Actuators B 92 (2003) 222–227.
[91] R. Dutta, D. Morgan, N. Baker, J.W. Gardner, E.L. Hines, Sens. Actuators B 109 (2005) 355–362.
[92] M. Peris, L. Escuder-Gilabert, Anal. Chim. Acta 638 (2009) 1–15.
[93] L.F. Chen, H.Y.M. Liao, M.T. Ko, J.C. Lin, G.J. Yu, Pattern Recog. 33 (2000) 1713–1726.
[94] T. Hastie, R. Tibshirani, IEEE T. Pattern. Anal. 18 (1996) 607–616.
[95] C. Li, P. Heinemann, R. Sherry, Sens. Actuators B 125 (2007) 301–310.
[96] K. Jaruwongrungsee, T. Maturos, P. Sritongkum, A. Wisitsora-At, C. Pintavirooj, M. Sangworasil, A. Tuantranont, ECTI-CON 2010 – The 2010 ECTI International Conference on Electrical Engineering/Electronics, Computer, Telecommunications and Information Technology (2010) 548–551.
[97] M. Consales, S. Campopiano, A. Cusano, M. Penza, P. Aversa, L. Capodieci, M. Giordano, Proceedings of SPIE – The International Society for Optical Engineering (2005) 46–49.
[98] M. Penza, G. Cassano, P. Aversa, F. Antolini, A. Cusano, M. Consales, M. Giordano, L. Nicolais, Sens. Actuators B 111–112 (2005) 171–180.
[99] L. Valentini, I. Armentano, J.M. Kenny, C. Cantalini, L. Lozzi, S. Santucci, Appl. Phys. Lett. 82 (2003) 961–963.
[100] M. Trojanowicz, TrAC Trends Anal. Chem. 25 (2006) 480–489.
[101] N. Du, H. Zhang, B. Chen, M. Xiangyang, Z. Liu, J. Wu, D. Yang, Adv. Mater. 19 (2007) 1641–1645.
[102] T. Zhang, S. Mubeen, N.V. Myung, M.A. Deshusses, Nanotechnology 19 (2008) 332001.
[103] C. Steinem, A. Janshoff, F.L. Dickert, P.A. Lieberzeit, Piezoelectric Sensors (Springer Series on Chemical Sensors and Biosensors), Springer, Berlin, Heidelberg, 2007, 173–210.
[104] P.A. Lieberzeit, A. Rehman, B. Najafi, F.L. Dickert, Anal. Bioanal. Chem. 391 (2008) 2897–2903.
[105] C.K. O'Sullivan, R. Vaughan, G.G. Guilbault, Anal. Lett. 32 (1999) 2353–2377.
[106] Y.S. Fung, Y.Y. Wong, Anal. Chem. 73 (2001) 5302–5309.
[107] R.D. Vaughan, C.K. O'Sullivan, G.G. Guilbault, Enzyme Microb. Technol. 29 (2001) 635–638.
[108] S.M. Reddy, J.P. Jones, T.J. Lewis, P.M. Vadgama, Anal. Chim. Acta 363 (1998) 203–213.
[109] F. Patolsky, M. Zayats, E. Katz, I. Willner, Anal. Chem. 71 (1999) 3171–3180.
[110] J. Wang, Anal. Chem. 69 (1997) 5200–5202.
[111] F. Patolsky, A. Lichtenstein, I. Willner, J. Am. Chem. Soc. 122 (2000) 418–419.
[112] J. Wegener, A. Janshoff, H.J. Galla, Euro. Biophys. J. 28 (1998) 26–37.
[113] K.A. Marx, T. Zhou, A. Montrone, H. Schulze, S.J. Braunhut, Biosens. Bioelectron. 16 (2001) 773–782.
[114] B. Zhang, Q. Mao, X. Zhang, T. Jiang, M. Chen, F. Yu, W. Fu, Biosens. Bioelectron. 19 (2004) 711–720.
[115] Y. Luo, M. Chen, Q. Wen, M. Zhao, B. Zhang, X. Li, F. Wang, Q. Huang, C. Yao, T. Jiang, G. Cai, W. Fu, Clin. Chem. 52 (2006) 2273–2280.
[116] J.B. Schlenoff, M. Li, H. Ly, J. Am. Chem. Soc. 117 (1995) 12528–12536.
[117] M.H. Schoenfisch, J.E. Pemberton, J. Am. Chem. Soc. 120 (1998) 4502–5413.
[118] M.D. Malinsky, K.L. Kelly, G.C. Schatz, R.P. Van Duyne, J. Am. Chem. Soc. 123 (2001) 1471–1482.
[119] W. Wang, T. Lee, M.A. Reed, Phys. Rev. B: Condens. Matter Mater. Phys. 68 (2003) 354161–354167.
[120] H. Ogi, H. Nagai, Y. Fukunishi, T. Yanagida, M. Hirao, M. Nishiyama, Anal. Chem. 82 (2010) 3957–3962.
[121] T. Kallio, S. Alajoki, V. Pore, M. Ritala, J. Laine, M. Leskelä, P. Stenius, Colloids Surf. A 291 (2006) 162–176.
[122] H. Hidaka, H. Honjo, S. Horikoshi, N. Serpone, Sens. Actuators B 123 (2007) 822–828.
[123] A. Fujishima, T.N. Rao, D.A. Tryk, J. Photochem. Photobiol. C 1 (2000) 1–21.
[124] L. Chen, Y. Guan, B. Yang, D. Shen, Prog. Chem. 14 (2002) 68–76.
[125] D. Grieshaber, R. MacKenzie, J. Vörös, E. Reimhult, Sensors 8 (2008) 1400–1458.

Talanta 84 (2011) 1384–1389

Contents lists available at ScienceDirect

Talanta

journal homepage: www.elsevier.com/locate/talanta

Electrochemical detection on electrowetting-on-dielectric digital microfluidic chip

Chanpen Karuwan[a], Kreeta Sukthang[b], Anurat Wisitsoraat[a], Ditsayut Phokharatkul[a], Viyapol Patthanasettakul[a], Wishsanuruk Wechsatol[b], Adisorn Tuantranont[a,*]

[a] Nanoelectronics and MEMS Laboratory, National Electronics and Computer Technology Center, Pathumthani 12120, Thailand
[b] Department of Mechanical Engineering, King Mongkut's University of Technology, Thonburi 126 Prachauthit Road, Bangmod Thung Kharu District, Bangkok 10140, Thailand

ARTICLE INFO

Article history:
Available online 28 April 2011

Keywords:
Electrowetting-on-dielectric
Digital microfluidic
Electrochemical detection

ABSTRACT

In this work, the use of three-electrode electrochemical sensing system with an electrowetting-on-dielectric (EWOD) digital microfluidic device is reported for quantitative analysis of iodide. T-junction EWOD mixer device was designed using arrays of 50-μm spaced square electrodes for mixing buffer reagent and analyte droplets. For fabrication of EWOD chips, 5-μm thick silver EWOD electrodes were formed on a glass substrate by means of sputtering and lift-off process. PDMS and Teflon thin films were then coated on the electrodes by spin coating to yield hydrophobic surface. An external three-electrode system consisting of Au working, Ag reference and Pt auxiliary wires were installed over EWOD electrodes at the end of T-junction mixer. In experiment, a few-microliter droplets of Tris buffer and iodide solutions were moved toward the mixing junction and transported toward electrochemical electrodes by EWOD process. A short processing time within seconds was achieved at EWOD applied voltage of 300 V. The analyte droplets mixed with different concentrations were successfully analyzed by cyclic voltametry. Therefore, the combination of EWOD digital microfluidic and electrochemical sensing system has successfully been demonstrated for rapid chemical analysis with minimal reagent consumption.

1. Introduction

In recent years, there has been a great interest in miniaturized analysis systems for chemical and biological applications [1]. These systems and devices, also well known as lab-on-a-chip (LOC), offer several advantages including low sample/reagent consumption, fast analysis, high throughput and automation capability. Conventional microfluidic platforms are based on continuous flow scheme operated by fluid pressure [2] or electrokinetic actuation [3]. Recently, a new category of microfluidics, called droplet-based microfluidics, has been developed. In contrary to conventional continuous flow scheme, droplets of samples/reagent are formed instead of continuous stream, which results in lower sample/reagent consumption. There are two main types, namely continuous and discrete droplet based microfluidics. In the continuous type, droplets are generated and transported along microfluidic channels by flowing sample/reagent into an immiscible carrier fluid that separates and encapsulates continuous solution stream into microdroplets. The main benefit of this method is very high throughput. In the discrete approach, samples/reagent are formed, manipulated and analyzed as isolated microdroplets with no need of carrier and microchannel. This method has several advantages over continuous-type systems, including extremely low sample/reagent consumption, parallel processing ability, reconfigurability, architectural scalability and ease of fabrication [4]. Thus, droplet-based microfluidic systems have increasingly gained interest in various applications. Due to the architectural similarities with digital microelectronic systems, it is often referred as "digital microfluidics".

A variety of droplet manipulation technologies have been demonstrated including surface acoustic wave [5–8], thermocapillary forces [9,10], electrowetting-on-dielectric (EWOD) [11–15], dielectrophoresis (DEP) [16–21] and magnetic forces [22,23]. Among them, EWOD is one of the most promising techniques because of fast response time, easy implementation, low power consumption, no joule heating effect and large force at the millimeter to micrometer scales. The principle of electrowetting is the modulation of interfacial tension between a conducting liquid phase and an insulated solid electrode by the application of a high electric potential between the two. EWOD has been employed for a variety of droplet manipulations such as transporting, merging, mixing and splitting [4,24–26]. However, there has been relatively few reports on coupling of EWOD devices with detection components. Among a variety of detection methods, electrochemical technique is highly promising for microsystem applications because of its high performance detection, simplicity and scala-

* Corresponding author. Tel.: +66 2 564 6900; fax: +66 2 564 6756.
E-mail address: adisorn.tuantranont@nectec.or.th (A. Tuantranont).

0039-9140/$ – see front matter © 2011 Elsevier B.V. All rights reserved.
doi:10.1016/j.talanta.2011.03.073

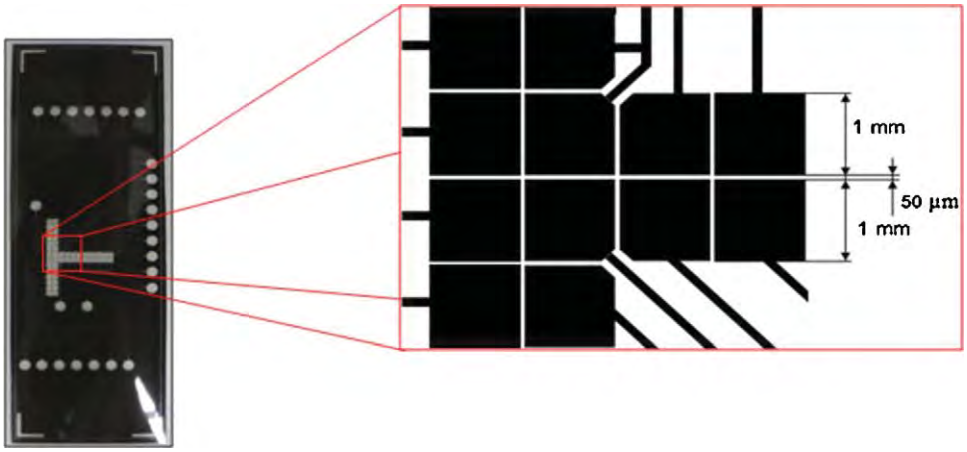

Fig. 1. The layout of electrodes for T-junction EWOD mixer device.

bility. Nevertheless, there has been very few reports on coupling of electrochemical detection scheme with EWOD microfluidic device [27,28].

In this work, the coupling of three-electrode electrochemical sensing system with EWOD digital microfluidic devices is developed for quantitative analysis of an analyte. T-junction EWOD mixer device is combined with external three-electrode system for detection of iodide microdroplets using cyclic voltametry. The characteristics of EWOD device and electrochemical detection of iodide microdroplets are studied.

2. Experimental

2.1. EWOD chip design and fabrication

T-junction EWOD mixer device is designed on a glass substrate for buffer reagent and analyte droplets mixing. The layout of electrodes for T-junction EWOD mixer device is shown in Fig. 1. EWOD electrodes are designed as closely spaced electrode arrays. To obtain effective EWOD actuation, the ratio of the gap between square electrodes (g) and the width of square electrode (w) should be minimal because the contact angle of the wetting droplet decreases with g/w ratio and it is easier for the droplet to move when the contact angle reduces [29]. However, g/w ratio is set to be 5% in order to avoid dielectric breakdown of the underlying glass substrate. Due to photolithographic constraints, the gap between square electrodes and the width of square electrode are designed to be 50 μm and 1 mm, respectively. Silver is selected as electrode material due to its high electrical conductivity.

The EWOD silver electrode was fabricated on glass substrate by lift-off process. The surface of glass substrate was cleaned with acetone and methanol. The AZ-P4620 photoresist was then deposited by spin coating at 1250 rpm for 30 s and then soft-baked at 90 °C for 3 min. Next, the photoresist was exposed to UV light under the designed photomask using MJB4 mask aligner (SUSS Microtec, Germany). It was then developed and cleaned with deionized water. The glass substrate with photoresist pattern is shown in Fig. 2(a). The photoresist was hard-baked at 120 °C for 3 min to make it hard enough for subsequent sputtering deposition. Next,

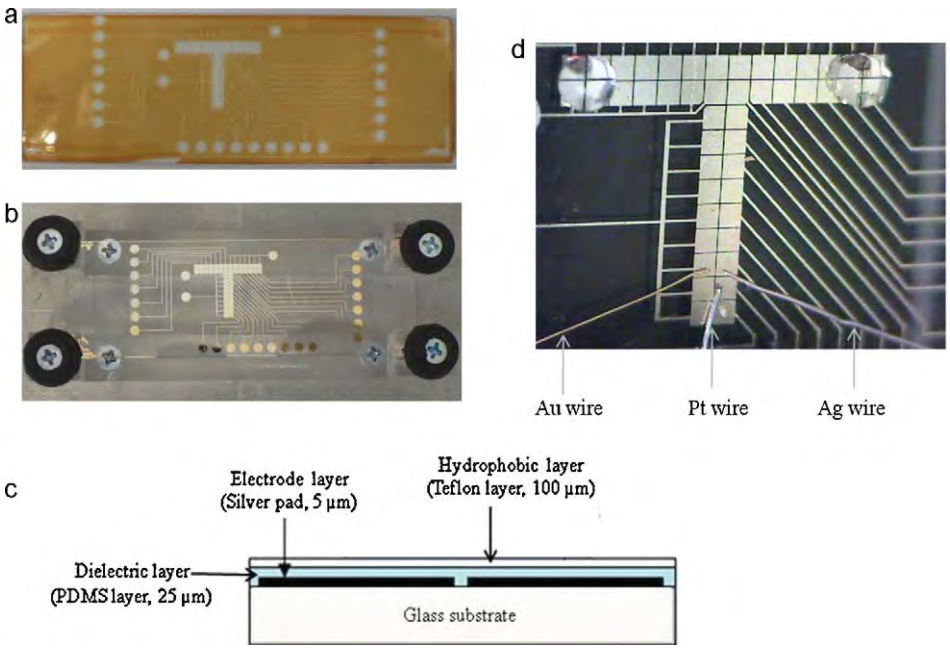

Fig. 2. (a) Photograph of glass substrate with photoresist pattern, (b) photograph of glass chip with EWOD silver electrodes, (c) cross-sectional structure of EWOD chip and (d) photograph of EWOD chip with three electrode system containing gold (Au) working electrode, platinum (Pt) auxiliary electrode and silver (Ag) reference electrode at the end of T-junction.

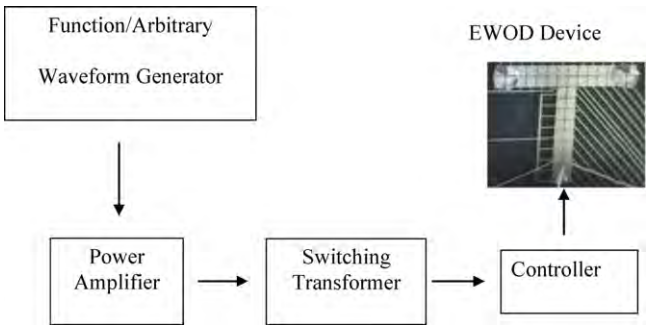

Fig. 3. Schematic diagram of the control system for EWOD device.

0.1-μm thick chromium and 5-μm thick silver films were successively sputtered by DC sputtering process at an argon pressure of 10^{-2} mbar. Next, the metal film on photoresist was lifted off by ultrasonication in acetone for 15 min.

Polydimethylsiloxane (PDMS) dielectric layer (Fig. 2(c)) was then coated on the EWOD electrode by spin coating. PDMS was prepared by mixing of silicon elastomer base and silicon elastomer curing agent with a volumetric ratio of 10:1. The PDMS was spin-coated at 4000 rpm for 30 s on top of the glass surface to form a 5 μm thick dielectric layer. The glass chip was baked at 95 °C for 60 min on a hot plate to cure PDMS. Finally, Teflon AF hydrophobic layer was spin-coated at 1000 rpm for 30 s to generate a 100 nm thick hydrophobic layer. Teflon AF solution grade 400S1-100-1 was used because of its superior hydrophobic and dielectric properties compared to normal Teflon [30]. The glass chip was baked again at 95 °C for 60 min to cure Teflon AF. The purpose of hydrophobic layer is to provide suitable contact angle and mobility for a droplet.

2.2. Electrochemical system

An external three-electrode electrochemical sensing system consisting of Au working, Ag reference and Pt auxillary wires was installed over EWOD electrodes at the end of T-junction mixer as shown in Fig. 2d. A potentiostat, μ-autolab Type III (Metrohm, Switzerland) was used for all the cyclic voltammetric (CV) studies.

2.3. Chemicals

All of chemicals used in this work were analytical grade. Standard solutions of iodide were purchased from Sigma (USA). Various buffers including acetate (pH 5) and phosphate (pH 6–8) were purchased from Merck (Germany). Tris buffer solution (pH 9) was prepared from tris (hexahydroxy) aminomethane and 1.0 M hydrochloric acid (HCl) (Lab Scan, Ireland). The stock solution (0.01 mol l^{-1}) of iodide was prepared by dissolving required amount of iodide in deionized–distilled water. Glass substrates, Photoresist (AZ®P4620), Telfon AF and PDMS were purchased from Superior (Germany), AZ electronic materials (USA), Dupont (USA) and Dow Chemical (USA), respectively.

2.4. Experimental procedure

EWOD device was driven by a control system as shown in Fig. 3. A small signal from function/arbitrary waveform generator was amplified by a power amplifier, which drove a switching transformer. The switching transformer was used to supply a high voltage of 300 V. The high voltage was applied via a high-speed controller, which provided proper switching to EWOD electrodes according to command set by users. A droplet could be forced to move forward and to turn left or right by changing the direction and position of applied voltage along the line of electrodes. In addition, the droplet movement could be accelerated or decelerated by changing the controlled time of applied voltage on each electrode. In this experiment, the signal frequency was set at 400 Hz, which was selected for suitable mobility of droplets.

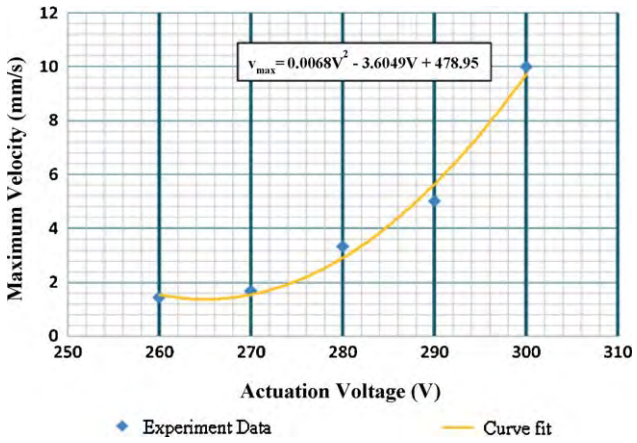

Fig. 4. Maximum velocity of droplet vs. actuation voltage of EWOD device.

For iodide analysis, a droplet of KI solution and a droplet of Tris buffer solution were dropped from auto pipette tips on two ends of T arms as shown in Fig. 3. Both droplets were then moved to the mixing junction by EWOD control voltages. After droplets were mixed, the combined droplet was transported to the three-electrode system at the end of T junction and CV measurement was performed using potential window between 0 and 1.2 V. The process was repeated with different droplet sizes to vary iodide concentration of the final droplet. The concentration was determined from the product of initial iodide concentration and the ratio of analyte's droplet volume and the final volume of the mixed droplet.

3. Results and discussions

3.1. Effect of applied voltage on the velocity of droplet

To determine suitable actuation voltage for the EWOD device, maximum droplet velocity was measured as a function of applied voltage. To find maximum droplet velocity, the controlled time of applied voltage on each electrode was increased from zero until the droplet moved from one electrode to adjacent electrode. The maximum velocity was then estimated from the distance that droplet moved (equal to the gap plus the width of electrode) and the minimum time required to move the droplet at each applied voltage. The maximum velocity of droplet as a function of actuation voltage of EWOD device is shown in Fig. 4. It can be seen that the maximum velocity increases rapidly when the applied voltage is more than 270 V. An empirical relationship of the maximum velocity and applied voltage is found to be quadratic order by regression curve fitting and is given by:

$$v_{max} = 0.0068V^2 - 3.6049V + 478.95$$

where v_{max} is the maximum velocity of water droplet (mm/s) and V is the actuation potential (V). The maximum velocity is a second order function of EWOD potential because EWOD force acting upon the droplet is proportional to the square of applied voltage [13,14] and maximum velocity varies linearly with force at a given time.

3.2. EWOD processing

Droplets of iodide and Tris buffer solutions were successfully manipulated, mixed and transported for electrochemical detection

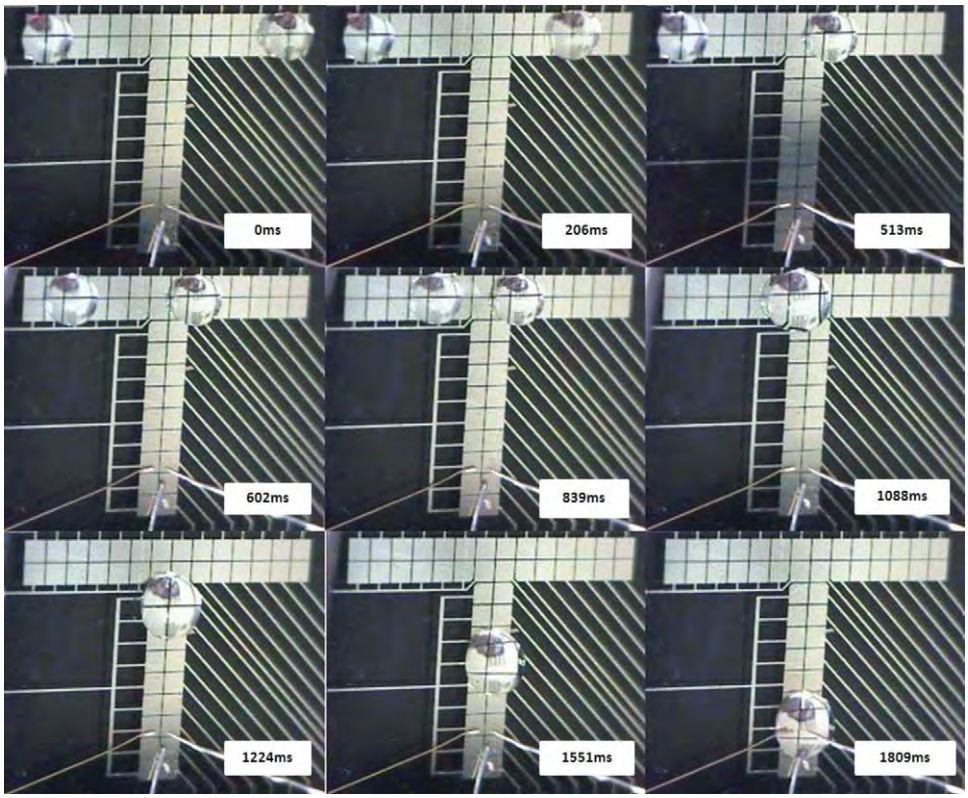

Fig. 5. Snapshots of sample and reagent droplets at various steps on EWOD device.

by EWOD process. Fig. 5 shows the snapshots of sample and reagent droplets at various steps on EWOD device. The concentration of the iodide droplet is 1 mM and the applied voltage is 300 V. It can be seen that the transport time before merging and detection are ~0.8 s and ~1.8 s, respectively. The processing time within seconds is considered short and high throughput can be achieved by EWOD. Nevertheless, it can be inferred from Fig. 4 that processing time may be further reduced to an order of milliseconds, which will be comparable to continuous flow system, by increasing applied voltage that will result in quadratic increase of maximum velocity.

3.3. Electrochemical detection of iodide droplets

3.3.1. pH dependence study

The effect of pH on response to 1 mM iodide droplet was evaluated in order to select an optimum pH value. Fig. 6 shows the cyclic voltammograms of 1 mM iodide droplets in buffers with different pHs. The Au electrodes exhibit well-defined CV of iodide with two oxidation peaks for all pHs except pH 8 that exhibit only one broad oxidation peak. pH 6 is selected for further studies on Au electrode due the observed sharp peak at 0.75 V.

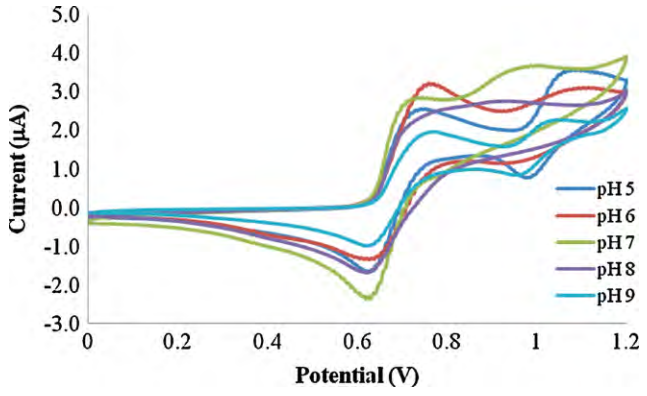

Fig. 6. The cyclic voltammograms that were obtained from EWOD chip for 1 mM iodide in various buffers (pH 5–9). The scan rate was fixed at 0.1 V/s.

3.3.2. Scan rate dependence study

Cyclic voltammograms of 1 mM iodide droplets of Au electrode were investigated at different scan rates and the results are displayed in Fig. 7(a). Fig. 7(b) shows the relationship between the second oxidation peak current and the square root of the scan rate. It is evident that peak current at the second oxidation peak varies linearly with the square root of scan rate. The slope of regression line is 6.47 μA $(s/V)^{1/2}$ and correlation coefficient (r^2) is 0.998. This confirms that the current is limited by seminfinite linear diffusion of iodide on the Au electrode [31].

3.3.3. Analytical features

The analytical performances of the EWOD electrochemical system for iodide droplet detection were characterized by CV at different concentrations ranging from 10 to 100 μM. Linear concentration dependence or dynamic range was observed between 10 and 100 μM. The regression equation was given by $y = 0.0007x + 0.0058$ ($r^2 = 0.9917$), where y and x were the height of peak current (μA) and iodide concentration (μM), respectively. The slope of the equation was corresponding to a linear sensitivity of 0.0007 μA/μM. The detection limit (3S/N) was 2.76 μM. The noise value (N) was measured by taken peak–peak amplitude of sinusoidal noise in the base line region of CV curve. The stability was checked by recording successive CVs. The electrode remained stable after 20 successive cycles with relative standard deviation (RSD) of 3.3% ($n = 20$). The total analysis time including droplet mixing and CV measurement was approximately 12 s. Therefore, the analytical

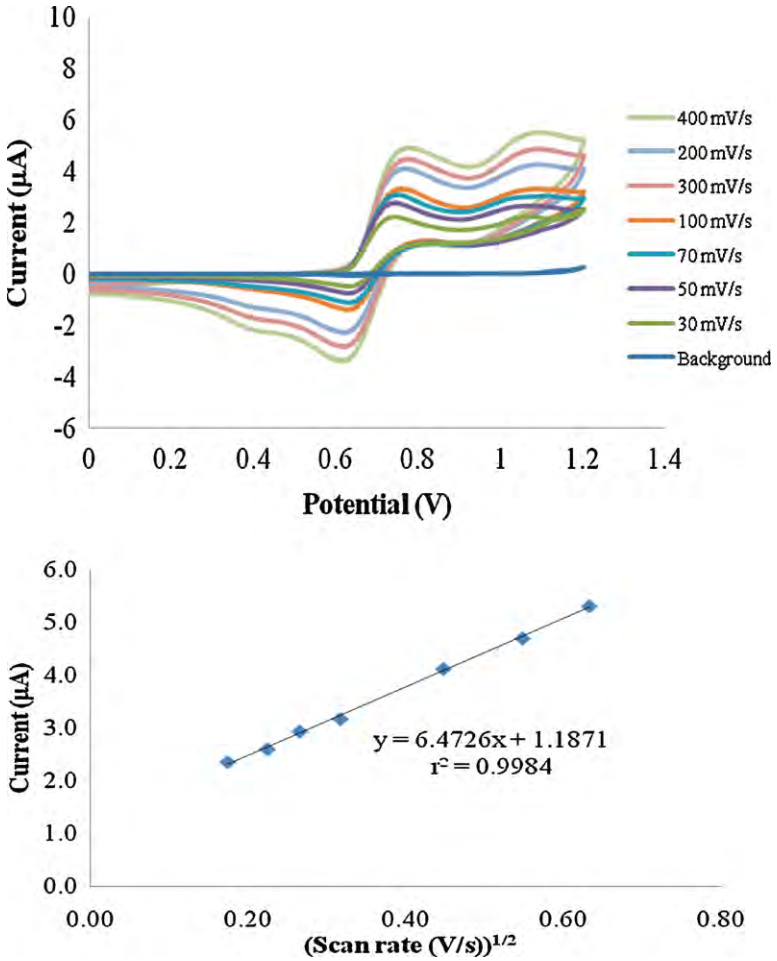

Fig. 7. (a) Cyclic voltammograms, obtained at various potential scan rates for 1 mM iodide in 1 mM phosphate buffer (pH 6) of Au electrode. (b) The relationship between the second oxidation peak current and the square root of the scan rate.

performances are attractive for high throughput real world analysis of iodide in pharmaceutical and medical applications.

4. Conclusions

In conclusion, the coupling of three-electrode electrochemical sensing system with a droplet-based EWOD microfluidic device is demonstrated for quantitative analysis of iodide. An external three-electrode electrochemical sensing system consisting of Au working, Ag reference and Pt auxiliary wires was suspended at the end of T-junction EWOD mixing device. Microdroplet of Tris buffer and potassium iodide solution were mixed and successfully detected by cyclic voltametry with short processing time within seconds. The combination of EWOD digital microfluidic and electrochemical sensing system is illustrated as a promising method for rapid chemical analysis with minimal reagent consumption.

Acknowledgements

Adisorn Tuantranont would like to express his gratitude for Researcher Career Development Grant from Thailand Research Fund (TRF). Wishsanuruk Wechsatol would also like to acknowledge the financial support from Industry/University Cooperative/Research Center in HDD Advanced Manufacturing and National Electronics and Computer Technology Center, National Science and Technology Development Agency.

References

[1] E. Verpoorte, Electrophoresis 23 (2002) 677–712.
[2] C. Karuwan, A. Wisitsoraat, T. Maturos, D. Phokharatkul, A. Sappat, K. Jaruwongrungsee, T. Lomas, A. Tuantranont, Talanta 79 (2009) 995–1000.
[3] J. Wang, Electrophoresis 23 (2002) 713–718.
[4] M.G. Pollack, A.D. Shendorov, R.B. Fair, Lab Chip 2 (2002) 96–101.
[5] D. Beyssen, L.L. Brizoual, O. Elmazria, P. Alnot, Sens. Actuators B 118 (2006) 380–385.
[6] Z. Guttenberg, H. Müller, H. Habermüller, A. Geisbauer, J. Pipper, J. Felbel, M. Kielpinski, J. Scriba, A. Wixforth, Lab Chip 5 (2005) 308–317.
[7] J. Shi, D. Ahmed, X. Mao, S.-C.S. Lin, A. Lawit, T.J. Huang, Lab Chip 9 (2009) 2890–2895.
[8] T. Franke, A.R. Abate, D.A. Weitz, A. Wixforth, Lab Chip 9 (2009) 2625–2627.
[9] J.Z. Chen, S.M. Troian, A.A. Darhuber, S. Wagner, J. Appl. Phys. 97 (2005) 014906.
[10] A.T. Ohta, A. Jamshidi, J.K. Valley, H.-Y. Hsu, M.C. Wu, Appl. Phys. Lett. 91 (2007) 07413.
[11] D. Brassardab, L. Malicac, F. Normandina, M. Tabrizianc, T. Veres, Lab Chip 8 (2008) 1342–1349.
[12] S.K. Cho, H. Moon, C.-J. Kim, J. MEMS 12 (2003) 70–80.
[13] M. Vallet, B. Berge, L. Vovelle, Polymer 37 (1996) 2465–2470.
[14] M. Abdelgawad, S.L.S. Freire, H. Yang, A.R. Wheeler, Lab Chip 8 (2008) 672–677.
[15] J. Gong, C.-J. Kim, Lab Chip 8 (2008) 898–906.
[16] S.-Y. Park, C. Pan, T.-H. Wu, C. Kloss, S. Kalim, C.E. Callahan, M. Teitell, E.P.Y. Chiou, Appl. Phys. Lett. 92 (2008) 151101.
[17] J.A. Schwartz, J.V. Vykoukal, P.R.C. Gascoyne, Lab Chip 4 (2004) 11–17.
[18] S.-Y. Park, S. Kalim, C. Callahan, M.A. Teitell, E.P.Y. Chiou, Lab Chip 9 (2009) 3228–3235.
[19] K. Ahn, C. Kerbage, T.P. Hunt, R.M. Westervelt, D.R. Link, D.A. Weitz, Appl. Phys. Lett. 88 (2006) 024104.
[20] O.D. Velev, B.G. Prevo, K.H. Bhatt, Nature 426 (2003) 515–516.
[21] J.-C. Baret, O.J. Miller, V. Taly, M. Ryckelynck, A. El-Harrak, L. Frenz, C. Rick, M.L. Samuels, J.B. Hutchison, J.J. Agresti, D.R. Link, D.A. Weitz, A.D. Griffiths, Lab Chip 9 (2009) 1850–1858.
[22] Z.-G. Guo, F. Zhou, J.-C. Hao, Y.-M. Liang, W.T.S. Huck, W.-M. Liu, Appl. Phys. Lett. 89 (2006) 081911.

[23] M. Okochi, H. Tsuchiya, F. Kumazawa, M. Shikida, H. Honda, J. Biosci. Bioeng. 109 (2010) 193–197.
[24] S.-K. Cho, H. Moon, C.-J. Kim, Microelectromech. Syst. 12 (2003) 32–52.
[25] P.Y. Paik, V.K. Pamula, M.G. Pollack, R.B. Fair, Lab Chip (2003) 28–33.
[26] P.Y. Paik, V.K. Pamula, R.B. Fair, Lab Chip 3 (2003) 253–259.
[27] P. Dubois, G. Marchand, Y. Fouillet, J. Berthier, T. Douki, F. Hassine, S. Gmouh, M. Vaultier, Anal. Chem. 78 (2006) 4909–4917.
[28] J.L. Poulos, W.C. Nelson, T.J. Jeon, C.C. Kim, J.J. Schmidt, Appl. Phys. Lett. 95 (2009), 13706-13703.
[29] U.C. Yi, C.J. Kim, J. Micromech. Microeng. 16 (2006) 2053–2059.
[30] P. Resnick, W. Buck, in: Hougham et al., Fluoropolymers 2: Properties, Plenum Press, New York, 1999, pp. 25–33.
[31] S. Gottesfeld1, S.W. Feldberg, J. Electroanal. Chem. Interface Electrochem. 194 (1) (1985) 1–10.

Talanta 84 (2011) 1390–1395

Contents lists available at ScienceDirect

Talanta

journal homepage: www.elsevier.com/locate/talanta

AAO–CNTs electrode on microfluidic flow injection system for rapid iodide sensing

Ditsayut Phokharatkul[a], Chanpen Karuwan[a,b,c], Tanom Lomas[a], Duangjai Nacapricha[b,c], Anurat Wisitsoraat[a], Adisorn Tuantranont[a,*]

[a] Nanoelectronics and MEMS Laboratory, National Electronics and Computer Technology Center, Pathumthani 12120, Thailand
[b] Flow Innovation-Research for Science and Technology (FIRST) Laboratories, Faculty of Science, Mahidol University, Rama 6 Road, Bangkok 10400, Thailand
[c] Department of Chemistry, Center of Excellence for Innovation in Chemistry, Faculty of Science, Rama 6 Road, Bangkok 10400, Thailand

ARTICLE INFO

Article history:
Available online 28 April 2011

Keywords:
Flow injection
Microfluidic device
Carbon nanotubes
Iodide detection
In-channel electrochemical detection
Lab-on-a-chip

ABSTRACT

In this work, carbon nanotubes (CNTs) nanoarrays in anodized aluminum oxide (AAO–CNTs) nanopore is integrated on a microfluidic flow injection system for in-channel electrochemical detection of iodide. The device was fabricated from PDMS (polydimethylsiloxane) microchannel bonded on glass substrates that contains three-electrode electrochemical system, including AAO–CNTs as a working electrode, silver as a reference electrode and platinum as an auxiliary electrode. Aluminum, stainless steel catalyst, silver and platinum layers were sputtered on the glass substrate through shadow masks. Aluminum layer was then anodized by two-step anodization process to form nanopore template. CNTs were then grown in AAO template by thermal chemical vapor deposition. The amperometric detection of iodide was performed in 500-μm-wide and 100-μm-deep microchannels on the microfluidic chip. The influences of flow rate, injection volume and detection potential on the current response were optimized. From experimental results, AAO–CNTs electrode on chip offers higher sensitivity and wider dynamic range than CNTs electrode with no AAO template.

1. Introduction

Microfluidics is a potential technology for biochemical processing and analysis because of low sample/reagent consumption, high sample throughput and total analysis capability [1,2]. Plastic/glass based microfluidic platforms have been extensively used for various applications due to wide functionality, low cost and disposability [3–7]. Polydimethylsiloxane (PDMS) has become a primary plastic material for miniaturized analytical system due to its high chemical and mechanical stability and a variety of PDMS based microfluidic chips [6,7] have been fabricated by standard micromolding technology [8,9].

Integration of efficient sensors or detection devices in microfluidic chips has been an important issue in the development of full functional microfluidic systems. Among a variety of detection methods, electrochemical technique is highly promising because it offers high performance detection and can directly be fabricated on plastic/glass based microfluidic chips [10]. Recently, electrochemical detection has been embedded in microfluidic systems based on end-channel [11,12] and in-channel [10,13,14] detection scheme using different electrode materials, including gold, platinum and carbon paste. Nevertheless, conventional electrochemical electrodes are not fast and highly sensitive enough for general micro total analysis applications, which involve small analyte volume and short sampling time.

Therefore, novel sensing materials should be integrated in microfluidic system to improve detection performances. Carbon nanotubes (CNTs) are promising for electrochemical sensing due to its high reaction area and excellent electron transfer rate [15]. CNTs have been widely applied as sensors in various electroanalysis applications [16–21]. Recently, microfluidic glass chips with directly grown CNTs electrode for sensitive and rapid salbutamol sensing have been reported [22]. However, naturally grown CNTs are still not yet ideal electrochemical sensors because its very high density hinders dynamics of electrochemical process. Thus, the use of CNTs for electrochemical sensing can be more effective if CNTs can be formed with micro/nano array configuration.

Anodized aluminum oxide (AAO) is a highly useful nanopore template for nanostructure formation and organization due to its low cost, ease of fabrication and high chemical stability. AAO nanopore can be used to separate CNT forest into nano array [23–26] to improve the performance of CNTs electrode by hemispherical solute diffusional effect [27]. However, there has been no report on the use of AAO–CNTs electrode in microfluidic devices.

* Corresponding author. Tel.: +66 2 564 6900; fax: +66 2 564 6771.
E-mail addresses: anurat.wisitsoraat@nectec.or.th (A. Wisitsoraat), adisorn.tuantranont@nectec.or.th (A. Tuantranont).

0039-9140/$ – see front matter © 2011 Elsevier B.V. All rights reserved.
doi:10.1016/j.talanta.2011.03.071

In this work, a new microfluidic device is developed using PDMS/glass chip with in-channel amperometric detection based on AAO–CNTs electrode. The three-electrode system was fabricated on glass substrate as an in-channel detection using thin-film sputtering and chemical vapor deposition (CVD) technique. The system was applied for determination of potassium iodide (KI). Iodide detection is of interest because it is used to determine iodide deficiency in human, which results in diseases including hypothyrodism, spontaneous abortion and cretinism. The new device would allow fast and sensitive detection of iodide with relatively low sample/reagent consumption.

2. Experimental

2.1. Chemicals and reagents

All of chemicals used in this work were analytical grade. Standard solutions of KI were purchased from Sigma (USA). Sodium phosphate monobasic monohydrate and sodium phosphate dibasic were also purchased from Sigma (USA) to prepare a phosphate buffer solution. The standard stock solution (100 mol l^{-1}) of KI was prepared by dissolving required amount of KI in the phosphate buffer solution (pH 5.8). KI solutions with different concentrations were then prepared for testing by proper dilution of the stock solution. Glass substrates, PDMS and Photoresist (SU-8 2100) were acquired from Sperior (Germany), Dow Chemical (USA), Micro Chem (USA), respectively.

2.2. Apparatus

A potentiostat, μ-autolab Type III (Metrohm, Switzerland) was used for all the cyclic voltammetric (CV) and amperometric studies. Spin coater (Laurell Technologies Corp., model WS-400A-6NPP) was used for spin coating of photoresist for mold fabrication. The MJB4 mask aligner (SUSS Microtec, Germany) was used for UV-lithography process to obtain photoresist patterns on Si-substrate. The oxygen plasma cleaner (Harrick Scientific Corp., model PDC-32G) was used for treatment of PDMS and glass surface to obtain good bonding.

2.3. Electrochemical cell for cyclic voltammetry

Cyclic voltammetry (CV) is an initial technique for characterization of electrochemical behaviors of electrodes and analytes. For CV measurement, AAO–CNTs and CNTs electrodes were fabricated on ⟨1 0 0⟩ Si substrates. The schematic structure of AAO–CNTs is illustrated in the inset of Fig. 1. First, Al (200 nm) layer was sputtered on the substrate as a contact layer and very thin layer of alumina (10 nm) was successively deposited by reactive RF sputtering. The alumina layer was used to support stainless steel catalyst (5 nm), which was subsequently sputtered on it for CNTs growth. Next, 2 μm thick Al layer was sputtered on the stainless steel catalyst. The alumina layer was deposited by reactive RF sputtering at a pressure of 3×10^{-3} mbar with 1:5 $Ar:O_2$ gas mixture while other metallic layers were deposited by pure Ar gas at the same pressure.

The top aluminum layer was then anodized in a 0.3 M oxalic acid solution at a constant applied voltage of 40 V for 5 min at room temperature. Next, the resultant aluminum oxide film was removed by a mixed solution of phosphoric acid (4 wt.%) and chromic acid (1.5 wt.%). The second anodization was then performed for 15 min under the same condition. The aluminum oxide layer was etched again by the etching solution for 30 min in order to widen the nanopore and expose the stainless steel catalyst.

CNTs were then grown in AAO template on silicon wafer by chemical vapor deposition (CVD) [19–21]. The CVD process is used because of its low cost and high quality CNTs structure. The catalyst

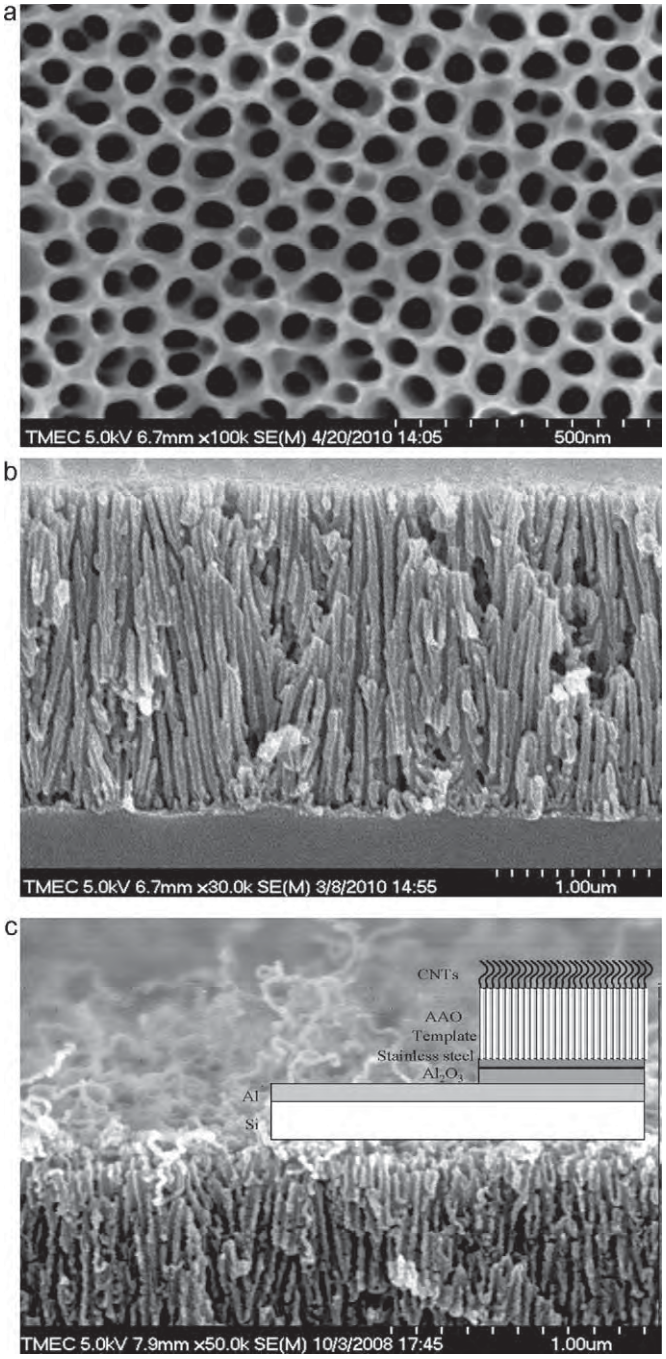

Fig. 1. SEM images of (a) top view of AAO template, (b) cross-sectional view of AAO template and (c) cross-sectional view of AAO–CNTs electrode. Inset: structure of AAO–CNTs electrode.

layer on substrates was placed on an alumina carrier in a horizontal furnace thermal CVD system. The CNTs synthesis was conducted at the atmospheric pressure and growth temperature of 700 °C. During CNTs growth, acetylene was flowed for 1.5 min and hydrogen to acetylene flow rate ratio was 4.3:1. In the course of CNTs growth, in situ water-assisted etching was employed to remove undesired amorphous carbon formation from random acetylene decomposition [21]. In water etching process, 300 ppm of water vapor was introduced by water bubbling through Ar gas for 3 min while acetylene gas was turned off. CNTs growth and water-assisted etching were repeatedly performed for five cycles.

CV experiments were performed using AAO–CNTs and CNTs electrodes in a home-made electrochemical cell. The three-

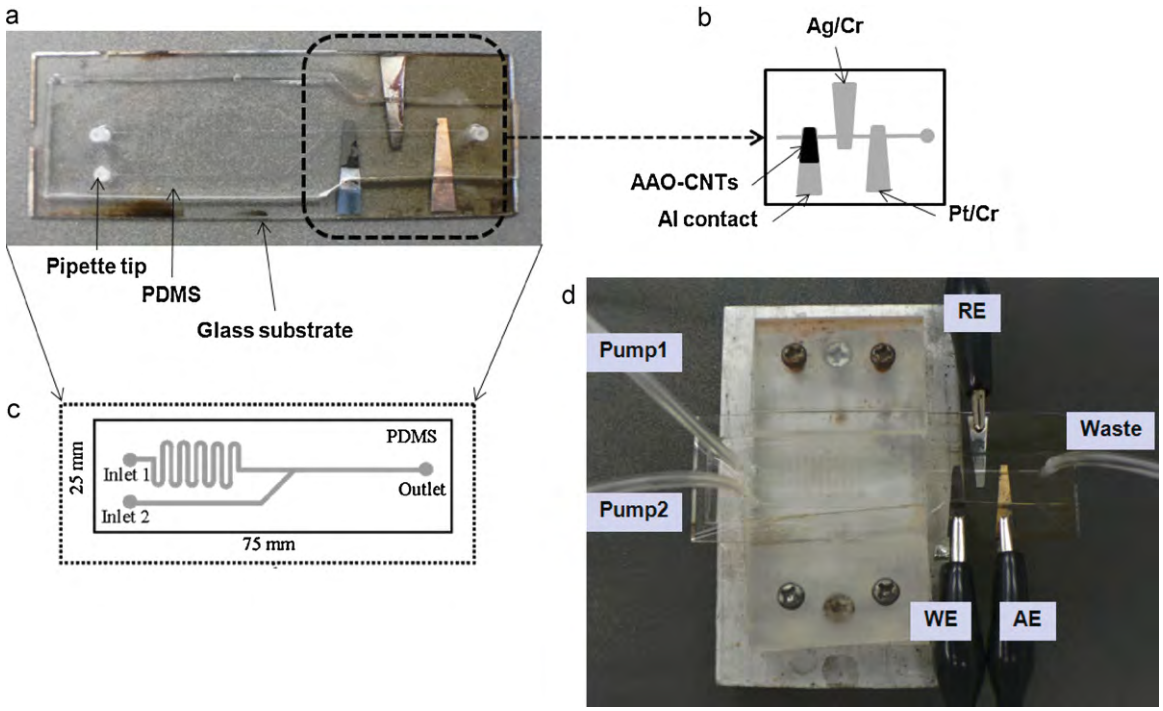

Fig. 2. Microchip and AAO–CNTs in-channel amperometric detector.

electrode system consisted of Pt wire auxiliary electrode, silver/silver chloride (Ag/AgCl) reference electrode and AAO–CNTs or CNTs working electrode. The area of working electrode was set at 0.7 cm^2 and the cell volume was 1.5 ml.

2.4. Fabrication of the miniaturized microfluidic system

The fabrication process of the miniaturized microfluidic system consisted of three main tasks. Firstly, PDMS chip containing microchannel was made by micromolding and casting process. Secondly, three-electrode system was formed on a glass substrate by sputtering and chemical vapor deposition (CVD) processes. The PDMS and glass chip were then bonded using oxygen plasma treatment. Fig. 2 shows the structure of microfluidic device with AAO–CNTs electrode.

For the fabrication of PDMS chip, microfluidic channels were fabricated based on standard photolithography. SU-8 photoresist was spun on Si substrate using spin coater and then soft baked to remove solvent in the layer. UV-lithography was performed to obtain photoresist patterns on Si substrate using MJB4 mask aligner and then post-baked in order to selectively cross-link the exposed portion of photoresist. Finally, the photoresist was developed and cleaned with deionized water and isopropyl alcohol. The microfluidic chip was designed to have two microchannel inlets and one microchannel outlet as shown in Fig. 2(c). For two microchannel inlets, one was used for buffer carrier stream and the other was for injection of analyte. The microchannel is 100 μm deep and 500 μm wide.

In the second part, three electrodes including CNTs, Pt and Ag electrodes were designed as straight stripes across microchannel as shown in Fig. 2(a) and (b). Three electrodes were located opposite to the outlet of microchannel. The auxiliary and reference electrodes were 200 μm wide and 300 nm thick platinum and silver layers each supported by 50 nm Cr adhesive layers. To obtain the AAO–CNTs working electrode, multilayer films were sputtered, top Al layer was anodized by two-step anodization process and CNTs were grown by CVD technique as previously described in Section 2.3, but in this case glass substrate was used and CNTs growth was performed at a lower temperature of 550 °C.

In the last part, the PDMS and glass chip were treated in 35-W radio-frequency oxygen plasma for 30 s. They were immediately aligned and attached after oxygen plasma treatment as shown in Fig. 2(a). Next, the inlet and outlet of microchannel were drilled and connected to micro tubing via pipette tips, which could be sealed to PDMS holes by physical attachment without the use of adhesive as shown in Fig. 2(d). The inlets were connected to syringe pumps and outlet was connected to a reservoir. Syringe pump (Pump 1) was used for propelling the running buffer into microchannel inlet 1. Microchannel inlet 2 was used for analyte injection controlled by the second syringe pump (Pump 2). Finally, the whole apparatus was mounted on an aluminum fixture and electrodes were electrically connected to potentiostat. The developed system was used for all amperometric experiments.

2.5. Microfluidic procedure

Before use, the channel was treated with deionized water for 10 min. The running buffer was PBS buffer (pH 5.8). The chronoamperograms were recorded with time while applying a detection potential at +0.6 V versus Ag/AgCl reference electrode. Sample injections were performed after stabilization of baseline buffer signal. The running buffer was delivered into the channel using a syringe pump at a controlled flow rate. The analytes were injected into the channel by propelling of syringe pump with a controlled volume.

3. Results and discussion

3.1. AAO–CNTs electrode

The device structure was characterized by scanning electron microscope (SEM). Fig. 1(a) shows the top-view SEM image of AAO template after two-step anodization. It is seen that the pore size is quite uniform and the average pore diameter is about 50 nm.

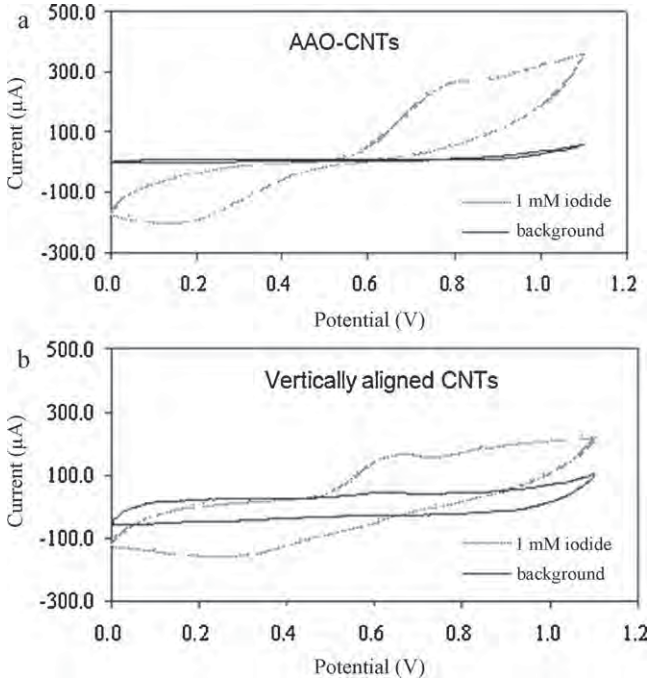

Fig. 3. Cyclic voltamograms for 1 mM iodide of (a) AAO–CNTs and (b) vertically aligned CNTs electrode in phosphate buffer solution pH 5.8.

Fig. 1(b) shows the cross-sectional view SEM image of AAO template. It is seen that the thickness of AAO layer is approximately 2 μm. Fig. 1(c) demonstrates the cross-sectional view SEM image of AAO–CNTs electrode along with its structural diagram. It can be observed that CNTs is protruded from the bottom of AAO template. The average diameter of CNTs is found to be around 30 nm by transmission microscope.

3.2. Cyclic voltammetry

In order to assess the efficacy of AAO–CNTs electrode, the electrochemical characteristics of AAO–CNTs electrode was compared to vertically aligned CNTs electrode with no AAO template. Fig. 3(a) and (b) shows cyclic voltammogram for 1 mM iodide solution of AAO–CNTs and CNTs electrodes, respectively. It is evident that AAO–CNTs electrode has much lower background current than CNTs electrode does. In addition, AAO–CNTs electrode exhibits much higher irreversible oxidation peak than vertically aligned CNTs electrode does. Thus, AAO nanopores considerably enhance the iodide response and signal to background ratio of CNTs electrode. The enhancement can be attributed to the formation of CNTs nanoarray by AAO nanopore template. The sensing area is increased and hemispherical solute diffusional effect is exploited.

Moreover, it can be noticed that there is a considerable difference between iodide peak potentials of AAO–CNTs (0.76 V in Fig. 5(a)) and CNTs (0.64 V in Fig. 5(b)) electrodes. A possible explanation for this result is that the electrical resistance of AAO–CNTs electrode is higher than that of CNTs one and it causes the observed potential shift. To validate this assumption, the resistances between electrode surface and metal contact were measured and the resistances of AAO–CNTs and CNTs electrodes were found to be ~200 Ω and ~3 Ω, respectively. The relatively high resistance of AAO–CNTs electrode can cause a potential drop of ~0.1 V when a peak current of 300 μA flows through. Thus, the assumption is highly probable. The higher resistance could be due to considerably lower density and shorter length of CNTs grown in AAO nanopores compared to CNTs grown with no AAO template.

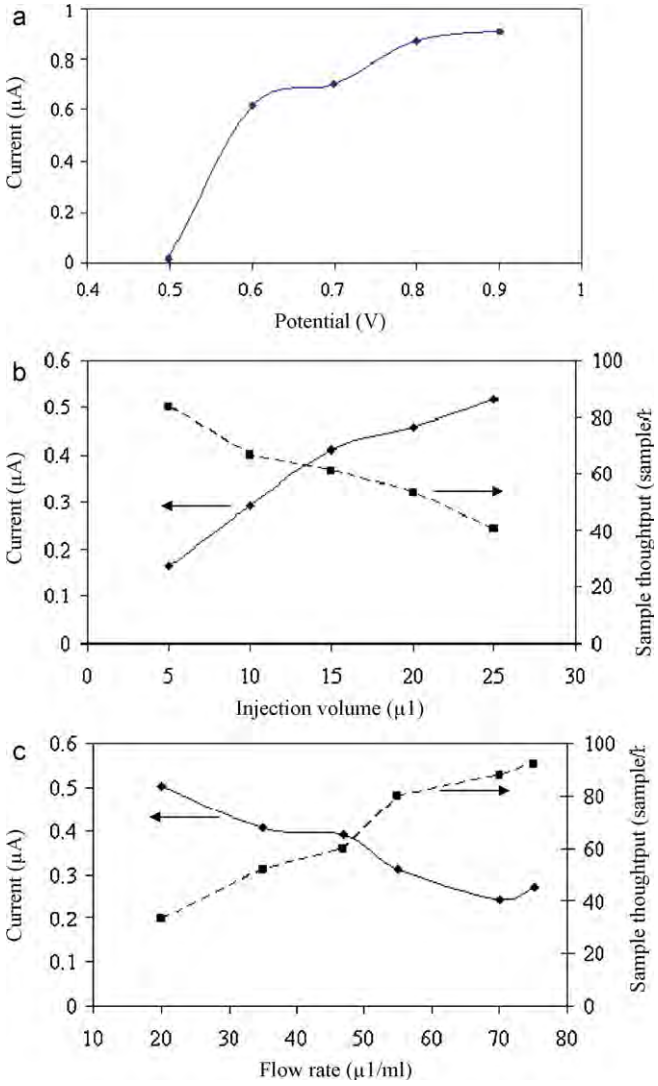

Fig. 4. Effects of (a) detection potential on current signal, (b) injection volume and (c) flow rate on current signal and sample throughput.

3.3. Flow injection optimization

The detection potential strongly affects the sensitivity of current signal of an analyte. To obtain the optimal detection potential, the hydrodynamic voltammogram was determined. Hydrodynamic voltammetry was studied from injection of 10 μl of 1 mM standard iodide solution into the micro flow system with varying detection potential from 0.5 to 0.9 V as shown in Fig. 4(a). It can be seen that the current response increases as the potential increases and seems to saturate at potential above 0.8 V. Thus, the detection potential of 0.8 V was selected for all amperometric detection in micro flow experiments.

The effect of injection volume on analytical performances of AAO–CNTs electrode was investigated over the range between 5 and 25 μl. Fig. 4(b) shows the current response and throughput versus injection volume of 1 mM standard iodide at a fixed flow rate of 50 μl/min. It is evident that throughput decreases but current signal increases with increasing injection volume. The injection volume of 15 μl was thus chosen to compromise sensitivity and throughput (60 samples/h).

In order to achieve the satisfactory sensitivity and sample throughput, the effect of flow rate was optimized using the injection of 15 μl of standard iodide solution. Fig. 4(c) shows that the

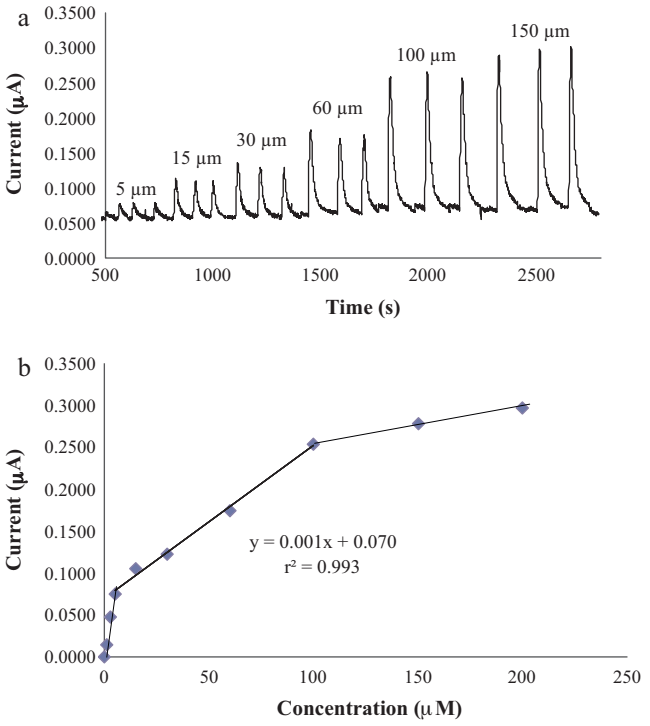

Fig. 5. (a) Effects of concentration of standard iodide on current signal and (b) calibration curve.

response decreases with increasing flow rate from 20 to 75 μl/min. Conversely, increasing flow rate increases sample throughput. To balance between response and sample throughput, the flow rate of 50 μl/min was selected.

3.4. Microfluidic system with amperometric detection

In order to test fouling or adsorption of the analyte compound on AAO–CNTs electrode, responses from replicate injections of standard iodide of 1 mM were evaluated in term of relative standard deviation (RSD). The developed system gave a fair repeatability with RSD of 8.86% (n = 12) so fouling of the AAO–CNTs electrode was considered low. However, the result was still not acceptable and it should be improved by further optimizing electrode structure as well as conditions for amperometric detection.

In order to obtain a calibration curve, the varied concentrations of standard iodide from 1 to 200 μM were injected into the system and current response amplitude was measured. Fig. 5(a) shows the effect of concentration on current signal with different concentrations ranging from 1 to 200 μM with three replicate injections. Fig. 5(b) demonstrates the calibration curve of current signal over concentration ranging from 1 to 200 μM. It can be seen that linear concentration dependence is observed in the range between 5 and 100 μM. The regression equation is given by $y = 0.001x + 0.07$ (r^2 = 0.993), where y and x are the height of peak current (μA) and iodide concentration (μM), respectively. The slope of the equation is corresponding to linear sensitivity of 0.001 μA/μM. The detection limit (3S/N) is ~0.5 μM. At low concentration (less than 5 μM), iodide peak current also varies linearly but with a higher slope value. On the other hand, the response current begins to level off at higher iodide concentrations (100–200 μM).

3.5. Real sample analysis and interference study

The possibility for the use of the developed system in real sample analysis was studied with pharmaceutical products containing iodide. Iodide contents in four pharmaceutical tablets, namely 'Centrum', 'Bioton', 'Obimin' and 'Revicon' were analyzed by the developed electrochemical system. Tablets were ground before extraction with water, centrifuged and filtrated through 0.25 μm cellulose acetate membrane. The filtrates were then suitably diluted with 50 mM tris buffer pH 5.8. The measured results were compared to the labeled values from their manufacturer and results from ion selective electrode (ISE) potentiometric analysis as shown in Table 1. ISE measurement was conducted by a commercial digital Orion ion-analyzer (model 601A). Before ISE measurement, the ion strength of solution was adjusted by adding suitable amount of 5 M $NaNO_3$ solution. The potential developed across the employed iodide-ISE (Orion, USA) and the saturated calomel electrode (Orion) was then measured in the prepared sample solution.

Table 1
Comparison of the labeled values of iodide content in pharmaceutical products and the analyzed results by ISE analysis and flow injection chronoamperometry using AAO–CNTs electrode.

Samples	Content of iodide (μg/tablet)		
	Label	AAO–CNTs electrode	Ion selective electrode
Revicon 1	200	220 ± 12	195 ± 7.2
Revicon 2	200	226 ± 9.3	197 ± 5.2
Revicon 3	200	227 ± 7.1	198 ± 4.5
Obimin 1	100	80 ± 4.7	98 ± 5.3
Obimin 2	100	86 ± 5.6	96 ± 4.6
Obimin 3	100	86 ± 3.3	97 ± 4.3

Table 2
Effects of foreign ions on the current signal obtained from adding of foreign species into 90 μM potassium iodide solution.

Foreign species	Content label in some sample (mg/l)	Results[a]
Vitamin C or L(+)ascorbic acid/$C_8H_8O_6$	90–100	Strongly interfere (studied from 40 to 320 mg/l)
Cl^-/NaCl	40	Does not interfere (studied from 40 to 160 mg/l)
Br^-/NaBr	40	Does not interfere (studied from 40 to 200 mg/l)

[a] Greater than ±5% signal variation is classified as interfering condition.

It can be seen that the results for Obimin and Revicon from our developed system are in fair agreement to those obtained from standard ISE method. The results determined by both methods are considered not greatly different at 95% confidence by paired t-test (t_{stat} = 0.85, $t_{critical}$ = 2.57). However, the differences between the results from our and standard method are quite notable (10–20%). Thus, there is considerable interference to iodide by other species in Obimin and Revicon. In addition, it was found that very strong interference occurred in other tested products including Centrum and Bioton.

Further interference study was conducted to identify species that contribute strong interference. Interferences were tested towards three electroactive species including ascorbic acid, chloride and bromide, which were major ingredients in these pharmaceutical tablets, at their nominal concentrations. Table 2 summarizes the interference results of ascorbic acid (40–320 mg/dl), chloride (40–160 mg/dl) and bromide (40–200 mg/dl) in 90 μM potassium iodide solution. It can be seen that chloride and bromide give very low interference signals while ascorbic acid produces considerable interference. Thus, ascorbic acid, which is an active ingredient of Revicon, is one of strong interference species that

should be separated to avoid analysis errors. From these results, AAO–CNTs electrode does not possess general anti-interference capability. Sample pretreatment including separation is needed to overcome the interference problem in general cases especially urine samples, which contain very complex matrices.

4. Conclusions

In conclusion, in-channel amperometric microfluidic device with AAO–CNTs electrode has successfully been developed for iodide detection. The device demonstrates the first utilization of AAO–CNTs electrode on glass based microfluidic chip for iodide detection. The electrocatalytic activity of iodide on AAO–CNTs is good when compared with vertically aligned CNTs electrode with higher response and signal to background ratio. Moreover, AAO–CNTs electrode exhibits good stability in flowing system and fair reproducibility for amperometric detection. Thus, the combination of sensitive AAO–CNTs electrode and miniaturized analysis system is a new and promising technique for chemical detection.

Acknowledgements

The authors would like to acknowledge the research funding from National Electronics and Computer Technology Center and National Science and Technology Development Agency. Adisorn Tuantranont would like to express his gratitude for Researcher Career Development Grant from Thailand Research Fund (TRF). And from the Center for Innovation in Chemistry: Postgraduate Education and Research Program in Chemistry (PERCH-CIC).

References

[1] H. Becker, L.E. Locascio, Talanta 56 (2002) 267–287.
[2] D.R. Rwyes, D. Iossifidis, P.A. Auroux, A. Manz, Anal. Chem. 74 (2002) 2623–2636.
[3] Y. Liu, D. Ganser, A. Schneider, R. Liu, P. Grdzinski, N. Kroutchinina, Anal. Chem. 73 (2001) 4196–4201.
[4] S.M. Ford, B. Kar, S. McWhorter, J. Davies, S.A. Soper, M. Klopf, G. Calderon, V.J. Saile, Microcolumn 10 (1998) 413–422.
[5] J.C. McDonald, D.C. Duffy, J.R. Anderson, D.T. Chiu, H. Wu, O.J.A. Schueller, G.M. Whitesides, Electrophoresis 21 (2000) 27–40.
[6] M.J. Schoning, M. Jacobs, A. Muck, D.-T. Knobbe, J. Wang, M. Chatrathi, S. Spillmamm, Sens. Actuators B 108 (2005) 688–694.
[7] O. Yassine, P. Morin, O. Dispagne, L. Renaud, L. Denoroy, P. Kleimann, K. Faure, J.-L. Rocca, N. Ouaini, R. Ferrigno, Anal. Chim. Acta 609 (2008) 215–222.
[8] G.S. Virdi, R.K. Chutani, P.K. Rao, S. Kumar, Sens. Actuators B 128 (2008) 422–426.
[9] Micro Chem, Nano SU-8 2000, Negative Tone Photoresis Formulations 2035–2100.
[10] K.-W. Lin, Y.-K. Huang, H.-L. Su, Y.-Z. Hsieh, Anal. Chim. Acta 619 (2008) 115–121.
[11] M. Castano-Alvarez, M.T. Fernansez-Abedul, A. Costa-Garcia, J. Chromotogr. A 1109 (2006) 291–299.
[12] D.F. Pozo-Ayuso, M. Castano-Alvarez, A. Fernansez-la-Villa, M. Garcia-Granda, M.T. Fernandez-Abedul, A. Costa-Garcia, J. Rodriguez-Garcia, J. Chromotogr. A 1180 (2008) 193–202.
[13] K.-T. Liao, C.-M. Chen, H.-J. Huang, C.-H. Lina, J. Chromotogr. A 1165 (2007) 213–218.
[14] N. Dossi, R. Toniolo, A. Pizzariwllo, S. Susmel, F. Perennes, G. Bontempelli, J. Electroanal. Chem. 601 (2007) 1–7.
[15] S. Shahrokhian, H.R. Zare-Mehrjardi, Electrochim. Acta 52 (2007) 6310–6317.
[16] S. Roy, H. Vedala, W. Choi, Nanotechnology 17 (2006) S14–S18.
[17] J.-E. Huang, X. Hong, H.-L. Li, Carbon 41 (2003) 2731–2736.
[18] A. Wisitsoraat, A. Tuantranont, E. Comini, G. Sberveglieri, W. Wlodarski, IEEE Sensors 2007 Conf., October 28–31, 2007, IEE Sensors, 2007, pp. 550–553.
[19] Y. Wanna, N. Srisukhumbowornchai, A. Tuantranont, A. Wisitsoraat, N. Thavaungkul, P. Singjai, J. Nanosci. Nanotechnol. 6 (2006) 3893–3896.
[20] A. Wisitsoraat, A. Tuantranont, C. Thanachayanont, V. Patthanasettakul, P. Singjai, J. Electroceram. 17 (2006) 45–49.
[21] S. Chaisitsak, J. Nukeaw, A. Tuantranont, Diam. Relat. Mater. 16 (2007) 1958–1966.
[22] C. Karuwan, A. Wisitsoraat, T. Maturos, D. Phokharatkul, A. Sappat, K. Jaruwongrungsee, T. Lomas, A. Tuantranont, Talanta 79 (2009) 995–1000.
[23] J.S. Lee, G.H. Gu, H. Kim, K.S. Jeong, J. Bae, J.S. Suh, Chem. Mater. 13 (2001) 2387–2391.
[24] S.Y. Jeong, M.C. An, Y.S. Cho, D.J. Kim, M.C. Peak, K.Y. Kang, Curr. Appl. Phys. 9 (2009) S101–S103.
[25] H. Masuda, H. Yamada, M. Satoh, H. Asoh, Appl. Phys. Lett. 71 (1997) 2770–2772.
[26] M. Tian, S. Xu, J. Wang, N. Kumar, E. Wertz, Q. Li, P.M. Campbell, M.H.W. Chan, T.E. Mallouk, Nano Lett. 5 (2005) 697–703.
[27] M.-H. Spyridaki, P. Kiousi, A. Vonaparti, P. Valavani, V. Zonaras, M. Zahariou, E. Sianos, G. Tsoupras, C. Georgakopoulos, Anal. Chim. Acta 573 (2006) 242.

View Online / Journal Homepage / Table of Contents for this issue
Dynamic Article Links

Lab on a Chip

Cite this: *Lab Chip*, 2012, **12**, 133

www.rsc.org/loc

PAPER

Enhancement of DNA hybridization under acoustic streaming with three-piezoelectric-transducer system

Thitima Maturos,[a] Tawee Pogfay,[a] Kiattimant Rodaree,[a] Sastra Chaotheing,[b] Apichai Jomphoak,[a] Anurat Wisitsoraat,[a] Nattida Suwanakitti,[b] Chayapat Wongsombat,[b] Kata Jaruwongrungsee,[a] Philip Shaw,[b] Sumalee Kamchonwongpaisan[b] and Adisorn Tuantranont*[a]

Received 4th August 2011, Accepted 30th September 2011
DOI: 10.1039/c1lc20720b

Recently, we have demonstrated that DNA hybridization using acoustic streaming induced by two piezoelectric transducers provides higher DNA hybridization efficiency than the conventional method. In this work, we refine acoustic streaming system for DNA hybridization by inserting an additional piezoelectric transducer and redesigning the locations of the transducers. The Comsol® Multiphysics was used to design and simulate the velocity field generated by the piezoelectric agitation. The simulated velocity vector followed a spiral vortex flow field with an average direction outward from the center of the transducers. These vortices caused the lower signal intensity in the middle of the microarray for the two-piezoelectric disk design. On the contrary, the problem almost disappeared in the three-piezoelectric-disk system. The optimum condition for controlling the piezoelectric was obtained from the dye experiments with different activation settings for the transducers. The best setting was to activate the side disks and middle disk alternatively with 1 second activating time and 3 second non-activating time for both sets of transducers. DNA hybridization using microarrays for the malaria parasite *Plasmodium falciparum* from the optimized process yielded a three-fold enhancement of the signal compared to the conventional method. Moreover, a greater number of spots passed quality control in the optimized device, which could greatly improve biological interpretation of DNA hybridization data.

Introduction

The DNA microarray is one of the most important analysis techniques in molecular biology. This technology is used to measure changes in gene expression levels and to identify patterns of genetic variation *i.e.* single nucleotide polymorphisms (SNPs).[1] In a standard microarray experiment, the sample solution is confined in a microarray hybridization chamber by a cover slip. Inside the chamber, the target DNA diffuses all around the hybridization chamber to hybridize with complementary DNA probes fixed on a solid surface. Without active agitation, the diffusion of macromolecules such as DNA is an extremely slow process owing to the low diffusion constant (D) of DNA, which in water is typically 10^{-6} to 10^{-7} cm^2 s^{-1}, depending on DNA size, concentration and hybridization conditions.[2,3] According to the equation of diffusion length (L): $L = (Dt)^{0.5}$, the diffusion time (t) for DNA to travel over a distance of a few mm is more than 24 h.[4] Practically, diffusion-limited DNA hybridization takes 6–24 h to achieve sufficient hybridization signals and uniformity of signals across an array.[5]

Accordingly, a large number of researchers have been seeking alternative methods to enhance the hybridization, for example surface acoustic wave (SAW) based microagitation,[6] cavitational microstreaming,[7] fluid circulation and mixing,[1,2,8] rotating the hybridization chamber[9,10] and other forms of electrical enhancement.[11,12] All of these methods are based on the use of mechanical or electrical force to increase the transportation rate of the DNA molecules. Some of these methods require complicated fabrication processes, expensive devices, or modification of the DNA microarray. Acoustic streaming is another effective mixing technique applicable to microarrays. In this technique, an ultrasound wave passes through a liquid medium and transfers the momentum to the test fluid, generating a steady circular flow occurring in a high-intensity non-linear acoustic field.[13] The spatial attenuation of a wave in free space and the friction between a medium and a vibrating object are the two key mechanisms for acoustic streaming induction.[14] Another non-linear phenomenon always considered along with acoustic streaming, is the acoustic radiation force. Acoustic radiation

[a]*Nanoelectronics and MEMS laboratory, National Electronics and Computer Technology Center (NECTEC), 112 Paholyothin Rd., Klong 1, Klong Luang, Pathumthani, 12120, Thailand. E-mail: adisorn.tuantranont@nectec.or.th; Fax: +66-2-564-6756; Tel: +66-2-564-6900 ext. 2111*
[b]*National Center for Genetic Engineering and Biotechnology (BIOTEC), 113 Paholyothin Rd., Klong 1, Klong Luang, Pathumthani, 12120, Thailand; Fax: +66-2-564-6707; Tel: +66-2-564-6700*

force moves a suspending particle toward or away from acoustic pressure nodes while acoustic streaming induces the flow of the entire fluid.[13] The extent to which a particle is affected by acoustic radiation force or acoustic streaming depends on the size of the particle. Larger particles will experience a higher degree of acoustic radiation force and a lower level of acoustic streaming, respectively.[15] Acoustic streaming has been used in many applications, for example clinical analysis,[16] enhancement of heat and mass transfer[17] and fluid mixing.[3,18] It is one of the most practical fluid mixing techniques for DNA hybridization since there is no need for an external pumping unit or complicated mechanical parts for moving the microarray slide and coverslip. However, fabrication and integration of the acoustic streaming source for microarrays typically requires modification to the microarrays and coverslip,[19–21] which is impractical since DNA microarrays are typically obtained from commercial sources available in standard formats only.

Recently, we proposed a simple and low cost device for DNA hybridization based on acoustic streaming induced by two piezoelectric transducers with a coupling fluid.[22] Each piezoelectric disk, placed directly beneath each hybridization chamber, generates acoustic waves that are effectively transferred to microarrays *via* a coupling fluid. The DNA targets were observed to move in both vertical and horizontal directions under the influence of acoustic streaming facilitating hybridization with their complementary DNA probes. This scheme requires no modification of the microarray or coverslip and provides better DNA hybridization efficiency and speed compared to the conventional method of static hybridization. However, the efficiency of DNA hybridization over the whole array area is still sub-optimal. In this work, we refine the acoustic streaming system for DNA hybridization by inserting an additional piezoelectric transducer (PZT) and redesigning the locations of the transducers. The Comsol® Multiphysics software is used to design and simulate the velocity field generated by the piezoelectric agitation. DNA microarray hybridization experiments were performed using *Plasmodium falciparum* microarrays to verify the performance of the new device.

Experimental section

Design and fabrication

The schematic of the DNA hybridization device is shown in Fig.1. The device consists of three PZTs attached in aluminium chambers. Another aluminium plate, which could be screwed to the chamber, was used as a lid. An o-ring was used to provide a tight seal between chambers and the cover plate. PZTs with a diameter of 1.75 mm were activated at a resonant frequency of 1.67 MHz and operating voltage of 24 V_{rms}. The 0.8 mm deep circular wells located on top of the PZTs and two rectangular wells at both ends of the chamber were used for holding a coupling fluid and a humidity control solution, respectively. 3xSSC solution was used as a coupling fluid as well as a humidity control solution. The reasons for choosing 3xSSC solution as a coupling fluid were that it is closely matched in acoustic impedance (z) with the silica glass, it is low in heat transfer and it is non-contaminant to the hybridization process.[22] The 3-PZT design was proposed in order to improve the non-uniformity

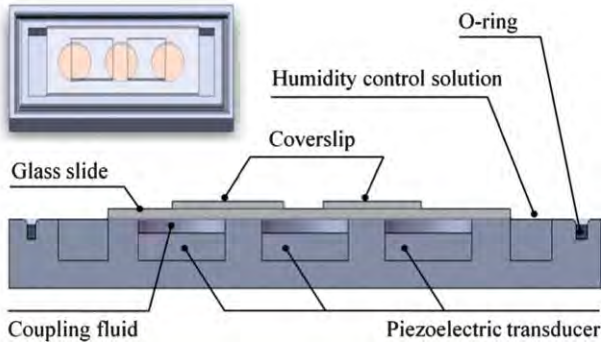

Fig. 1 Schematic showing a side view and top view of dynamic hybridization device in which DNA microarrays are placed inside the hybridization chamber above the piezoelectric ultra sonic transducers and coupling liquid. An O-ring rubber is used to provide a tight seal.

problem found from our previous design, in which microarrays were placed on top of two PZTs. It was found that signal intensity in the middle of the hybridization chamber tended to be low compared with other regions, which may have been a result of an outward flow of acoustic wave from the center of the microarray. The new device was designed to have PZTs interposed between microarrays to provide alternate agitations between both sides of the hybridization chamber and thus significantly enhance the movement of target DNA. Moreover, the new design would allow us to operate with different microarray shapes *i.e.*, the short microarray (17.5 × 19.5 mm^2) and a long microarray (17.5 × 45 mm^2). The optimum signal for each microarray could be obtained by controlling each PZT independently. It should also be noted that no more than three-piezoelectric-transducers can be used in this system because of physical constraints including the sizes of the piezoelectric disk, microarray, glass slide and chamber.

Finite element simulation

The microagitation system was designed and simulated using Comsol® Multiphysics (COMSOL Inc., Burlington, MA), a finite element method (FEM) simulation software. The 3D model for numerical simulations was constructed according to the real device dimensions. The finite elements of the structure were then built using a tetragonal mesh with ultra fine precision. The generation and propagation of acoustic waves in the structure were simulated using piezoelectric and pressure acoustic modules in Comsol® Multiphysics. The first set of governing equations used in the piezoelectric module are electromechanical equations of motion with stress-induced piezoelectric effect[23]:

$$\begin{bmatrix} \mathbf{M} & \mathbf{0} \\ \mathbf{0} & \mathbf{0} \end{bmatrix} \begin{bmatrix} \ddot{\mathbf{u}} \\ \ddot{\mathbf{v}} \end{bmatrix} + \begin{bmatrix} \mathbf{C}_m & \mathbf{0} \\ \mathbf{0} & \mathbf{0} \end{bmatrix} \begin{bmatrix} \dot{\mathbf{u}} \\ \dot{\mathbf{v}} \end{bmatrix} + \begin{bmatrix} \mathbf{K}_m & \mathbf{K}_{me} \\ \mathbf{K}_{me}^T & \mathbf{K}_e \end{bmatrix} \begin{bmatrix} \mathbf{u} \\ \mathbf{v} \end{bmatrix} = \begin{bmatrix} \mathbf{F} \\ \mathbf{L} \end{bmatrix} \quad (1)$$

$$\mathbf{T} = \mathbf{c}_E\mathbf{S} - \mathbf{e}^T\mathbf{E} \quad (2)$$

$$\mathbf{D} = \mathbf{e}\mathbf{S} + \boldsymbol{\varepsilon}_s\mathbf{E} \quad (3)$$

where $\mathbf{M}$, $\mathbf{C}_m$, $\mathbf{K}_m$, $\mathbf{K}_{me}$, $\mathbf{K}_e$, $\mathbf{u}$, $\mathbf{v}$, $\mathbf{F}$ and $\mathbf{L}$ were mass matrix, damping matrix, dielectric conductively matrix, piezoelectric

coupling matrix, stiffness matrix, spatial displacement vector, electric displacement vector, structural force vector and nodal charge vector, respectively. In eqn (2) and (3) **T**, **S** and **E** are stress, strain and electric field vectors respectively, while **e**, $\mathbf{c}_E$ and $\boldsymbol{\varepsilon}_s$ are anisotropic elastic modulus, piezoelectric constant and dielectric constant matrices, respectively. The electric potential boundary conditions applied between piezoelectric electrodes are 1.67 MHz 130 V_{rms} sinusoidal waves. The Comsol® program solves the equations in three dimensions and produces the solution of acoustic wave from displacement fields, which is coupled to the pressure acoustic modules where the propagation of acoustic wave is determined by solving Helmholtz's acoustic wave equation[15,24]:

$$\nabla\cdot(-(1/\rho_0)(\nabla p - q)) - (\omega^2/c_s^2 + \lambda^2)p/\rho_0 = Q,\ \lambda = -ik_N \qquad (4)$$

where p, ρ_0, ω, c_s, Q, q, λ and k_N are acoustic pressure wave, density of acoustic medium, angular frequency, acoustic velocity, monopole source, dipole source, eigenfrequency and normal wave number, respectively. Monopole and dipole source are absent in this case. The mechanical boundary conditions are that all surface of the device are free boundary while the side and top walls of coupling fluid chambers are hard-sound boundary where normal velocity component vanished. The COMSOL eigenvalue solver is used to determine the acoustic frequency response and acoustic wave velocity field. The acoustic simulation of the device with three-PZT agitation was made and compared to that from the previous design that contained only two PZTs.

Optimization of controlling signal

Since dramatic heat flux was generated and could denature DNA during PZT activation, transducers could not operate continuously. Thus, PZTs must be controlled to minimize heat as well as bubble generation, but maximize overall fluidic movement. For the control experiment, the transducers were turned on and off using a square wave signal and tested in three different modes. First, the side disks and the middle disk were activated alternately. Secondly, all disks were activated simultaneously and lastly each disk was activated alternately. Fluidic dye was added into hybridization chambers to observe lateral fluidic movement as a result of agitation. The on and off times for activating the disks were also varied to find an optimum condition. The optimum controlling signal that allowed the fluidic dye to flow all over the hybridization chamber rapidly, homogeneously and coldly are used in the hybridization experiment.

DNA hybridization experiment

The hybridization experiments were then performed using two- and three-piezo hybridization devices and compared with the conventional static method. The DNA microarrays were fabricated on polylysine-coated glass slides using a new generation ultrafast, linear servo driven DeRisi microarrayer, controlled by ArrayMaker software (http://derisilab.ucsf.edu/microarray/software.html). The DNA microarray was printed on a glass substrate with a total area of 17.5 × 19.5 mm^2. The microarray contained 8088 features with a printed long oligonucleotide probe (70 bases in length). The probes covered the malaria parasite *Plasmodium falciparum* genome. The target DNAs were cDNAs, which were transcribed from total RNA.

There were two different cDNA samples, one labeled with Cy3 dye and the other labeled with Cy5 dye (Amersham Biosciences) as described previously.[25] The experiments were conducted with the same cDNA quantity (5 pmol) and hybridized for 16 h at 42 °C. After hybridization, the arrays were washed, dried and stored in a cool dark place before analysis. All scanning was done on the same day and all scans were done using the same laser power and PMT gain settings (100%, Cy5 PMT = 560 V, and Cy3 PMT = 490 V respectively). Microarray scanning and image analysis was done on a GenePix400B scanner and spot intensities were quantified using GenePix Pro 6.0 Software (Axon Instrument, Inc). Filtering to distinguish good/effective spots was done using the signal-to-noise ratio (SNR) ≥ 3 reported by GenePixPro, which follows the recommendation made by Yatskou *et al.*[26] for DNA microarray data. Kernel density plots and subarray boxplots were carried out using the R interpreter software.

Results and discussion

Flow field in hybridization chamber

The velocity vector fields from acoustic simulation of the device with 2-PZT and 3-PZT agitation systems are illustrated in Fig. 2. The results of the 2-PZT agitation system are demonstrated when only the left PZT is activated while the results of the 3-PZT agitation system are demonstrated in the mode in which two side PZTs are activated and the center PZT is off. These settings represent typical conditions used in experiments. Comparing the top view of the velocity vector field of 2-PZT and 3-PZT systems (Fig. 2A–B), it is evident that the velocity vector field on the square hybridization area of the 2-PZT system is considerably weaker than that of the 3-PZT system. Thus, agitation by the 3-PZT system is much more effective. From the enlarged 3D view of the velocity vector field of the 2-PZT and 3-PZT systems (Fig. 2C–D), a spiraling vortex 3D streaming flow with a source located approximately in the middle of the PZT is formed in both cases. The spiral flow is in the direction outward from the center of the PZT. For the 2-PZT case, each PZT is concentric with the microarray. Thus, DNA particles will move very slowly (almost stationary) around the center of microarray, however there is much more movement toward the edges. The results can explain our previous experimental observation that the hybridization intensity on the edge of microarrays was often observed to be much greater than on the central region. In the 3-PZT design, each microarray is interposed between two PZTs. Hence, each edge of a microarray can receive the outward spiral flow with strong velocity field from the PZT on each side as shown in Fig. 2D. However, it should be noted that if the spiral fields from PZTs on both sides appear simultaneously, undesirable standing wave will occur from the simulation of two opposing waves. Thus, PZTs on either side should not be activated concurrently. Therefore, the 3-PZT design with alternate PZT activation should be able to circumvent the problem of low hybridization intensity at the microarray center in 2-PZT design.

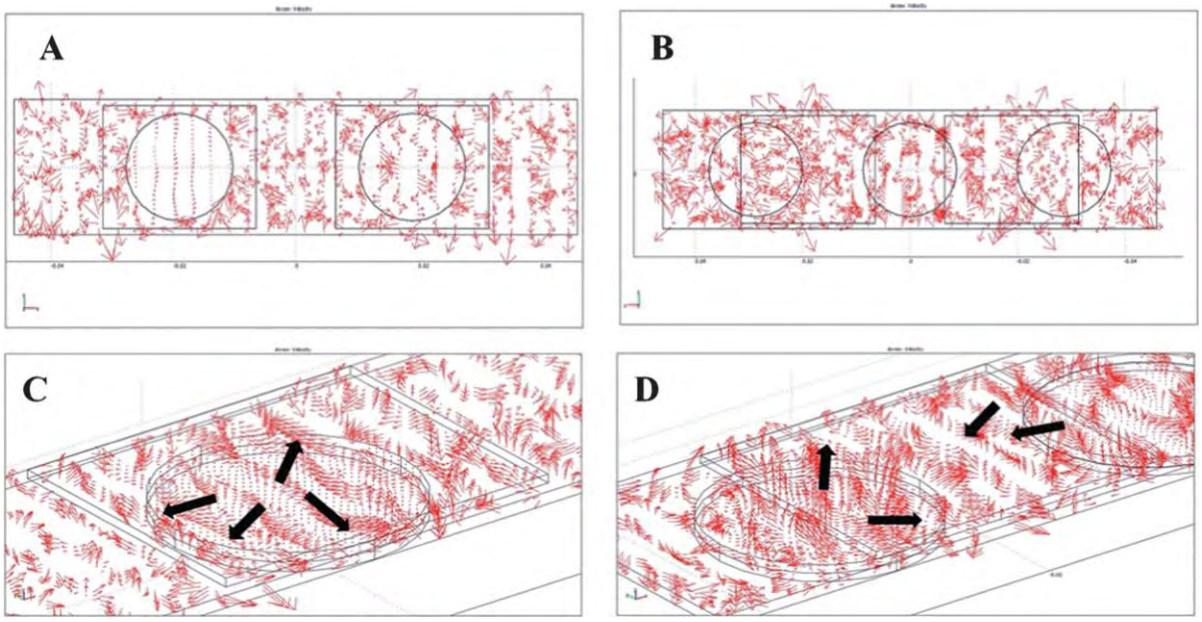

Fig. 2 Top view of velocity vector field of (A) the 2-PZT system when the left PZT is activated and (B) the 3-PZT system when two side PZTs are activated. The corresponding 3D views of the velocity vector field of the (C) 2-PZT and (D) 3-PZT systems.

Operating signal optimization

From the control experiments, three PZTs were initially tested in three different modes without non-activating time between consecutive transducer activations. It was found that the fluidic dye could cover the entire hybridization chamber within 5 min when the side disks and the middle disk were alternately activated. However, similar coverage would take 10 min and 14 min when operating all three PZTs simultaneously and activating each PZT alternately, respectively. Thus, the results agree with the prediction from the simulation that a standing wave would occur and deter fluid mixing when operating all PZTs simultaneously. Therefore, the best activation mode is confirmed to be operating the middle and side PZTs alternately. However, it was found that excessive heat was generated due to the lack of non-activating time between consecutive transducer activations. Thus, non-activating time was added and on-off activating signals were varied to optimize fluidic movement, total operating time and heat generation. Lower heat generation could be observed with less bubble generation in the fluid after adding non-activating time. The optimum activating and non-activating times were found to be 1 and 3 s, respectively. The condition was proven to be suitable in terms of heat reduction and overall fluid movement. The optimum agitation by 3-PZT system allowed the fluidic dye to fill the entire chamber as illustrated in Fig. 3B within 15 min, while it took more than 30 min for the dye to cover half of the chamber as shown in Fig. 3A for the static case (all PZTs off).

Enhancement of microarray hybridization efficiency

The hybridization efficiency of our device was compared with the conventional static hybridization method. The hybridization experiments were performed on a microarray with corresponding biological cDNA samples. The fluorescent scanned images of microarrays hybridized with or without piezoelectric agitation, are shown in Fig. 4. The signals are consistent across both arrays, although the signal overall for the piezoelectric hybridization appears stronger relative to conventional hybridization. For microarray data analysis, spot quality control is a crucial part to

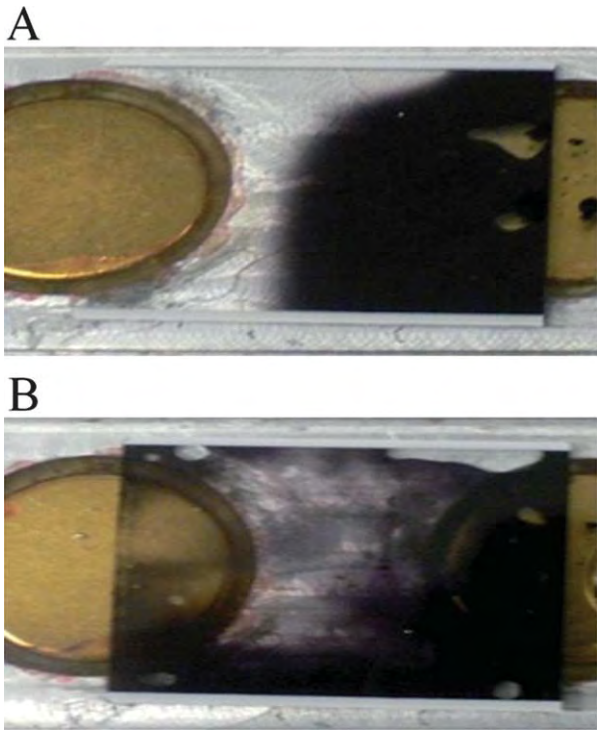

Fig. 3 Photographs of dye solution mixing in the hybridization microchamber (A) without acoustic streaming (PZT off) and (B) with the PZT agitation at 1.67 MHz and 24 Vrms.

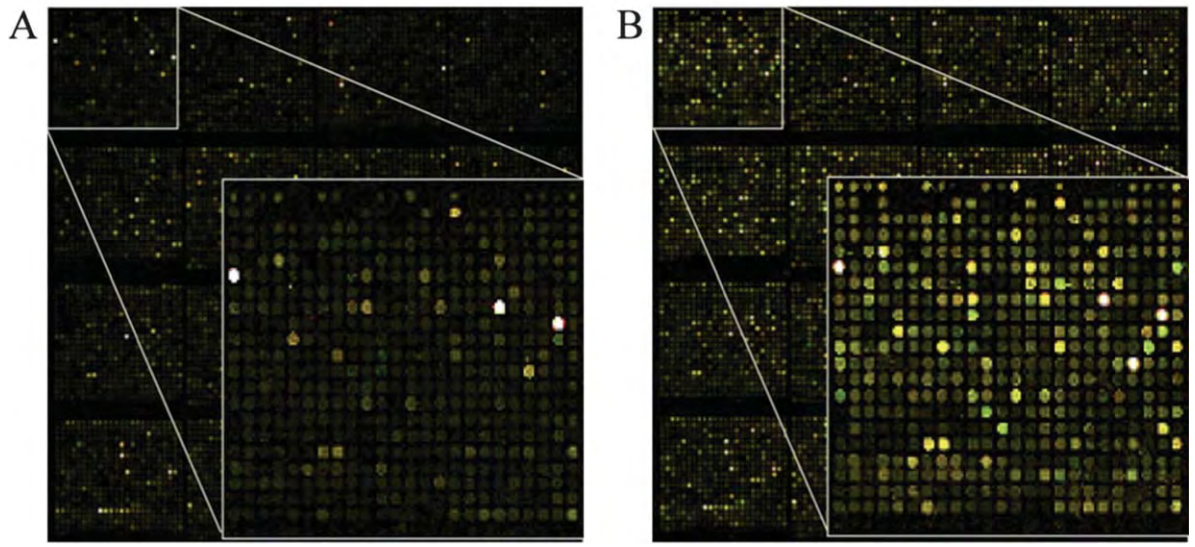

Fig. 4 Microarray scan pictures of *P. falciparum* DNA microarrays with (A) 16 h static hybridization, and (B) 16 h 3-PZT dynamic hybridization.

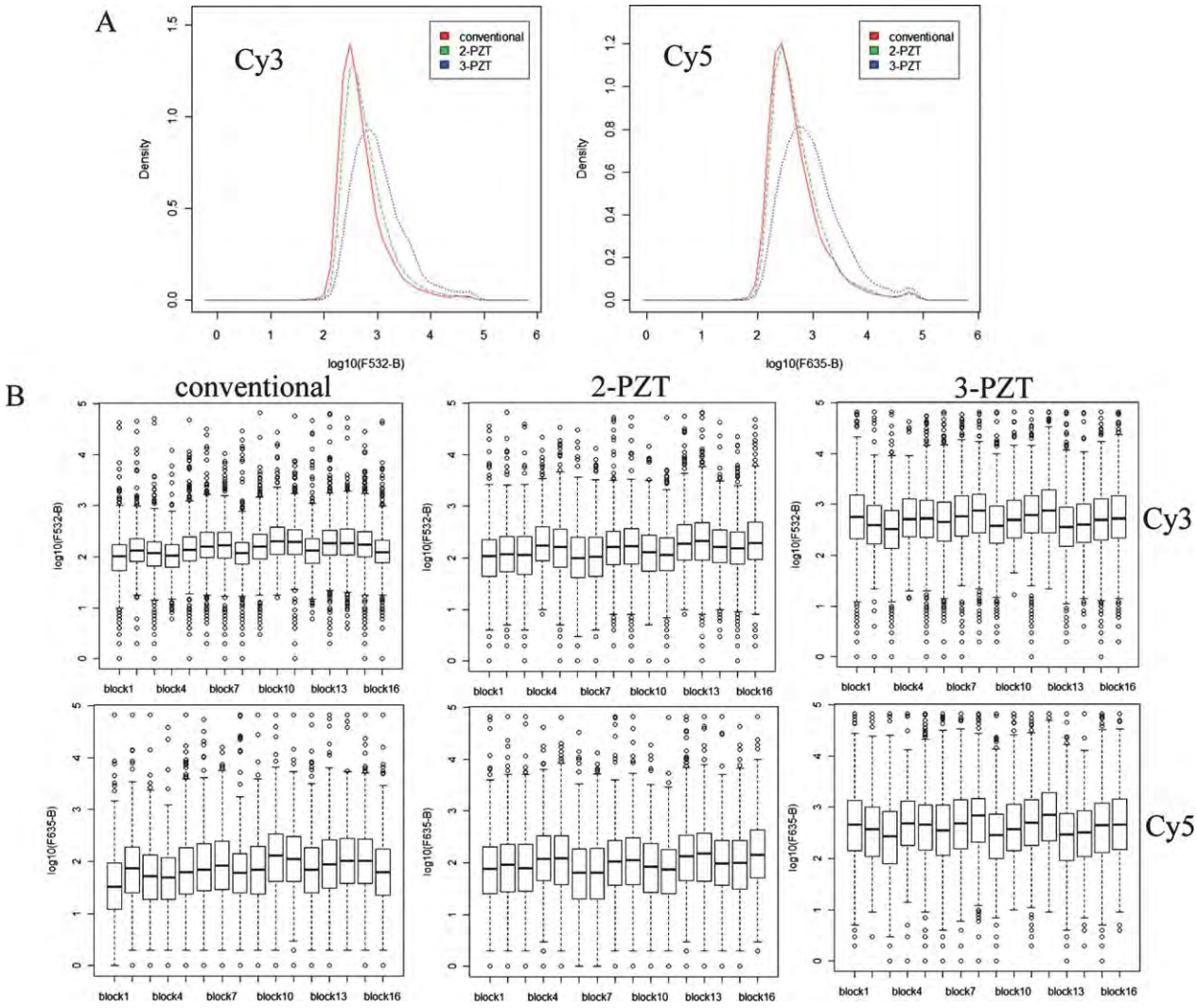

Fig. 5 (A) Kernel density plots (normalized density *vs.* background-corrected fluorescence intensity (log scale) for the spots in Cy3 (532 nm) and Cy5 (635 nm) channels) obtained from hybridization experiments using conventional, 2-PZT and 3-PZT systems and (B) corresponding subarray box plots (background-corrected fluorescence intensity (log scale) distribution for 16 subarrays). Thick line in each box represents median intensity.

distinguish between good/effective spots from bad ones that may represent biologically irrelevant noise. We found that more spots pass filtering for agitated 2-PZT and 3-PZT relative to conventional hybridization (2720, 5560, and 2414 spots respectively). Thus, our 3-PZT system can significantly increase the number of effective spots over the previous 2-PZT system and static hybridization. As a result, our new agitation system could increase the detection sensitivity for DNA targets that may have produced low hybridization signals (due to their low expression level) but were biologically relevant. The power of discovering more effective spots would be extremely beneficial in many kinds of transcriptomic profiling studies because it would produce better microarray interpretation. The greater number of good spots for agitated hybridization cover a broader range of signal intensities, especially for the 3-PZT hybridization, as shown by the kernel density distribution plots for the Cy3 and Cy5 channels (Fig. 5A).

In order to demonstrate that the hydridization efficiency of the 3-PZT is consistent across the array, the fluorescent signals within each of the 16 subarrays were compared. The boxplots of fluorescent intensity shown in Fig. 5B indicate that the ranges of intensities within each subarray are comparable, with no noticeable bias in different regions of the array. A rigorous statistical analysis was not performed though, since the subarrays contain different probes corresponding to genes expressed at different levels. Moreover, the printing of probes on the array is not random *e.g.* the bottom row of each subarray is mostly empty. Consistent hybridization across the array also requires careful application of the labeled DNA solution and coverslip, which can be a major source of operator error. To overcome this problem, semi-automated delivery systems could be incorporated into the 3-PZT device, such as used in the MAUI commercial system (BioMicro systems USA).

Conclusions

In conclusion, we have developed a new three-PZT design for a low-cost dynamic acoustic streaming-based DNA hybridization system. The new acoustic streaming design is modified from the previously developed 2-PZT system by inserting an additional piezoelectric transducer and redesigning the locations of the transducers. The design is assisted by acoustic simulations using Comsol® Multiphysics. Our static *versus* dynamic hybridization comparison under 'real' microarray experimental parameters demonstrated that the newly designed dynamic hybridization system provides significantly higher average fluorescent signal intensities in both Cy3 and Cy5 channels than the conventional static hybridization and the previous 2-PZT design. This allows more effective spots to be included in the subsequent microarray data analysis, and potentially greater power to detect biologically significant signals, especially those in the lower range.

Acknowledgements

We would like to thank Drs Joseph Derisi and Jennifer Shock at the University of San Francisco for providing the oligo-set, training and facilities for the production of DNA microarray slides, through generous support from the Howard Hughes Medical Institute (HHMI, USA). S.K. is an international research scholar of HHMI, USA. A.T. expresses his great gratitude to the Thailand Research Fund (RSA5380005) for a research career development grant.

Notes and references

1 H. H. Lee, J. Smoot, Z. McMurray, D. A. Stahl and P. Yager, *Lab Chip*, 2006, **6**, 1163–1170.
2 M. K. McQuain, K. Seale, J. Peek, T. S. Fisher, S. Levy, M. A. Stremler and F. R. Haselton, *Anal. Biochem.*, 2004, **325**, 215–226.
3 R. H. Liu, J. Yang, M. Z. Pindera, M. Athavale and P. Grodzinski, *Lab Chip*, 2002, **2**, 151–157.
4 J.-M. Hertzsch, R. Sturman and S. Wiggins, *Small*, 2007, **3**, 202–218.
5 M. Schena, *Microarray Biochip Technology*, Eaton Publishing Company, California, 2000.
6 A. Toegl, R. Kirchner, C. Gauer and A. Wixforth, *J Biomol Tech.*, 2003, **14**, 197–204.
7 R. H. Liu, R. Lenigk, R. L. Druyor-Sanchez, J. Yang and P. Grodzinski, *Anal. Chem.*, 2003, **75**, 1911–1917.
8 P. K. Yuen, G. Li, Y. Bao and U. R. Muller, *Lab Chip*, 2003, **3**, 46–50.
9 J. Vanderhoeven, K. Pappaert, B. Dutta, P. Van Hummelen and G. Desmet, *Anal. Chem.*, 2005, **77**, 4474–4480.
10 M. A. Bynum and G. B. Gordon, *Anal. Chem.*, 2004, **76**, 7039–7044.
11 C. Gurtner, E. Tu, N. Jamshidi, R. W. Haigis, T. J. Onofrey, C. F. Edman, R. Sosnowski, B. Wallace and M. J. Heller, *Electrophoresis*, 2002, **23**, 1543–1550.
12 C. Chii-Chang, K. Wei-Chu, C. Sung-Kay and T. Chi-Meng, *Enhancement of DNA hybridization efficiency using photovoltaic effect*, 2003.
13 T. Uchida, T. Suzuki and S. Shiokawa, *Investigation of acoustic streaming excited by surface acoustic waves*, 1995.
14 C. P. Lee and T. G. Wang, *Outer acoustic streaming*, ASA, 1990.
15 S. M. Hagsater, T. G. Jensen, H. Bruus and J. P. Kutter, *Lab Chip*, 2007, **7**, 1336–1344.
16 X. Shi, R. W. Martin, S. Vaezy and L. A. Crum, *J. Acoust. Soc. Am.*, 2002, **111**, 1110–1121.
17 E. H. Trinh and J. L. Robey, *Experimental study of streaming flows associated with ultrasonic levitators*, AIP, 1994.
18 C. Suri, K. Takenaka, H. Yanagida, Y. Kojima and K. Koyama, *Ultrasonics*, 2002, **40**, 393–396.
19 Z. Guttenberg, H. Muller, H. Habermuller, A. Geisbauer, J. Pipper, J. Felbel, M. Kielpinski, J. Scriba and A. Wixforth, *Lab Chip*, 2005, **5**, 308–317.
20 A. Wixforth, C. Strobl, C. Gauer, A. Toegl, J. Scriba and Z. v. Guttenberg, *Anal. Bioanal. Chem.*, 2004, **379**, 982–991.
21 Z. Pan, Y. Li, D. Zhou, J. Tang, M. Zhang, P. Xiao and Z. Lu, *Anal. Biochem.*, 2008, **376**, 280–282.
22 K. Rodaree, T. Maturos, S. Chaotheing, T. Pogfay, N. Suwanakitti, C. Wongsombat, K. Jaruwongrungsee, A. Wisitsoraat, S. Kamchonwongpaisan, T. Lomas and A. Tuantranont, *Lab Chip*, 2011, **11**, 1059–1064.
23 F. Lu, H. P. Lee, P. Lu and S. P. Lim, *Sens. Actuators, A*, 2005, **119**, 90–99.
24 S. Mohamady, R. K. Raja Ahmad, A. Montazeri, R. Zahari and N. A. Abdul Jalil, *Advances in Acoustics and Vibration*, 2009, **2009**, 1–10.
25 Z. Bozdech, J. Zhu, M. Joachimiak, F. Cohen, B. Pulliam and J. DeRisi, *GenomeBiology*, 2003, **4**, R9.
26 M. Yatskou, E. Novikov, G. Vetter, A. Muller, E. Barillot, L. Vallar and E. Friederich, *BMC Res. Notes*, 2008, **1**, 80.

Sensors and Actuators B 161 (2012) 549–555

Contents lists available at SciVerse ScienceDirect

Sensors and Actuators B: Chemical

journal homepage: www.elsevier.com/locate/snb

Inkjet-printed graphene-poly(3,4-ethylenedioxythiophene):poly(styrene-sulfonate) modified on screen printed carbon electrode for electrochemical sensing of salbutamol

Chanpen Karuwan, Chakrit Sriprachuabwong, Anurat Wisitsoraat, Ditsayut Phokharatkul, Pornpimol Sritongkham, Adisorn Tuantranont*

Nanoelectronics and MEMS Laboratory, National Electronics and Computer Technology Center, 112 Thailand Science Park, Phahon Yothin Rd., Klong 1, Klong Luang, Pathumthani 12120, Thailand

ARTICLE INFO

Article history:
Received 4 August 2011
Received in revised form 13 October 2011
Accepted 31 October 2011
Available online 6 November 2011

Keywords:
Inkjet printing
Graphene-poly(3,4-ethylenedioxythiophene):poly(styrene-sulfonate)
Screen printed carbon electrode
Salbutamol
Electrochemical sensing

ABSTRACT

In this work, a simple and sensitive inkjet-printed graphene-poly(3,4-ethylenedioxythiophene): poly(styrene-sulfonate) (GP-PEDOT:PSS) on screen printed carbon electrode (SPCE) is developed for detection of salbutamol (SAL), a prohibited drug in sport. GP-PEDOT:PSS dispersed solution is prepared for use as an ink by one-step electrolytic exfoliation from a graphite electrode. GP-PEDOT:PSS layers are then printed on SPCEs by dimatrix inkjet material printer and their electrochemical behaviors are characterized. It is found that SAL oxidation peak responses of PEDOT:PSS modified and GP-PEDOT:PSS modified SPCE electrodes are approximately 30 and 150 times higher than that of unmodified SPCE, respectively. In addition, excellent analytical features with a wide dynamic range of 500 μM, a low detection limit (3S/N) of 1.25 μM and low matrices' interference in pharmaceutical samples have been achieved. Therefore, inkjet-printed GP-PEDOT:PSS SPCE is a promising candidate for advanced electrochemical sensing applications.

1. Introduction

Graphene is a two-dimensional nano-carbon material with a honeycomb lattice structure that exhibits exceptional physical, chemical and electronic properties. It is thus a potential candidate for a number of electronic applications including field-effect and single-electron transistors [1,2], memory devices [3], solar cells [4] and electrochemical sensors [4–10]. In particular, it is highly advantageous for electrochemistry due to its very large two-dimensional electrical conductivity, excellent electron transfer rate and huge specific surface area. Some recent studies have demonstrated that the electrochemical sensitivity of graphene based electrodes is superior to those of single-walled carbon nanotubes (SWCNTs) [9] and glassy carbon electrode (GCE) [10] because of its larger number of edge plane per unit mass. In addition, it is considered more practical than SWCNTs counterpart because it can be inexpensively produced from low-cost graphite with no metallic impurity [10]. Metallic impurities commonly found in CNTs can induce anomalous electrochemical reactions, causing serious interference problems.

Graphene may be synthesized by several methods including micromechanical cleavage, epitaxial growth via ultra-high vacuum graphitation, chemical synthesis through oxidation of graphite, chemical vapor deposition (CVD), solvothermal synthesis and electrolytic exfoliation [11]. Among these, electrolytic exfoliation is particularly promising because it can produce stable graphene nanosheets in aqueous solution at low cost and may easily be scaled up for large-scale production. Moreover, it is the most suitable route for the formation of graphene in conducting polymer matrix, which can be highly useful for electrochemical transduction and bio-receptor immobilization. Conducting polymers including polythiophene [12], polyaniline [13] and polypyrrole [14] have also attracted much interest in electroanalysis due to their good electrical conductivity and electrochemical stability.

Poly(3,4-ethylenedioxythiophene):poly(styrene-sulfonate) acid (PEDOT:PSS), an important derivative of polythiophene, is an attractive working electrode material for electroanalysis because of its high conductivity, low redox potential, high electrochemical, ambient and thermal stability [15]. PEDOT:PSS may be deposited on a transducer surface by solvent casting, dip coating, spin coating or inkjet printing [15–17]. Inkjet-printing technology is a relatively new non-contact deposition method that is highly suitable for organic based microelectronic fabrication owing to

* Corresponding author.
E-mail address: adisorn.tuantranont@nectec.or.th (A. Tuantranont).

0925-4005/$ – see front matter © 2011 Elsevier B.V. All rights reserved.
doi:10.1016/j.snb.2011.10.074

its micro-patterning capability, simple application procedure, low temperature processing and relatively low-cost instrumentation. Recently, inexpensive and disposable chemical/biosensors fabricated by inkjet printing have been demonstrated [18,19].

In this work, an electrochemically synthesized graphene-PEDOT:PSS (GP-PEDOT:PSS) is employed for the first time to modify screen printed carbon paste electrode (SPCE) by inkjet-printing technique. The inkjet-printed GP-PEDOT:PSS electrode is then applied for electrochemical detection of salbutamol by cyclic voltammetry (CV) and its performances are compared to PEDOT:PSS modified and unmodified SPCE. Salbutamol or [2-(tert-butylamino)-1-(4-hydroxy-3-hyroxymethyl) phenylethanol] is of interest because it is the most widely used β_2-adrenergic receptor agonist for curing bronchial asthma and other allergic diseases [20,21] while it is also a banned drug for athletes and a prohibited food additive. Due to its importance, electrochemical detections of salbutamol have been widely investigated as an alternative determination method to standard analysis techniques including mass spectrometry [22,23] and UV–vis spectroscopy [24]. Over the past decade, electrochemical detections of salbutamol by glassy carbon [25], carbon paste [26], boron-doped diamond [27], CNTs [28,29] and graphite nanosheet modified electrodes [30] have been presented. However, there has been no report of its electrochemical detection by a GP-PEDOT:PSS modified electrode.

2. Materials and methods

2.1. Materials and apparatus

All of chemicals used in this work were analytical grade. Standard solutions of salbutamol were purchased from Sigma (USA). Phosphate buffer solution (pH 5.8–8.0) was made from sodium dihydrogen phosphate (Fluka, Switzerland) and disodium hydrogen phosphate (Fluka). The stock solution of salbutamol (0.01 mol l^{-1}) was prepared by dissolving 0.03 g of salbutamol in deionized distilled water. Graphite rods (1/4″ dia, Electron Microscopy Science) were used as starting material for graphene synthesis. A commercial PEDOT:PSS solution (clevios P jet N from HC Starck, USA) was utilized as an electrolyte for electrolytic exfoliation. SPCE electrodes were fabricated in-house at King Mongkut University of Technology at Thonburi, Thailand. An inkjet printer (Fujifilm Dimatix Materials Printer) was employed for printing of GP-PEDOT:PSS layers on SPCEs. A potentiostat (μ-autolab Type III, Metrohm, Switzerland) and a home-made electrochemical cell comprising a 3 ml cylindrical acrylic cell, a GP-PEDOT:PSS working electrode, a platinum (Pt) wire counter electrode and a silver/silver chloride (Ag/AgCl) reference electrode were used for all CV measurements.

2.2. Graphene synthesis

Two graphite rods were placed in an electrolysis cell filled with PEDOT:PSS electrolyte and a constant potential of 8 V was applied between electrodes using Keithley 2420 Source Meter. The anode was corroding and black precipitate was gradually formed in the reactor. The electrolysis was conducted for 5 h to obtain stable GP-PEDOT:PSS dispersion with a suitable graphene concentration. The dispersed product was centrifuged at 1200 rpm to separate large agglomerates and supernatant portion of the dispersion was decanted. The morphology and structure of graphene dispersed in the solution were characterized by transmission electron microscope (JEOL model JEM-2010) and confocal Raman spectroscope (NT-MDT model Ntegra Spectra). TEM samples were prepared by drop-coating of graphene-PEDOT/PSS solution on a carbon/copper grid while Raman and FTIR samples were washed graphene and unwashed graphene-PEDOT/PSS powders extracted from the solution.

2.3. Inkjet printing of GP-PEDOT:PSS electrodes

The GP-PEDOT:PSS solution was used as an ink for inkjet printing. The ink was loaded into a cartridge and printed on SPCE by the commercial material inkjet printer. One to five layers of GP-PEDOT:PSS material were printed on SPCE over an area of 3 mm × 5 mm. The surface morphology and functional group of GP-PEDOT:PSS printed films were characterized by scanning electron microscope (SEM, Hitachi model S-4700) and Fourier transform infrared spectroscopy (FTIR, Perkin Elmer model spectrum spot light-300), respectively.

2.4. Electrochemical measurement

The electrochemical characteristics of inkjet-printed GP-PEDOT:PSS modified SPCEs were measured by CV using the commercial electrochemical work station and home-made electrochemical cell. Salbutamol solutions with different concentrations

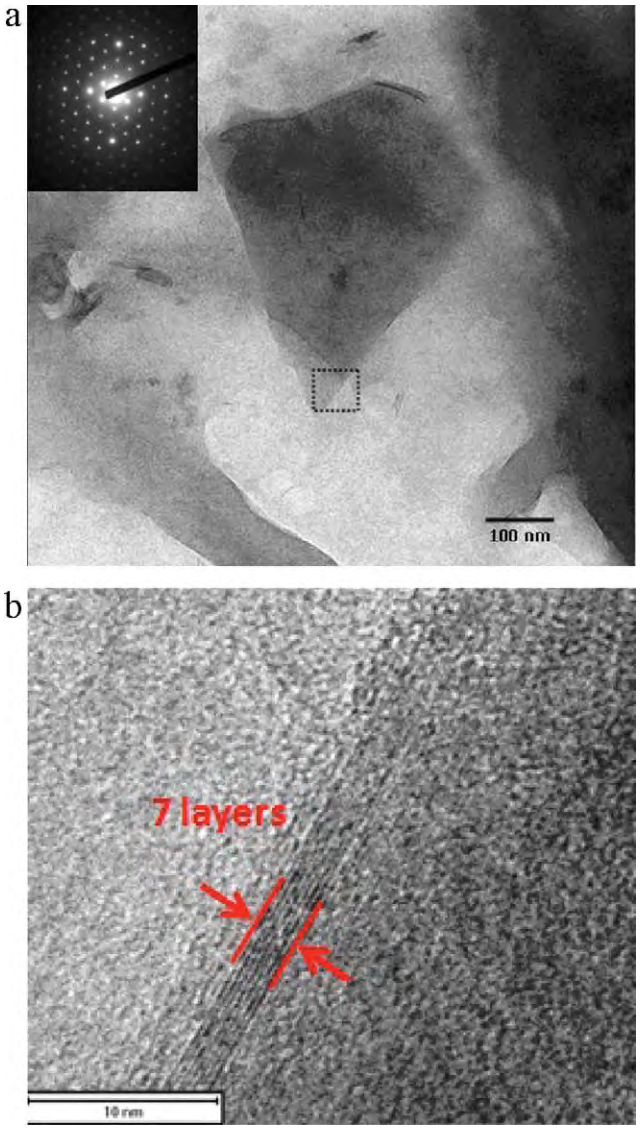

Fig. 1. (a) Bright field TEM image and (b) high-resolution TEM images of graphene sheet in GP-PEDOT:PSS composite. Inset: selected area electron diffraction pattern of a region near an edge of graphene sheet.

were then prepared for concentration study by proper dilution of the stock solution. Working electrode was immersed in salbutamol solutions and CV scans were run at several scan rates for different concentrations of salbutamol. The voltage window for CV was from +0.3 to +0.9 V because the oxidation peak of salbutamol appeared within this potential range.

3. Results and discussion

3.1. Morphological and structural characteristics of GP-PEDOT:PSS

The detailed structure of graphene dispersed in PEDOT:PSS solution was identified and characterized by TEM and confocal Raman spectroscopy. Fig. 1(a) shows a typical bright field TEM image of GP-PEDOT:PSS composite. It can be seen that it contains polygon sheets with unequal sides mixed and surrounded by very smooth material. In addition, polygon sheets are seen to have some thickness variation, suggesting more than one overlapping material layers. Their average diameter is estimated to be around 500 nm. The polygon sheet is confirmed to be graphene by selected area electron diffraction (SAED) from a region near an edge of a sheet as demonstrated in the inset of Fig. 1(a). The electron diffraction pattern is very well matched to that of standard single crystal graphite. Thus, the thin polygon sheet is affirmed to be graphene. Fig. 1(b) shows a typical high resolution TEM image of the exfoliated graphene sheet. The graphitic fringes observed on the edge confirm that the synthesized structure is multi-layer graphene with approximately seven sp^2-bonded carbon layers. The term, *graphene*, can thus be used because graphitic sheet with the number of sp^2-bonded carbon layers of less than ten still exhibits two-dimensional properties [31].

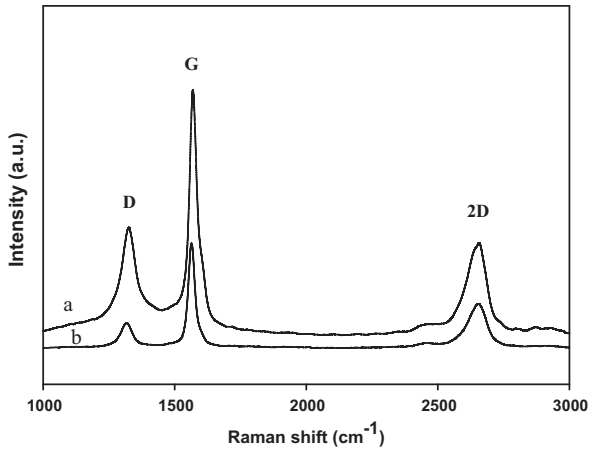

Fig. 2. (a) Raman spectra from graphene powder extracted from GP-PEDOT:PSS composite and (b) Raman spectra of graphite powder.

Fig. 2 demonstrates Raman spectra from extracted graphene powder and standard graphite. It can be seen that D, G and 2D bands (at ~1330, ~1574 and ~2648 cm^{-1}, respectively) of synthesized graphene and graphite are considerably different. The G peak, which arises from the in-plane vibration of sp^2 bonds, of graphene powder is relatively broader than that of graphite. In addition, the graphene powder shows relatively strong D and 2D bands compared to graphite, indicating partially disordered crystal structure of graphene sheet with larger numbers of edge-plane and zone-boundary defects, respectively [32]. Moreover, 2D band of graphene powder is relatively broad compared to G band, confirming that synthesized structure is multi-layer graphene [31].

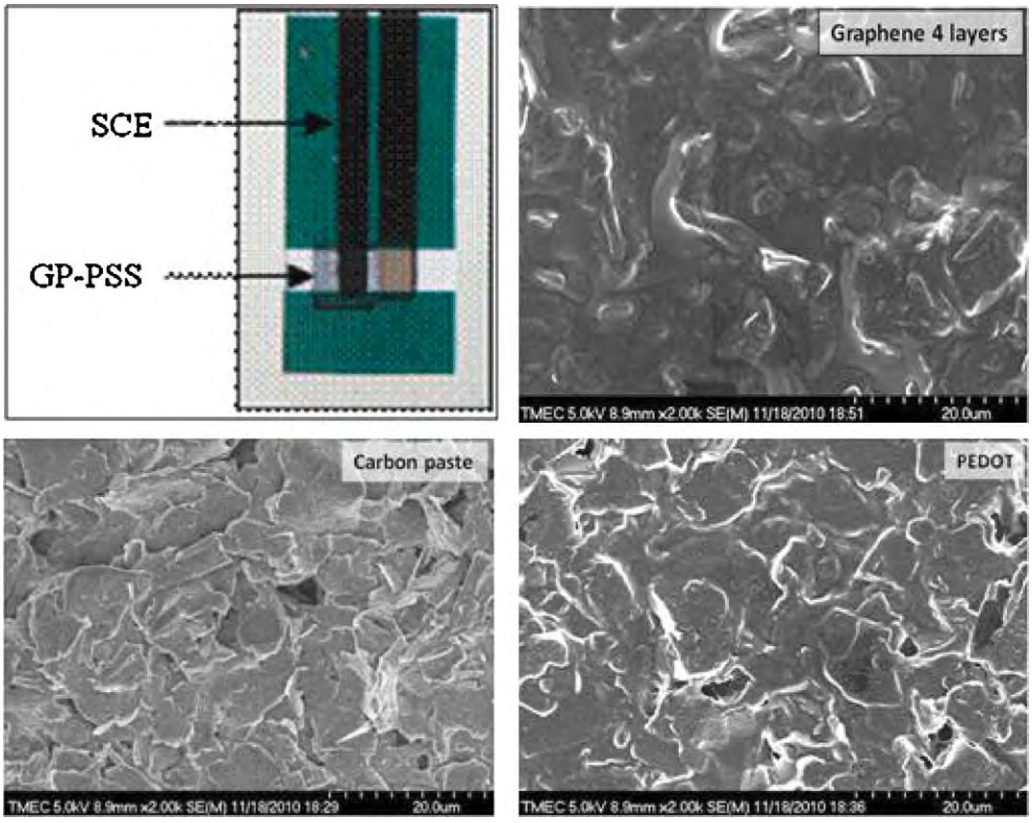

Fig. 3. Photograph of fabricated electrode and SEM micrographs of SPCE, inkjet-printed PEDOT:PSS on SPCE and printed GP-PEDOT:PSS on SPCE.

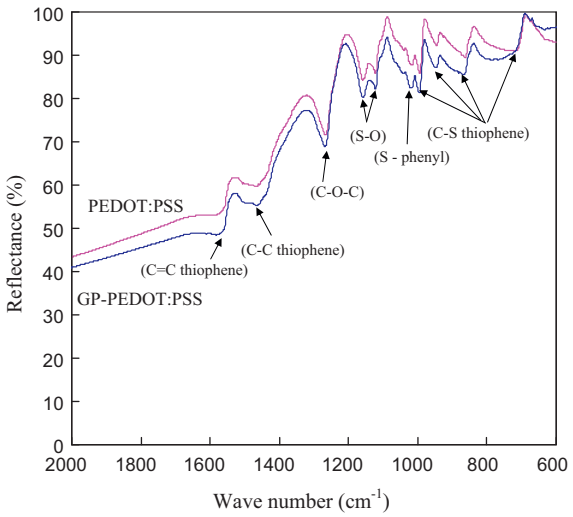

Fig. 4. FTIR spectra of (a) GP-PEDOT:PSS and (b) PEDOT layers on SPCEs.

The surface morphologies of fabricated electrochemical electrodes were examined by SEM. Fig. 3 includes a photograph of fabricated electrodes and SEM micrographs of unmodified SPCE, inkjet-printed PEDOT:PSS SPCE and inkjet-printed GP-PEDOT:PSS SPCE. It can be seen that uncoated SPCE has rough surface with large grains of several microns in size and the surface is smoothen after inkjet printing with PEDOT:PSS or GP-PEDOT:PSS layers. However, graphene structures are not clearly observed on the SPCE surface because graphene sheet (~0.5 μm in diameter) is very small compared to the surface roughness and grain of SPCE.

The functional groups of inkjet-printed PEDOT:PSS and GP-PEDOT:PSS films were characterized by FTIR and the FTIR spectra are illustrated in Fig. 4. It can be seen that both spectra contain peaks of S–O and S–phenyl bonds in sulfonic acid at 1157, 1121 and 1012 cm^{-1} and peaks of C=C, C–C and C–S bonds in thiophene backbone at 1532, 1356, 952, 845 and 704 cm^{-1}, respectively. Thus, both films contain the same expected functional groups of PEDOT:PSS copolymer. Nevertheless, GP-PEDOT:PSS film exhibits approximately 5% lower IR reflectance than PEDOT:PSS film does. Therefore, graphene causes small IR broadband absorption but does not contribute any additional functional group to the mixture. The result indicates that the structure formed in the solution by electrolytic exfoliation is indeed graphene not graphene oxide, which would otherwise show C–O and C=O peaks between 1600–1800 cm^{-1}.

3.2. Performance of GP-PEDOT:PSS and SPCE electrodes

The electrochemical efficacy of GP-PEDOT:PSS electrode was evaluated from CV response in 1 mM salbutamol solution and compared to those of PEDOT:PSS modified and unmodified SPCEs as shown in Fig. 5. It is evident that GP-PEDOT:PSS modified SPCE exhibits much larger irreversible oxidation peak at ~0.78 V than those of PEDOT:PSS modified and unmodified SPCEs, respectively. The oxidation peak of salbutamol at ~0.78 V has been explained by oxidative reaction of phenolic hydroxyl group [27]. From the CV responses, the oxidation peak amplitudes of PEDOT:PSS modified and GP-PEDOT:PSS modified SPCEs are approximately 30 and 150 times higher than that of unmodified SPCE, respectively. Thus, PEDOT:PSS considerably enhances the electrochemical activity of SPCE to salbutamol and the addition of graphene greatly increases the response further. The dramatic enhancement can be attributed to huge reactive surface area, high electronic mobility and excellent electron transfer rate of PEDOT:PSS and graphene composite.

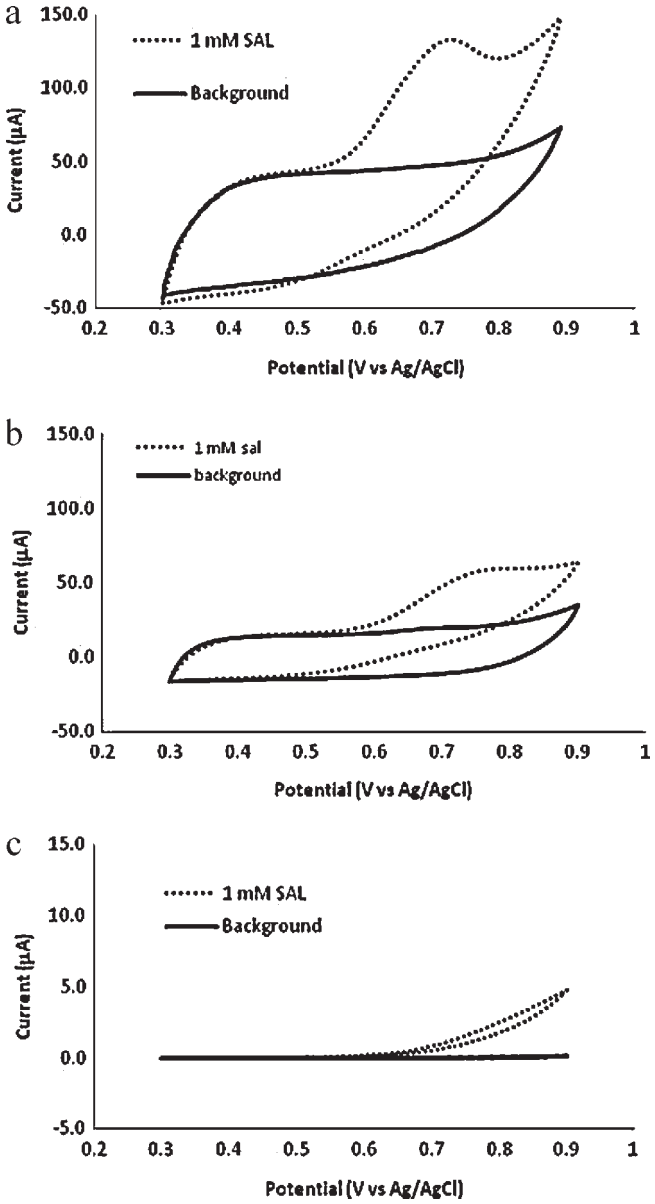

Fig. 5. The oxidation of 1 mM salbutamol on (a) GP-PEDOT:PSS and (b) PEDOT electrode and (c) SPCE electrode. Scan rate was 100 mV s^{-1}. Buffer solution was 50 mM phosphate buffer (pH 7.0).

3.3. Effect of buffer

The CV responses of GP-PEDOT:PSS modified SPCE electrode were measured in 0.5 mM salbutamol solutions in phosphate buffers with different pHs ranging from 5.8 to 8.0 as shown in Fig. 6. It can be seen that the oxidation peak amplitude increases as pH value increases from 5.8 to 7.0 and then decreases as pH value increases further. In addition, it can be noticed that the potential at oxidation peak is monotonically reduced as pH value increases. The pH value of 7.0 is seen as an optimal condition that yields the highest electrochemical response. The result suggests that solubility dissociation and diffusion of salbutamol in PBS buffer is maximized at pH value of 7.0, resulting in an optimal electrochemical sensitivity. This pH value is thus used in all subsequent CV measurement.

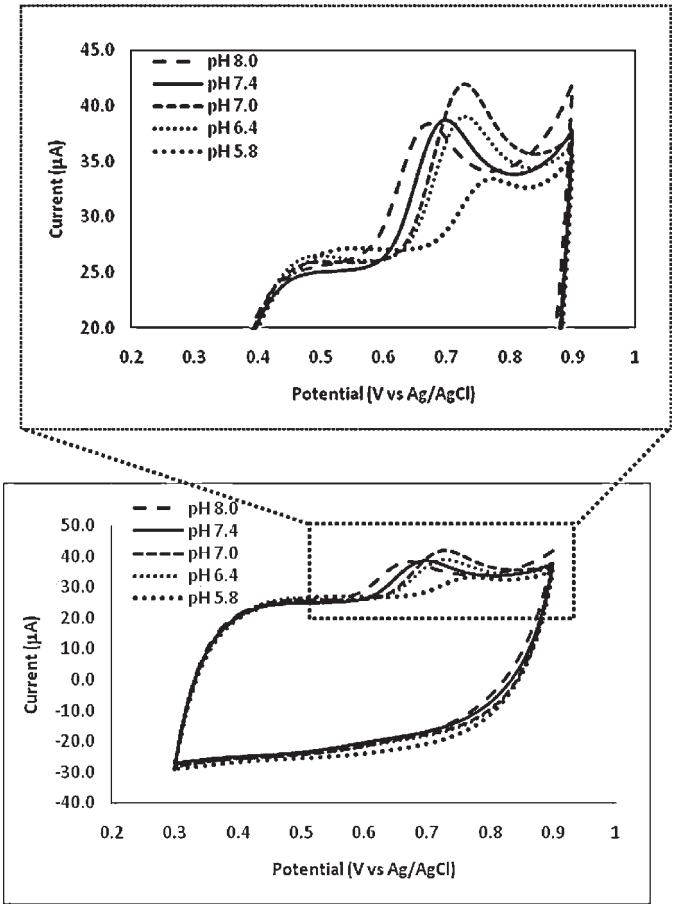

Fig. 6. Cyclic voltammograms obtained at various pHs of 0.5 mM standard salbutamol solutions in 50 mM phosphate buffer. Scan rate was 100 mV s^{-1}.

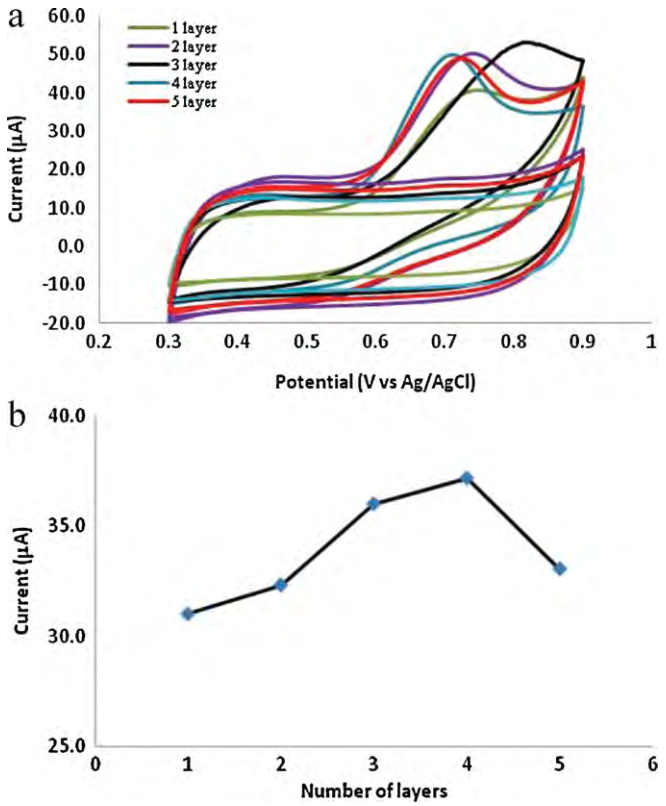

Fig. 7. (a) Cyclic voltammograms obtained at various numbers of printed GP-PEDOT:PSS layers on SPCE. (b) Relationship between current response and the number of GP-PEDOT:PSS layers. Scan rate was 100 mV s^{-1}. Solution is 0.5 mM standard salbutamol solution in 50 mM phosphate buffer (pH 7.0).

3.4. Effect of the number inkjet-printed layers

The electrochemical response of GP-PEDOT:PSS modified SPCE could be influenced by the number of inkjet-printed GP-PEDOT:PSS layers. CV responses toward a 0.5 mM salbutamol solution with different numbers of inkjet-printed GP-PEDOT:PSS layers are demonstrated in Fig. 7(a). It can be seen that the oxidation peak of salbutamol is considerably affected by the number of inkjet-printed layers. The oxidation peak amplitude is plotted as a function of the number of inkjet-printed layers as shown in Fig. 7(b). It is evident that the current amplitude initially increases as the number of layers increases from 1 to 4 and then decreases. Hence, the optimal number of printing layers is 4 and it is chosen for further characterization. A possible explanation for the observed result is that electrochemical response initially increases with the number of printing layers because the number of electroactive graphene and PEDOT:PSS sites increases. However, the surface of printed electrode becomes smoothen when the inkjet-printed layer is very thick because GP-PEDOT:PSS fills in pits of the rough SPCE surface. As a result, the electroactive surface area decreases and electrochemical response reduces.

3.5. Concentration dependence study

The CV measurements were made with different salbutamol concentrations as illustrated in Fig. 8(a). The current amplitude of oxidation peak as a function of concentration is plotted as shown in Fig. 8(b). It is clear that the oxidation peak current varies linearly with concentration in the range from 5.0 to 550 μM. The observed linear dynamic range of 500 μM is considerably wider than the range of 100 μM from previously reported salbutamol detection using vertically aligned CNT electrode [21]. The regression equation is given by $y = 0.0366x + 0.2414$ ($r^2 = 0.995$), where y and x are the height of peak current (μA) and salbutamol concentration (μM), respectively. The slope of the equation is corresponding to a linear sensitivity of 0.0366 μA/μM. The detection limit (3S/N) is estimated to be as low as 1.25 μM. The noise value (N) is determined from peak–peak amplitude of sinusoidal noise in the base line region of CV curve.

3.6. Stability study

The stability of GP-PEDOT:PSS modified SPCE was verified by recording successive CVs. After 5 cycles, no change was observed in CV profiles. The electrodes also remained stable in the presence of salbutamol up to 20 successive cycles or more with a relative standard deviation (RSD, $n = 20$) of 4.5%. Thus, GP-PEDOT:PSS modified SPCE exhibited very good stability. Furthermore, no significant change in the response was observed for more than two months after electrodes were stored at room temperature. Moreover, reproducibility of electrodes was determined from seven sensors fabricated in the same batch and RSD ($n = 20$) of 7.5% was obtained. Therefore, GP-PEDOT:PSS modified SPCE had satisfactory repeatability and reproducibility. It should be noted that repeatability and reproducibility were measured at 100 μM salbutamol concentration.

3.7. Performance for pharmaceutical applications

Salbutamol contents in pharmaceutical samples including Salbusian syrub and Salbolin tablet were analyzed by the developed

Table 1
Comparison of the labeled values of salbutamol in pharmaceutical products and the analyzed results by CV using GP-PEDOT:PSS electrode.

Samples	Salbutamol content		
	Labeled value	HPLC-UV measured value	Analyzed value
Salbusian syrub	400 mg/l	401 ± 3 mg/l	373.7 mg/l
Salbolin tablet	2 mg/tablet	2 ± 0.1 mg/tablet	1.86 mg/tablet

GP-PEDOT:PSS modified SPCE. The analyzed results were then compared to labeled values from their manufacturer and measured results from high performance liquid chromatography with ultraviolet detection (HPLC-UV) as shown in Table 1. HPLC-UV measurements were conducted by the manufacturer (IDS Manufacturing Ltd., Thailand). It is clear that our results are in fair agreement with those from HPLC-UV. The difference between the value measured by GP-PEDOT:PSS modified SPCE and HPLC-UV is around 7%, which is practically acceptable. The deviation should be due to small interference from matrices. Moreover, recovery studies yield good recovery values of 81.98–90.58%. This confirms that matrices in these samples have small influence on electrochemical oxidation of salbutamol by GP-PEDOT:PSS modified SPCE. Thus, the samples may directly be analyzed by our method with acceptably low matrices' interference. Nevertheless, the interference problems were found to be severe in urine samples and some other pharmaceutical products. In those cases, separation techniques would be needed before an electrochemical measurement.

The enhanced sensitivity, better detection limit and reduced interference for salbutamol detection of GP:PEDOT:PSS composite could be attributed to specific electrochemical activities between PEDOT:PSS/graphene and salbutamol. In the salbutamol oxiative reaction, salbutamol molecule is oxidized by electrochemical potential and become salbutamol free radical giving one electron and one proton [27]. PEDOT:PSS may act as a mediator [15,33] that promotes one electron–proton charge transfer in the oxidation process of salbutamol. Graphene can further enhance electron transfer rate via its very high electrical conductivity and huge adsorption surface area on edges of graphene basal plane. In addition, the salbutamol reactant can be better adsorbed and oxidized by graphene due to strong π–π interaction between salbutamol free radical and sp^2-bonded carbon atoms of graphene sheet [34,35].

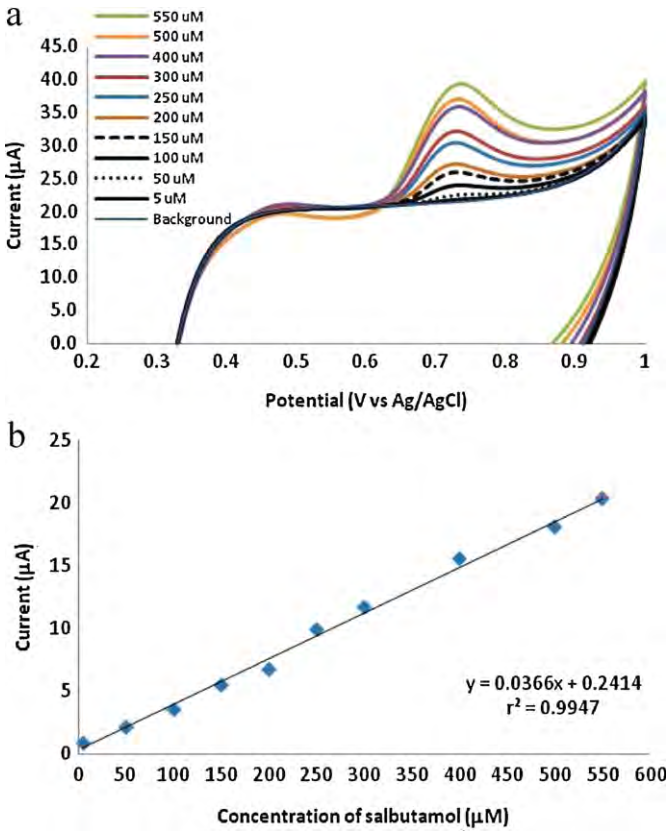

Fig. 8. Cyclic voltammograms obtained at various salbutamol concentrations in phosphate buffer (pH 7.0). The inset picture shows the relationship between salbutamol concentration and oxidation peak current response. Scan rate was 100 mV s^{-1}.

4. Conclusions

In conclusion, this report presents the first utilization of inkjet-printed GP-PEDOT:PSS modified SPCE electrode for electrochemical detection of salbutamol. GP-PEDOT:PSS ink is synthesized by one-step electrolytic exfoliation method and inkjet printed on SPCE. TEM characterization confirms the presence of graphene sheets of polygon shape with average diameter of 500 nm and SEM image indicates that SPCE surface is smoothen after successive GP-PEDOT:PSS printing. From CV measurement, the oxidation peak amplitudes of PEDOT:PSS modified and GP-PEDOT:PSS modified SPCEs are found to be approximately 30 and 150 times higher than that of unmodified SPCE, respectively. In addition, the method provides excellent analytical features with a wide dynamic range of 500 μM and a low detection limit (3S/N) of 1.25 μM. Moreover, direct analyses of salbutamol in pharmaceutical products have been demonstrated with low matrices' interference. Therefore, inkjet-printed GP-PEDOT:PSS on SPCE is highly promising for advanced electrochemical detection.

Acknowledgments

This work has been funded by Director Initiative Program, NECTEC. Adisorn Tuantranont would like to express his gratitude for Researcher Career Development Grant (RSA5380005) from Thailand Research Fund (TRF).

References

[1] X. Liang, Z. Fu, S.Y. Chou, Nano Lett. 7 (2007) 3840–3844.
[2] C. Stampfer, E. Schurtenberger, F. Molitor, J. Guttinger, T. Ihn, K. Ensslin, Tunable graphene single electron transistor, Nano Lett. 8 (2008) 2378–2383.
[3] D. Gunlycke, D.A. Areshkin, J.W. Li, J.W. Mintmire, C.T. White, Nano Lett. 7 (2007) 3608–3611.
[4] G. Zhu, T. Xu, T. Lv, L. Pan, Q. Zhao, Z. Sun, J. Electroanal. Chem. 650 (2011) 248–251.
[5] D.W. Wang, I.R. Gentle, G.Q. Lu, Electrochem. Commun. 12 (2010) 1423–1427.
[6] Y. Shao, J. Wang, H. Wu, J. Lin, I.A. Aksay, Y. Lin, Electroanalysis 22 (2010) 1027–1036.
[7] X. Kanga, J. Wanga, H. Wua, J. Liua, I.A. Aksayc, Y. Lina, Talanta 81 (2010) 754–759.
[8] C. Punckt, M.A. Pope, J. Liu, Y. Lin, Electroanalysis 22 (2010) 1–8.
[9] S. Alwarappan, A. Erdem, C. Liu, C.-Z. Li, J. Phys. Chem. C 113 (2009) 8853–8857.
[10] M. Pumera, A. Ambrosi, A. Bonanni, E.L.K. Chng, H.L. Poh, Trends Anal. Chem. 29 (2010) 954–965.
[11] G. Wang, B. Wang, J. Park, Y. Wang, B. Sun, J. Yao, Carbon 47 (2010) 3242–3246.
[12] K.S. Choi, F. Liu, J.S. Choi, T.S. Seo, Langmuir 26 (2010) 12902–12908.

[13] D.-W. Wang, F. Li, J. Zhao, W. Ren, Z.-G. Chen, J. Tan, Z.-S. Wu, I. Gentle, G.Q. Lu, H.M. Lu, Cheng, ACS Nano 3 (2009) 1745–1752.
[14] Y. Han, B. Ding, X. Zhang, J. New Mat. Electrochem. Systems. Received: July 25, 2010, accepted: October 20, 2010, Available online: November 15, 2010.
[15] Y. Yoshioka, G.E. Jabbour, Synth. Met. 156 (2006) 779–783.
[16] Y. Xu, Y. Wang, J. Liang, Y. Huang, Y. Ma, X. Wan, Y. Chen, Nano Res. 2 (2009) 343–348.
[17] W. Hong, Y. Xu, G. Lu, C. Li, G. Shi, Electrochem. Commun. 10 (2008) 1555–1558.
[18] K. Crowley, A. Morrin, R.L. Shepherd, M. in, het. Panhuis, G.G. Wallace, M.R. Smyth, A.J. Killard, IEEE Sens. 10 (2010) 1419–1426.
[19] K. Crowley, A. Morrin, A. Hernandez, E. O'Maley, P.G. Whitten, G.G. Wallace, M.R. Smyth, A.J. Killard, Talanta 77 (2008) 710–717.
[20] M.-H. Spyridaki, P. Kiousi, A. Vonaparti, P. Valavani, V. Zonaras, M. Zahariou, E. Sianos, G. Tsoupras, C. Georgakopoulos, Anal. Chim. Acta 573 (2006) 242–249.
[21] R.N. Goyal, M. Oyama, S.P. Singh, J. Electroanal. Chem. 611 (2007) 140–148.
[22] M.C. Dumasia, E. Houghton, J. Chromatogr. 564 (1991) 503–513.
[23] M.P. Montrade, B.L. Bizec, F. Monteau, B. Siliart, F. Andre, Anal. Chim. Acta 275 (1993) 253–268.
[24] W. Haasnoot, M.E. Ploum, R.J.A. Paulussen, R. Schilt, F.A. Huf, J. Chromatogr. 519 (1990) 323–335.
[25] L.A. Lin, R.S. Tomlinson, R.D. Stazger, J. Chromatogr. A 762 (1997) 275–280.
[26] S. Moane, J.R. Barreira Rodriguez, A.J. Miranda Ordieres, P. Tuñón Blanco, M.R. Smyth, J. Pharm. Biomed. Anal. 14 (1995) 57–63.
[27] C. Karuwan, T. Mantim, P. Chaisuwan, P. Wilairat, K. Grudpan, P. Jittangprasert, Y. Einaga, O. Chailapakul, L. Suntornsuk, O. Anurukvorakun, D. Nacapricha, Sensors 6 (2006) 1837–1850.
[28] C. Karuwan, A. Wisitsoraat, T. Maturos, D. Phokharatkul, A. Sappat, K. Jaruwongrungsee, T. Lomas, A. Tuantranont, Talanta 79 (2009) 995–1000.
[29] C. Karuwan, A. Wisitsoraat, A. Sappat, K. Jaruwongrungsee, V. Patthanasettakul, A. Tuantranont, Sens. Lett. 8 (2010) 1–6.
[30] L. Shen, Z. Li, P. He, Electrochem. Commun. 12 (2010) 876–881.
[31] Z. Ni, Y. Wang, T. Yu, Z. Shen, Nano Res. 1 (2008) 273–291.
[32] A.C. Ferrari, J. Robertson, Phys. Rev. B 61 (2000) 95–107.
[33] G. Istamboulie, T. Sikora, E. Jubete, E. Oschoteco, J.-L. Marty, T. Noguer, Talanta 82 (2010) 957–961.
[34] J.I. Paredes, S. Villar-Rodil, A. Martinez-Alonso, J.M.D. Tascon, Langmuir 24 (2008) 10560.
[35] A. Rochefort, J.D. Wuest, Langmuir 25 (2009) 210.

Biographies

Chanpen Karuwan received her master degree from Mahidol University Institute of Applied Analytical and Inorganic Chemistry in 2006. In that year, she worked in National Electronics and Computer Technology Center as a research assistant. Her research interests encompass the electrochemical chemistry and nanomaterial-based sensors.

Chakrit Sriprachuabwong is an assistant researcher at the Nanoelectronics and MEMS Laboratory, National Electronics and Computer Technology Center (NECTEC), Thailand, where he has been a laboratory member since 2009. He holds a bachelor's degree in chemistry with honors in 2005 and completed graduate studies in materials science in 2007. His research interests include the printed electronics and conductive materials.

Anurat Wisitsoraat received his PhD, MS degrees from Vanderbilt University, TN, USA, and BEng degree in electrical engineering from Chulalongkorn University, Bangkok, Thailand in 2002, 1997, and 1993, respectively. His research interests include microelectronic fabrication, semiconductor devices, electronic and optical thin film coating, sensors, and micro electromechanical systems (MEMS).

Ditsayut Phokharatkul is an assistant researcher at MEMS Laboratory in NECTEC, Thailand. He received his BE and ME degrees from Nagoya University (Japan) in 2006 and 2008, respectively. His dissertation is development of high density horizontally aligned carbon nanotubes for CNT-FET application. His research interests include microelectronic fabrication, semiconductor devices, carbon nanotubes, graphene and sensors.

Pornpimol Sritongkham received her PhD in electroanalytical chemistry from Cranfield University (United Kingdom) in 2002. Her current research is focused on the surface modification of QCM- and electrochemical biosensors and on the development of novel diagnostic devices.

Adisorn Tuantranont received the BS degree in electrical engineering from King Mongkut's Institute of Technology Ladkrabang, Thailand, in 1995, and the MS and PhD degrees in electrical engineering from the University of Colorado at Boulder in 2001. Since 2001, he has been the director of the Nanoelectronics and MEMS Laboratory, National Electronic and Computer Technology Center (NECTEC), Pathumthani, Thailand. His research interests are in the area of micro electro-mechanical systems (MEMS), nanoelectronics, lab-on-a-chip technology and printed electronics. He has authored more than 50 refereed journals, 150 proceedings, and holds five patents. He also received the Young Technologist Award in 2004 from the Foundation for the Promotion of Science and Technology under the patronage of H.M. the King, Thailand.

Journal of Materials Chemistry

Dynamic Article Links

Cite this: *J. Mater. Chem.*, 2012, **22**, 17094

www.rsc.org/materials

PAPER

Facile preparation of graphene–metal phthalocyanine hybrid material by electrolytic exfoliation

Johannes Philipp Mensing,[ab] Teerakiat Kerdcharoen,*[b] Chakrit Sriprachuabwong,[a] Anurat Wisitsoraat,[a] Ditsayut Phokharatkul,[a] Tanom Lomas[a] and Adisorn Tuantranont*[a]

Received 25th April 2012, Accepted 29th June 2012
DOI: 10.1039/c2jm32588h

In this article, we present a new, facile and efficient electrochemical method for the production of a stable aqueous dispersion of a graphene–metal phthalocyanine hybrid material. The material has been prepared by electrolytic exfoliation of graphite in an electrolyte containing copper phthalocyanine-3,4′,4″,4‴-tetrasulfonic acid tetrasodium salt (TSCuPc). Single- and few-layer graphene sheets, decorated with metal phthalocyanine molecules, are generated during the electrolysis and stably dispersed in the electrolyte with no further chemical treatment. Scanning electron/atomic force microscopic characterization shows that the TSCuPc–graphene hybrid structure has a sharp-edged particle morphology with thicknesses ranging from 2 nm to 6 nm, corresponding to 1 to 6 graphene-stacked layers and largely varied lateral dimensions from a few tens to several hundreds of nanometers. In addition, Raman/FTIR/UV-Vis spectra and X-ray diffraction reveal characteristic peaks that suggest that the TSCuPc–graphene hybrid is formed by non-covalent π–π interactions between graphene sheets and metal phthalocyanine and indicate a high quality graphene hybrid structure that can potentially be used in practical applications.

Introduction

Over the last few years, the search for novel nano-scale materials with special physical and chemical properties has been an important challenge in the field of nanotechnology. A promising approach is to synergistically combine two or more nano-materials into a new nanohybrid structure.[1–6] Carbon, in the form of graphene, is a highly intriguing material for scientists in various fields and is an outstandingly attractive building block for advanced hybrid materials. Graphene consists of tightly packed two-dimensional ('one-atom-thick') sheets of sp^2-hybridized carbon atoms arranged in a honeycomb crystal lattice.[7,8] Graphene sheets (sometimes referred to as graphene nano-sheets, GNSs) are considered to be the two-dimensional basis of other allotropes of carbon, and may be rolled or wrapped to form one-dimensional carbon nano-tubes or zero-dimensional fullerenes. Graphene possesses many extraordinary properties, such as high mobility of charge carriers, high mechanical strength, extremely high thermal conductivity as well as interesting optical characteristics.[9–11] Moreover, its two-dimensional geometry, unusual band structure and carrier mobility render it an ideal material for a large number of applications in nano-electronics, sensors, nano-composites, batteries, supercapacitors, hydrogen storage, field-effect transistors, resonators, transparent electrodes and organic photovoltaic devices.[12–19] Ever since Geim and co-workers prepared the first single layer graphene sheets in 2004 by micromechanical cleavage, a number of fabrication techniques such as epitaxial growth *via* ultra-high vacuum graphitization, solution-based reduction of graphene oxide, chemical vapor deposition and so on have been devised to massively produce various forms of graphene for potential applications.[20–24] One major obstacle to the use of graphene in technical applications is its poor processability due to strong attractive forces between the sheets. Thus, it has a strong tendency to agglomerate. In addition, GNSs are very poorly soluble in water and most other conventional solvents. It is, therefore, essential to develop methods of surface modification for graphene to allow molecular dispersion of individual graphene sheets (or at least few layer graphene) while retaining its desirable intrinsic properties.

In order to do so, various methods have been developed for chemical modification. For instance, functionalization of GNSs with oxygen-containing groups ('graphene oxide') can significantly improve their processability. However, it leads to inferior physical and electronic properties due to lattice damage. In contrast, other simple and versatile non-covalent methods through supramolecular interactions such as π–π stacking, electrostatic interaction and hydrogen bonding provide excellent

[a]*Nanoelectronics and MEMS Laboratory, National Electronics and Computer Technology Center (NECTEC), 112 Paholyothin Rd., Klong 1, Klong Luang, Pathumthani, 12120, Thailand. E-mail: adisorn.tuantranont@nectec.or.th; Fax: +66-2-564-6756; Tel: +66-2-564-6900*
[b]*Faculty of Science, Mahidol University, 272 Rama VI Road, Ratchathewi, Bangkok 10400, Thailand. E-mail: sctkc@mahidol.ac.th*

molecular dispersion while preserving the unique electronic properties of graphene because of no physical damage.[25] Non-covalent π–π stacking is feasible for GNS due to a large, accessible π-electron surface formed by the p_z-orbitals perpendicular to the sp^2-bonded carbon basal plane. This functionalization method will provide graphene with desired properties when it is combined with planar aromatic molecules such as metal phthalocyanines (MePcs).

MePcs are two-dimensional, 18 π-electron-possessing aromatic macrocycles with a metal atom located at the central cavity. They possess a variety of remarkable properties including (a) exceptional thermal and chemical stability such that temperature up to several hundred degree Celsius and strong acids or bases cannot damage the molecule, (b) astounding optical properties due to a large conjugated electron network leading to intense absorption bands in the visible region at 400 nm and 700 nm with extinction coefficients as high as 2×10^5 l mol^{-1} cm^{-1} in solution and (c) versatile chemical systems resulting in a large number of possible complexes with diverging chemical and physical characteristics.[26,27] Extensive research has been done on the fabrication of hybrid-materials combining carbon nanotubes (CNTs) and MePcs[27–32] with applications in optoelectronic, electro-catalytic or sensing devices. It has been shown that optoelectronic properties and electro-catalytic and sensing capabilities could be enhanced with the inclusion of CNTs in MePcs. It is, therefore, of great interest to explore to what extent these findings are transferable to graphene–MePc hybrid-materials.

Aqueous π–π bonded graphene–MePc hybrid-materials have previously been reported by various groups (*e.g.* Chunder *et al.*[33] or Zhang *et al.*[34]). In these reports, single layer graphene-oxide sheets dispersed in MePc are prepared by chemical oxidation of graphite in MePc solution and graphene-oxide is then reduced by chemical reduction using hydrazine. This method produces a highly defective graphene structure with inferior electronic properties. In addition, it is labor intensive since it includes oxidation–reduction steps and involves the usage of hydrazine, a highly toxic and environmentally harmful chemical.

Herewith, we present a new and facile method for the fabrication of graphene–MePc hybrid material by electrolytic exfoliation. This method can produce dispersions of high quality graphene sheets in one step which makes this method less labor intensive and supersedes the usage of toxic reagents. The physical, chemical and optical properties are characterized by scanning electron/atomic force microscopy, X-ray diffraction, and Raman/FTIR/UV-Vis spectroscopy.

Materials and methods

The graphene–MePc hybrid material was fabricated by electrolytic exfoliation of graphite rods (Electron Microscopy Sciences, Hatfield, PA; technical grade, with impurity levels of around 50 ppm) in an electrolyte containing copper phthalocyanine-3,4′,4″,4‴-tetrasulfonic acid tetrasodium salt (TSCuPc). The experimental setup for electrolytic exfoliation and the structure of TSCuPc are schematically shown in Fig. 1. In order to prepare the electrolyte, 10 mg ml^{-1} of TSCuPc were added to de-ionized water and ultrasonicated subsequently for 1 h to ensure complete dissolution. Pure graphite rods serve as both anode and cathode.

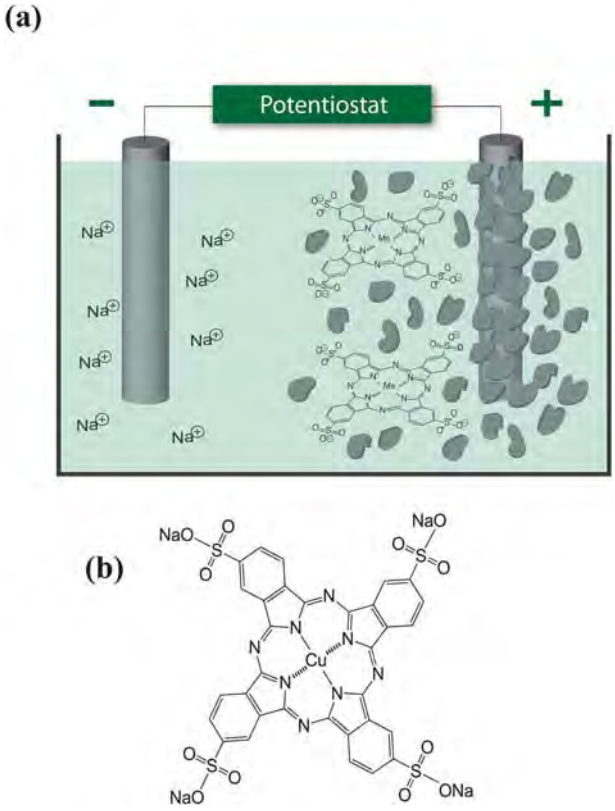

Fig. 1 (a) Schematic of the apparatus used for electrolytic exfoliation. TSCuPc dissociates into ions. The anions are forced against the graphite anode and exfoliate it. (b) The structure of Cu phthalocyanine-3,4′,4″,4‴-tetrasulfonic acid tetrasodium salt.

A constant potential of 12 V is applied between the two graphite rods and the process is terminated after 12 hours of electrolysis. A black precipitate as well as a slight color-change of the electrolyte from blue to blue-green is observed. In the electrolysis process, phthalocyanine tetrasulfonate anions are forced against the graphite anode by the electrical potential where they electrochemically interact with the graphite surface, resulting in exfoliation of graphene sheets into the electrolyte.[35] The solution is then ultrasonicated for 1 h to further exfoliate larger graphite particles in the precipitate into few-layer graphene sheets. During the course of the sonication, the color of the solution is further changed into almost purely green. After this step, the solution is centrifuged for 30 minutes at 3000 rpm and the resulting sediment is discarded. The obtained supernatant portion of the graphene–TSCuPc solution is then centrifuged again for five minutes at 10 000 rpm and the supernatant sediment is extracted. The sediment was redissolved with DI water, resulting in a green-grey solution with a hybrid-material content of 1 to 1.5 mg ml^{-1}. The dispersion proved to be naturally stable with no observable precipitation after several months.

Results and discussion

For morphological characterization using SEM (Hitachi S4700), samples of the electrolyte solution taken before and during the course of the preparation of the hybrid material are dropped onto silicon wafers and dried in a vacuum. SEM images of the

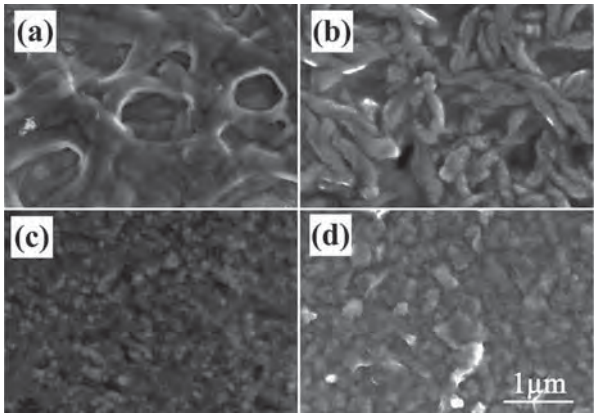

Fig. 2 SEM images of (a) a droplet of TSCuPc aqueous solution; (b) a droplet of the electrolyte after 12 h of electrolysis and 1 h of ultrasonication; (c) a droplet of the electrolyte after the first centrifugation step (30 min at 3k rpm); and (d) a droplet of the electrolyte after the final centrifugation step (5 min at 10k rpm).

specimens at the various stages of synthesis are shown in Fig. 2. Fig. 2a depicts the surface of a dried TSCuPc droplet with no graphene. It shows the typical intricate structure of this complex material, which was self-organized during the drying process. An SEM image of a droplet of the electrolyte after 12 h of electrolysis and 1 h of ultrasonication is illustrated in Fig. 2b. The structure is now predominantly characterized by elongated particles. Fig. 2c shows the surface of a droplet of the supernatant portion after the first centrifugation step. It can be seen that elongated particles are absent and the surface consists of TSCuPc–graphene hybrid-material particles and unbound TSCuPc aggregates appeared in the form of very fine nanoparticles. After the final centrifugation step to remove unbound TSCuPc, the structure appears as shown in Fig. 2d. Sharp edged particles, which are expected to be graphene sheets, become clearly observable, signifying the desired TSCuPc–graphene hybrid structure.

In order to investigate the morphology of TSCuPc–graphene hybrid particles in more detail using AFM (JPK nanowizard 3), a dilute dispersion of the hybrid material was spin-coated on freshly cleaved ultra-smooth mica substrates. Fig. 3 shows the resulting AFM image of TSCuPc–graphene hybrid particles and a line profile across the particles. It can be seen that the thicknesses of the particles are ranging from approximately 2 nm to 6 nm, which may correspond to those of TSCuPc–graphene hybrid particles consisting of 1 to ~6 graphene-stacked layers.[22,33] The lateral dimensions of the observed particles are largely varied from a few tens to several hundreds of nanometers.

UV-Vis absorbance spectra are measured using a fiber-optic spectrometer (Ocean Optics USB4000) to characterize the optical properties and identify the chemical structure of the hybrid materials. Absorbance spectra (400–900 nm) of the TSCuPc aqueous solution, the electrolyte after 12 h of electrolytic exfoliation followed by 1 h sonication, the supernatant portion after the first centrifugation step (3000 rpm for 30 min) and the re-dissolved hybrid-material solution after the second centrifugation step (10 000 rpm for five minutes) are demonstrated in Fig. 4A and absorption peak denominations are given in Table 1.

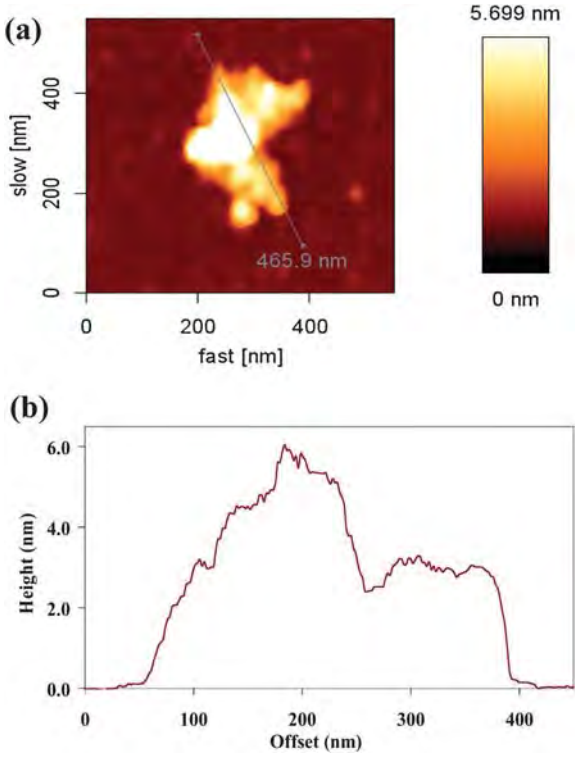

Fig. 3 AFM image and height profile of a hybrid particle.

The spectrum of the TSCuPc solution (Fig. 4A-*a*) exhibits the typical Q band of phthalocyanines in the wavelength region between ~550 and ~700 nm. The HOMO–LUMO ($\pi \rightarrow \pi^*$) transition in the TSCuPc electronic structure is responsible for the Q band formation. It can be observed that the Q band of TSCuPc in water consists of two bands, one with a prominent peak at 629 nm and the other with a satellite shoulder at 663 nm, which correspond to the presence of a dimer and a monomer of TSCuPc, respectively.[35] Furthermore, a deep valley between approximately 400 and 550 nm can be observed.

The UV-Vis spectrum changes during the exfoliation process and also after sonication due to exfoliation of graphite particles and subsequent formation of the hybrid material. Fig. 4A-*b* shows absorbance of the electrolyte after electrolysis followed by one hour of sonication. It can be seen that the dimer peak is blue-shifted to 609 nm, whereas the position of the monomer peak is red-shifted to approximately 770 nm. This suggests some interaction between the TSCuPc dimer and the exfoliated graphene in this stage. After the first centrifugation step and the removal of the sediment, the spectrum (Fig. 4A-*c*) contains the dimer peak at 631 nm and the monomer peak at 674 nm. Furthermore, a third peak appears at about 697 nm. Apparently, the spectrum of the re-dissolved TSCuPc–graphene hybrid material (Fig. 4A-*d*) exhibits only a single peak at 707 nm which is in the region of the third peak of the previous spectrum. The third peak at ~700 nm can be attributed to the TSCuPc–graphene hybrid formed by π–π interactions between graphene sheets and TSCuPc. When hybrid structures are fully formed, dimer and monomer peaks of TSCuPc largely disappear possibly due to reduced aggregation as a result of strong π–π interactions between graphene sheets and TSCuPc.

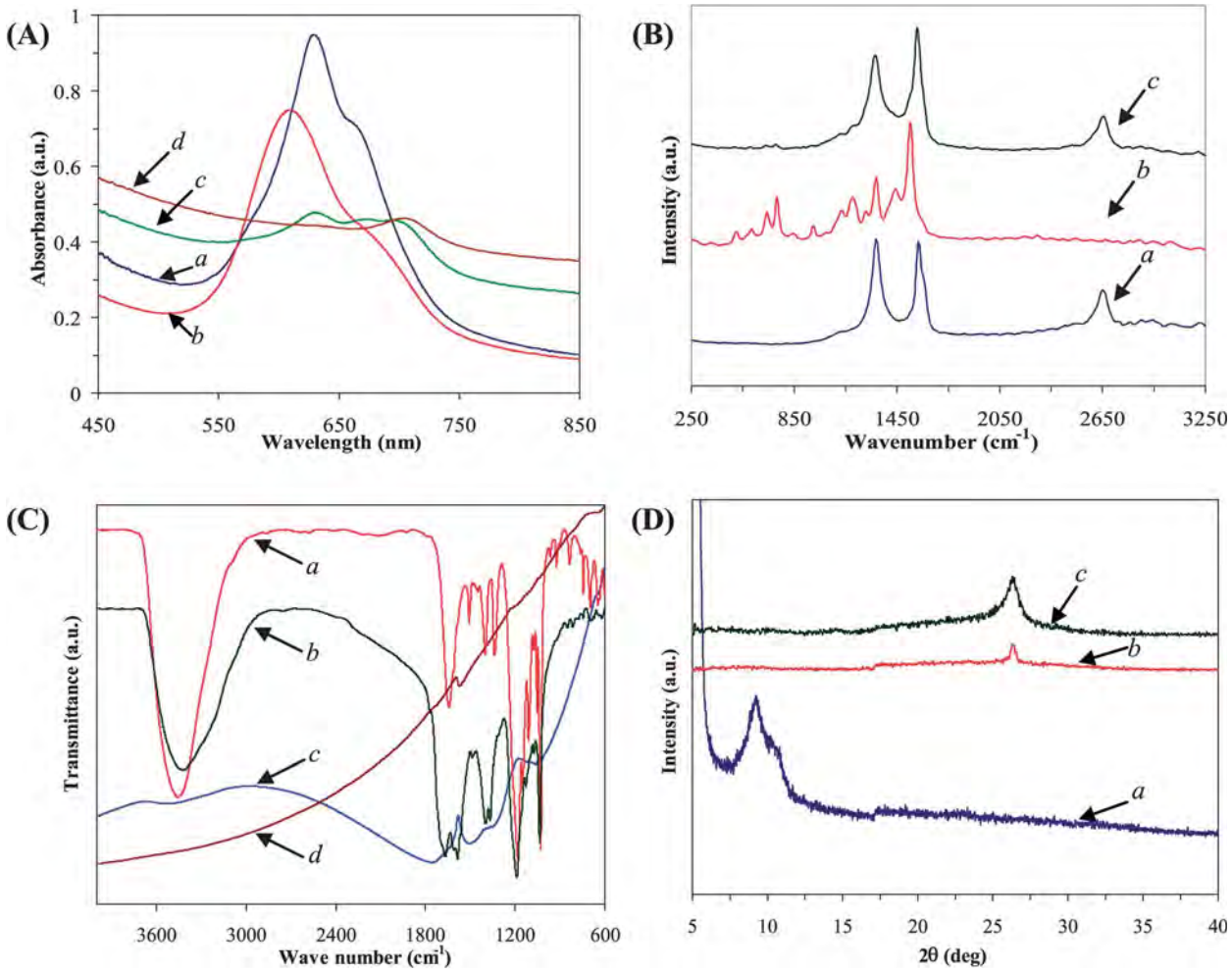

Fig. 4 (A) UV-Vis spectra of (*a*) the aqueous TSCuPc solution; (*b*) the electrolyte after 12 h of electrolysis and 1 h of sonication; (*c*) the supernatant after the first centrifugation step (30 min at 3k rpm); and (*d*) the redispersed sediment after the final centrifugation step (5 min at 10k rpm). (B) Raman spectra of (*a*) electrolytically exfoliated graphene powder; (*b*) TSCuPc; and (*c*) TSCuPc–graphene hybrid material. (C) FTIR spectra of (*a*) TSCuPc; (*b*) supernatant after 1 h of sonication and centrifugation (30 min at 3k rpm); (*c*) TSCuPc–graphene hybrid material; and (*d*) electrolytically exfoliated graphene powder. (D) XRD patterns of films of (*a*) TSCuPc; (*b*) graphene powder; and (*c*) TSCuPc–graphene hybrid material.

Fig. 4B shows Raman spectra of graphene, TSCuPc and the TSCuPc–graphene hybrid material measured using a confocal Raman spectrometer (NT-MDT NTEGRA) with an excitation wavelength of 633 nm. For comparison, a Raman spectrum is also taken from electrolytically exfoliated graphene prepared based on the methods proposed by Wang *et al.*[36] and Liu *et al.*[37] The spectrum of electrolytically exfoliated graphene (Fig. 4B-*a*) shows a D band at ~1328 cm^{-1}, a G band at ~1574 cm^{-1}, and a 2D band at ~2649 cm^{-1}, which are known to be attributed to zone boundary phonons, doubly degenerate zone centers (E_{2g} mode) and the second order scattering of zone boundary phonons, respectively.[38] The ratio between the intensities of the D and G bands, I_D/I_G, is a measure of the defect density in graphene (deviations from the ideal sp^2 hybridized graphene structure). It can be seen from Fig. 4B-*c* that the D/G ratio of the TSCuPc–graphene hybrid material (0.92) is about 10% lower than that of electrolytically exfoliated graphene (1.02), suggesting a larger average sp^2 domain size and lower defect density of

Table 1 UV-Vis peak denominations

	Chemical structure		
Material	Dimer	Monomer	Hybrid
TSCuPc (aqueous)	629 nm	663 nm	—
After electrolysis + 1 h ultrasonication	609 nm	Approx. 670 nm (shoulder)	—
Supernatant after the 1st centrifugation step	631 nm	674 nm	697 nm
Sediment after the 2nd centrifugation step	—	—	707 nm

graphene in the hybrid structure. Additionally, the positions of the D and G bands are shifted to lower wavenumbers, namely, 1319 cm^{-1} and 1566 cm^{-1}, respectively. These shifts are due to the electron donating nature of π–π bonded TSCuPc molecules.[39] Furthermore, characteristic vibrational features of TSCuPc, shown in Fig. 4B-*b*, are also observable in the Raman spectrum of the TSCuPc–graphene hybrid material. The highest intensity features of TSCuPc can be found at 1528 cm^{-1}, 1326 cm^{-1} and 744 cm^{-1}. They also appear in the hybrid-material spectrum but the positions are shifted to 1513 cm^{-1} and 738 cm^{-1}, respectively, while the feature located at 1326 cm^{-1} leads to a slightly broadened D band of graphene in the hybrid-material spectrum. These findings support the assumption that the π–π bonded TSCuPc–graphene hybrid-material is formed.

The chemical bonding information was further characterized by Fourier transform infrared spectra (FTIR) (Perkin-Elmer Spectrum Spotlight 300). Fig. 4C-*a* shows the spectrum of TSCuPc which exhibits a large band between ~2975 and ~3750 cm^{-1} with a peak at 3458 cm^{-1} corresponding to OH stretching of absorbed water and the typical bending vibration bands of this compound in the fingerprint region between ~500 and ~1800 cm^{-1} with the most intense peaks at 1643, 1183 and 1028 cm^{-1}. After sonication and centrifugation for 30 min at 3k rpm, the spectrum is altered significantly as can be seen in Fig. 4C-*b*. The OH peak is red-shifted to 3423 cm^{-1} and becomes less intense. This is probably due to the adsorption of hydrophobic graphene sheets instead of water molecules. Furthermore, the intense peaks in the fingerprint region are blue-shifted to 1666, 1190 and 1035 cm^{-1}, respectively. Moreover, features which are only barely noticeable in the TSCuPc spectrum (*e.g.* shoulders at 1612 and 1585 cm^{-1}) appear with increased intensities in spectrum b. Fig. 4C-*c* shows the spectrum of the redispersed sediment after the final centrifugation step illustrating that the spectrum undergoes another significant change. The intensity of the OH peak further decreases and the peak is red-shifted to 3532 cm^{-1}. Features which were clearly discernible peaks in spectrum b become broad bands with blue-shifted positions at 1753 cm^{-1} (peaks between 1666 and 1585 cm^{-1} in b), 1507 cm^{-1} (peaks between 1399 and 1368 cm^{-1} in b) and 1060 cm^{-1} (peak at 1035 cm^{-1} in b). The spectrum of electrolytically exfoliated graphene reveals a small peak at 1574 cm^{-1}, which can be attributed to C=C stretching of graphene sheets. This feature cannot clearly be identified in the other spectra but even so the spectra alteration in the course of the hybrid-material preparation (from spectra a to c) strongly suggests molecular interactions and formation of π–π bonded material.

The information about the crystal structure of the prepared material is obtained from X-ray diffraction (Rigaku TTRAX III diffractometer) operated in thin film measurement mode. XRD samples are prepared by dropping 150 μl of aqueous dispersions of the materials to be investigated on glass slides followed by drying in a vacuum. XRD results are shown in Fig. 4D. The diffraction pattern of the pure TSCuPc film (Fig. 4D-*a*) contains peaks at $2\theta = 5.2°$, 9.2° and 10.2° which correspond to lattice spacings of 16.8 Å, 9.6 Å and 8.5 Å, respectively. Fig. 4D(*b* and c) depict XRD patterns of pure graphene and TSCuPc–graphene hybrid-material films, respectively. The typical (002) peaks of graphitic materials are present at 26.3° equivalent to a lattice spacing of 3.38 Å. It can clearly be observed that the peaks present in the XRD pattern of TSCuPc cannot be found in b and c. The absence of diffraction peaks may suggest the occurrence of monomeric TSCuPc attached to graphene/graphite crystals since Raman and FTIR spectra both indicate the formation of the TSCuPc–graphene hybrid material.

Conclusion

In conclusion, a novel and facile preparation method for the metal phthalocyanine–graphene hybrid material has successfully been developed. The physical and chemical properties of the hybrid material have been characterized by SEM, AFM, XRD, UV/Vis-, Raman- and FTIR spectroscopy. The morphological characterization shows that the TSCuPc–graphene hybrid structure has a sharp-edged particle morphology with thicknesses ranging from 2 nm to 6 nm, corresponding to 1 to ~6 graphene-stacked layers and largely varied lateral dimensions from a few tens to several hundreds of nanometers. In addition, Raman/FTIR/UV-Vis spectra and X-ray diffraction suggest that the TSCuPc–graphene hybrid is formed by non-covalent π–π interactions between graphene sheets and metal phthalocyanine and a high quality graphene hybrid structure has been achieved. Further work is in progress to evaluate the applicability of the hybrid material in the field of gas sensing, especially for the identification and quantification of volatile organic compounds by means of optical as well as electrical transduction.

Acknowledgements

This work was carried out as part of the requirements for the degree of Doctor of Philosophy of Mr Johannes Mensing in the materials science and engineering program at Mahidol University, Bangkok, Thailand. This work has been funded by Platform Technology Program, grant no. P1201107, NECTEC. Adisorn Tuantranont would like to express his gratitude for Researcher Career Development grant no. RSA5380005, Thailand Research Fund (TRF).

Notes and references

1 A. V. Parra, M. Rei Vilar, N. Battaglini, A. M. Ferraria, A. M. Botelho do Rego, S. Boufi, M. L. Rodríguez-Méndez, E. Fonavs, I. Muzikante and M. Bouvet, *Langmuir*, 2007, **23**, 3712–3722.
2 P. Gomez-Romero, *Adv. Mater.*, 2001, **13**, 163–174.
3 P. Gomez-Romero and C. Sanchez, *New J. Chem.*, 2005, **29**, 57–58.
4 B. G. Choi, J. Im, H. S. Kim and H. S. Park, *Electrochim. Acta*, 2011, **56**, 9721–9726.
5 D. Zha, S. Mei, Z. Wang, H. Li, Z. Shi and Z. Jin, *Carbon*, 2011, **49**, 5166–5172.
6 Y. Xue, H. Zhao, Z. Wu, X. Li, Y. He and Z. Yuan, *Biosens. Bioelectron.*, 2011, **29**, 102–108.
7 V. Singh, D. Joung, L. Zhai, S. Das, S. I. Khondaker and S. Seal, *Prog. Mater. Sci.*, 2011, **56**, 1178–1271.
8 X. Huang, Z. Yin, S. Wu, X. Qi, Q. He, Q. Zhang, Q. Yan, F. Boey and H. Zhang, *Small*, 2011, **7**, 1876–1902.
9 D. R. Dreyer, R. S. Ruoff and C. W. Bielawski, *Angew. Chem., Int. Ed.*, 2010, **49**, 9336–9344.
10 H.-P. Boehm, *Angew. Chem., Int. Ed.*, 2010, **49**, 9332–9335.
11 C. N. R. Rao, A. K. Sood, K. S. Subrahmanyam and A. Govindaraj, *Angew. Chem., Int. Ed.*, 2009, **48**, 7752–7777.
12 M. Liang and L. Zhi, *J. Mater. Chem.*, 2009, **19**, 5871–5878.
13 X. Huang, X. Zhou, K. Qian, D. Zhao, Z. Liu and C. Yu, *J. Alloys Compd.*, 2011, **514**, 76–80.
14 W. Yuan, B. Li and L. Li, *Appl. Surf. Sci.*, 2011, **257**, 10183–10187.

15 S. Mao, K. Yu, G. Lu and J. Chen, *Nano Res.*, 2011, **4**, 921–930.
16 A. M. Zande, R. A. Barton, J. S. Alden, C. S. Ruiz-Vargas, W. S. Whitney, P. H. Q. Pham, J. Park, J. M. Parpia, H. G. Craighead and P. L. McEuen, *Nano Lett.*, 2010, **10**, 4869–4873.
17 Y. Y. Choi, S. J. Kang, H. K. Kim, W. M. Choi and S. I. Na, *Sol. Energy Mater. Sol. Cells*, 2011, **96**, 281–285.
18 Y. Xu, Z. Liu, X. Zhang, Y. Wang, J. Tian, Y. Huang, Y. Ma, X. Zhang and Y. Chen, *Adv. Mater.*, 2009, **21**, 1275–1279.
19 X. Sun, D. Luo, J. Liu and D. G. Evans, *ACS Nano*, 2010, **4**, 3381–3389.
20 K. S. Novoselov, A. K. Geim, S. V. Morozov, D. Jiang, Y. Zhang, S. V. Dubonos, I. V. Grigorieva and A. A. Firsov, *Science*, 2004, **306**, 666–669.
21 C. Berger, Z. Song, X. Li, X. Wu, N. Brown, C. Naud, D. Mayou, T. Li, J. Hass and A. N. Marchenkov, *et al.*, *Science*, 2006, **312**, 1191–1196.
22 A. Chunder, T. Pal, S. I. Khondaker and L. Zhai, *J. Phys. Chem. C*, 2010, **114**, 15129–15135.
23 K. S. Kim, Y. Zhao, H. Jang, S. Y. Lee, J. M. Kim, K. S. Kim, J.-H. Ahn, P. Kim, J.-Y. Choi and B. H. Hong, *Nature*, 2009, **457**, 706–710.
24 A. Dato, V. Radmilovic, Z. Lee, J. Phillips and M. Frenklach, *Nano Lett.*, 2008, **8**, 2012–2016.
25 X. Zhang, Y. Feng, S. Tang and W. Feng, *Carbon*, 2010, **48**, 211–216.
26 G. Guillaud, J. Simon and J. P. Germain, *Coord. Chem. Rev.*, 1998, **178**, 1433–1484.
27 Y. Wang, N. Hu, Z. Zhou, D. Xu, Z. Wang, Z. Yang, H. Wei, E. S.-W. Kong and Y. Zhang, *J. Mater. Chem.*, 2011, **21**, 3779–3787.
28 Z. Xu, H. Li, K.-Z. Li, Y. Kuang, Y. Wang, Q. Fu, Z. Cao and W. Li, *Cryst. Growth Des.*, 2009, **9**, 4136–4141.
29 U. Hahn, S. Engmann, C. Oelsner, C. Ehli, D. M. Guldi and T. Torres, *J. Am. Chem. Soc.*, 2010, **132**, 6392–6401.
30 L. Lozzi, S. Santucci, F. Bussolotti and S. La Rosa, *J. Appl. Phys.*, 2008, **104**, 033701.
31 T. Mugadza and T. Nyokong, *Electrochim. Acta*, 2010, **55**, 6049–6057.
32 F. C. Moraes, D. L. Golinelli, L. H. Mascaro and S. A. Machado, *Sens. Actuators, B*, 2010, **148**, 492–497.
33 A. Chunder, J. Liu and L. Zhai, *Macromol. Rapid Commun.*, 2010, **31**, 380–384.
34 X.-F. Zhang and Q. Xi, *Carbon*, 2011, **49**, 3842–3850.
35 B. Brozek-Pluska, I. Szymczyk and H. Abramczyk, *J. Mol. Struct.*, 2005, **744**, 481–485.
36 G. Wang, B. Wang, J. Park, Y. Wang, B. Sun and J. Yao, *Carbon*, 2009, **47**, 3242–3246.
37 N. Liu, F. Luo, H. Wu, Y. Liu, C. Zhang and J. Chen, *Adv. Funct. Mater.*, 2008, **18**, 1518–1525.
38 A. C. Ferrari, J. C. Meyer, V. Scardaci, C. Casiraghi, M. Lazzeri, F. Mauri, S. Piscanec, D. Jiang, K. S. Novoselov, S. Roth and A. K. Geim, *Phys. Rev. Lett.*, 2006, **97**, 187401.
39 Q. Su, S. Pang, V. Alijani, C. Li, X. Feng and K. Müllen, *Adv. Mater.*, 2009, **21**, 3191–3195.

Journal of Electroanalytical Chemistry 704 (2013) 208–213

Contents lists available at SciVerse ScienceDirect

Journal of Electroanalytical Chemistry

journal homepage: www.elsevier.com/locate/jelechem

Graphene–PEDOT:PSS on screen printed carbon electrode for enzymatic biosensing

A. Wisitsoraat [a,*], S. Pakapongpan [a], C. Sriprachuabwong [a], D. Phokharatkul [a], P. Sritongkham [b], T. Lomas [a], A. Tuantranont [a,*]

[a] National Electronics and Computer Technology Center, NSTDA, Thailand
[b] Biomedical Engineering, Mahidol University, Thailand

ARTICLE INFO

Article history:
Received 17 December 2012
Received in revised form 11 May 2013
Accepted 8 July 2013
Available online 19 July 2013

Keywords:
Graphene–PEDOT:PSS
Screen printed carbon electrode
Enzymatic biosensor

ABSTRACT

In this work, a highly sensitive enzyme-based biosensor is developed based on graphene–poly(3,4-ethylenedioxythiophene):polystyrene sulfonic acid (GP-PEDOT:PSS) modified screen printed carbon electrode (SPCE) for electrochemical detection of glucose. GP-PEDOT:PSS nanocomposite synthesized by one-step electrolytic exfoliation is drop-coated on SPCE and glucose oxidase (GOD) enzyme is then immobilized on GP-PEDOT:PSS by glutaraldehyde cross linking. Electron microscope characterization confirms the presence of multi-layer graphene sheets and the appearance of smooth and long microstripe structure of GOD on the electrode surface. Direct electrochemistry of GOD at the GP/PEDOT:PSS electrode is observed by cyclic voltammetry and graphene plays the main role in a quasi-reversible redox process. GOD/GP-PEDOT:PSS electrode exhibits a high amperometric sensitivity of 7.23 μA/mM, which is about 13 times higher than that of GOD/PEDOT:PSS but has a relatively narrow linear dynamic range of ~20–900 μM. Moreover, GOD/GP-PEDOT:PSS offers a very low detection limits (3S/N) of ~0.3 μM which is better or comparable to other recent reports of highly sensitive glucose biosensors. Furthermore, the sensor has good stability with only 30% loss of enzyme activity after 30 days.

1. Introduction

Graphene, the latest two-dimensional nanocarbon material, is highly promising for electrochemical biosensing due to its large two-dimensional electrical conductivity, excellent electron transfer rate, huge specific surface area and efficient direct electrochemistry [1–6]. In addition, it has been shown to exhibit superior sensing performances over other carbon based materials including its nearest counterpart, carbon nanotubes (CNTs), owing to its twice larger surface area, higher number of chemically active edge planes per unit mass, higher electron mobility and the absence of anomalous sensing response from metallic impurities [5,7,8]. Moreover, it is more feasible for commercial applications because its production based on low-cost graphite can be done with no hazardous byproducts [1,9,10]. Among various reported graphene synthesis methods [11–13], electrolytic exfoliation is particularly attractive for electrochemical biosensing because it can produce stable graphene dispersion in conducting polymer matrix, which could be highly effective for electrochemical transduction and bio-receptor immobilization. In addition, the process is simple, low cost and suitable for large-scale production [14].

Poly(3,4 ethylenedioxythiophene):poly-styrene-sulfonic acid (PEDOT:PSS) is a highly promising conducting polymer matrix for enzyme based biosensors due to its high enzyme immobilization capacity, good conductivity, good water solubility, high stability and biocompatibility [15,16]. Its combination with graphene should offer excellent performance biosensors. However, there have been very few reports that exploit this material combination for biosensing. Recently, non-enzymatic electrochemical sensors based on graphene–PEDOT:PSS (GP-PEDOT:PSS) film have been demonstrated for highly sensitive electrochemical sensing of salbutamol, hydrogen peroxide (H_2O_2), nicotinamide adenine dinucleotide (NAD^+) and $Fe(CN)_6^{3-/4-}$ redox couple [17,18]. H_2O_2 and NAD^+ are common products of many enzymatic reactions and thus GP-PEDOT:PSS should be highly effective for enzyme-based biosensing.

In this work, electrochemically synthesized graphene–PEDOT:PSS (GP-PEDOT:PSS) nanocomposite is demonstrated as a new and practically useful material platform for highly sensitive enzyme-based electrochemical detection. Glucose is used as the model analyte as it is the most common biosubstrate for enzyme-based biosensing and its detection is always needed for human's health monitoring. In addition, its enzyme, glucose oxidase (GOD), is highly useful for direct electrochemistry study on novel electrode materials. Recently, the direct electrochemistry of GOD on graphene prepared by different methods has been evaluated [19–23]. In

* Corresponding authors. Tel.: +66 25646900 (A. Wisitsoraat).
E-mail addresses: anurat.wisitsoraat@nectec.or.th (A. Wisitsoraat), adisorn.tuantranont@nectec.or.th (A. Tuantranont).

1572-6657/$ - see front matter © 2013 Elsevier B.V. All rights reserved.
http://dx.doi.org/10.1016/j.jelechem.2013.07.012

this study, the direct electrochemistry of GOD on graphene in the presence of PEDOT:PSS matrix is also investigated.

2. Materials and methods

2.1. Reagents and apparatus

All of chemicals used in this work were analytical grade and used without further purification. D-glucose, glucose oxidase (GOx, Pseudomonas fluorescens 250 U/mg), glutaraldehyde, acetaminophen, ascorbic acid and uric acid were purchased from Sigma (USA). Phosphate buffer (PB) solution (pH 6.8–7.4) was made from sodium dihydrogen phosphate (Fluka, Switzerland) and disodium hydrogen phosphate (Fluka). Graphite rods (1/4″ dia, Electron Microscopy Science) were starting material for graphene synthesis. A commercial PEDOT:PSS solution (clevios P jet N from HC Starck, USA) was utilized as an electrolyte for electrolytic exfoliation. Screen printed carbon paste electrodes (SPCEs) were fabricated in-house at King Mongkut University of Technology at Thonburi, Thailand. A potentiostat (μ-autolab Type III, Metrohm, Switzerland) and a home-made electrochemical cell comprising a 3 ml cylindrical acrylic cell, a modified SPCE working electrode, a platinum (Pt) wire counter electrode and a silver/silver chloride (Ag/AgCl) reference electrode were used for all CV and amperometric measurements.

2.2. Preparation of GOD/GP-PEDOT:PSS modified electrodes

Graphene–PEDOT:PSS was synthesized by the electrolytic exfoliation procedure reported elsewhere [17,18]. The SCPE was then modified by GOD/GP-PEDOT:PSS by drop coating method. Firstly, GP-PEDOT:PSS solution (5 μl) was dropped on SPCE over an area of 3 mm × 5 mm and then allowed to dry in air at room temperature (25 °C) for 3 h. For enzyme immobilization, 50 μL of GOD enzyme solution (10 mg/0.4 ml) was mixed with 20 μl of 2%vol glutaraldehyde cross-linking solution. High GOD concentration of 2000 U/ml was used to ensure maximum activity in 0.1 M PB buffer solution [24]. The mixed solution (5 μl) was then dropped on GP-PEDOT:PSS layer and allowed to absorb and dry in air at room temperature for 12 h. The prepared GOD/GP-PEDOT:PSS-modified electrode was then stored at room temperature during the entire measurement process. The surface morphology and functional groups of GOD/GP-PEDOT:PSS films were characterized by scanning electron microscope (SEM, Hitachi model S-4700) and Fourier transform infrared spectroscope (FTIR, Perkin Elmer model spectrum spot light-300).

2.3. Electrochemical measurement

CV measurements for direct electrochemistry of GOD in PB buffer and 1 mM D-glucose was conducted over a potential window between −0.8 and +0.2 V at 100 mV scan rate as redox peaks for GOD appeared within this potential range. The electrochemical response towards glucose of GP-PEDOT:PSS modified SPCEs were then measured by chronoamperometry at a constant potential in the reduction regime with the non-aerated buffer solution. It should be noted that the solution was not aerated because inherent oxygen in the PB buffer solution was found to be sufficient for related electrochemical reactions. The stock solution of D-glucose (15.6 mM) was prepared in PB buffer (0.1 M, pH 7.0). The effect of potential was studied by varying the reduction potential from −0.1 V to −0.6 V. In amperomentric measurements, 10 μl of D-glucose solution was injected for every 90 s into the electrochemical cell containing 4 ml of buffer solution. For interference study, 10 μl of uric acid (2 mM), ascorbic acid (2 mM) and acetaminophen (2 mM) were successively injected into the buffer solution prior to glucose detection.

3. Results and discussions

3.1. Structural characteristics of GOD/GP-PEDOT:PSS

The surface morphologies of unmodified SPCE, GOD/PEDOT:PSS SPCE and GOD/GP-PEDOT:PSS SPCE at different magnifications are illustrated in Fig. 1(a–f), respectively. It can be seen that uncoated SPCE has rough porous surface with large flakes and pits of several microns in size. After drop coating with GOD/PEDOT:PSS, the surface becomes smoother and contains some long stripe structures. Such stripe features were not observed from PEDOT:PSS and GP-PEDOT:PSS SPCE surface [17] and hence they should correspond to the presence of GOD and glutaraldehyde cross linker. For the case of GOD/GP-PEDOT:PSS SPCE, relatively large stripes are clearly seen and mixed with some micron-sized oval and rounded polygonal sheets. The sheets were confirmed to be multi-layer graphene structures by transmission electron microscopy and Raman spectroscopy reported previously [17,18].

The functional groups of GOD/PEDOT:PSS and GOD/GP-PEDOT:PSS films were characterized by FTIR as illustrated in Fig. 2. It can be seen that both spectra contain expected bands of functional groups from PEDOT:PSS and GOD, confirming successful enzyme immobilization. Peaks at 1157, 1121 and 1012 cm^{-1} are attributed to S–O and S-phenyl bonds in sulfonic acid and peaks at 1532, 1356, 952, 845 and 704 cm^{-1} arise from C═C, C–C and C–S bonds in thiophene backbone. In addition, peptide groups and linkages in the GOD backbone contribute to C–N bending band at 740–800 cm^{-1}, COOH peak at 1400 cm^{-1}, the combination of N–H bending and C–N stretching peak of Amide II at ∼1,570 cm^{-1} and C═O stretching peak of Amide I at ∼1650 cm^{-1} [25]. Moreover, GOD/GP-PEDOT:PSS film evidently shows more pronounced peaks from the GOD group than GOD/PEDOT:PSS one. Thus, graphene should help improving GOD immobilization on SPCE. Moreover, graphene does not contribute additional functional group to the mixture but causes perturbations of some peak amplitudes and locations.

3.2. Performance of GOD/GP-PEDOT:PSS modified SPCE

3.2.1. Direct electrochemistry of GOD on GP-PEDOT:PSS

The direct electrochemistry of GOD on GOD/GP-PEDOT:PSS modified SPCE is evaluated from CV responses in 0.1 M PB solution (pH 7.0) and compared to that of GOD/PEDOT:PSS and GOD modified SPCEs as shown in Fig. 3. The CVs from these electrodes in the absence of GOD are also shown for comparison. It can be seen that only GOD/GP-PEDOT:PSS modified SPCE (curve f) exhibits a pair of well-defined redox peaks while GOD on PEDOT:PSS modified (curve e) and unmodified SPCE (curve b) essentially have no clear oxidation or reduction peak. In the absence of GOD, PEDOT:PSS (curve c) and GP-PEDOT:PSS (curve d) modified and unmodified (curve a) SPCEs also show no evident redox peak. Hence, the observed peaks are not directly caused only by the presence of graphene and PEDOT:PSS. Nevertheless, it can be observed that for PEDOT:PSS (curve c) GP-PEDOT:PSS (curve d) and GOD/PEDOT:PSS (curve e) modified SPCEs exhibit some anodic current increase. Such anodic current is not an actual oxidation peak but is known to correspond to Faradic charging of PEDOT:PSS matrix [26]. Thus, it may be concluded that the combination of graphene and GOD gives rise to the redox peaks that correspond to the direct electron transfer of GOD.

A plausible mechanism of the direct electron transfer between GOD and SPCE through graphene in PEDOT:PSS is depicted in Fig. 4. It illustrates FAD (Flavin adenine dinucleotide), electroactive

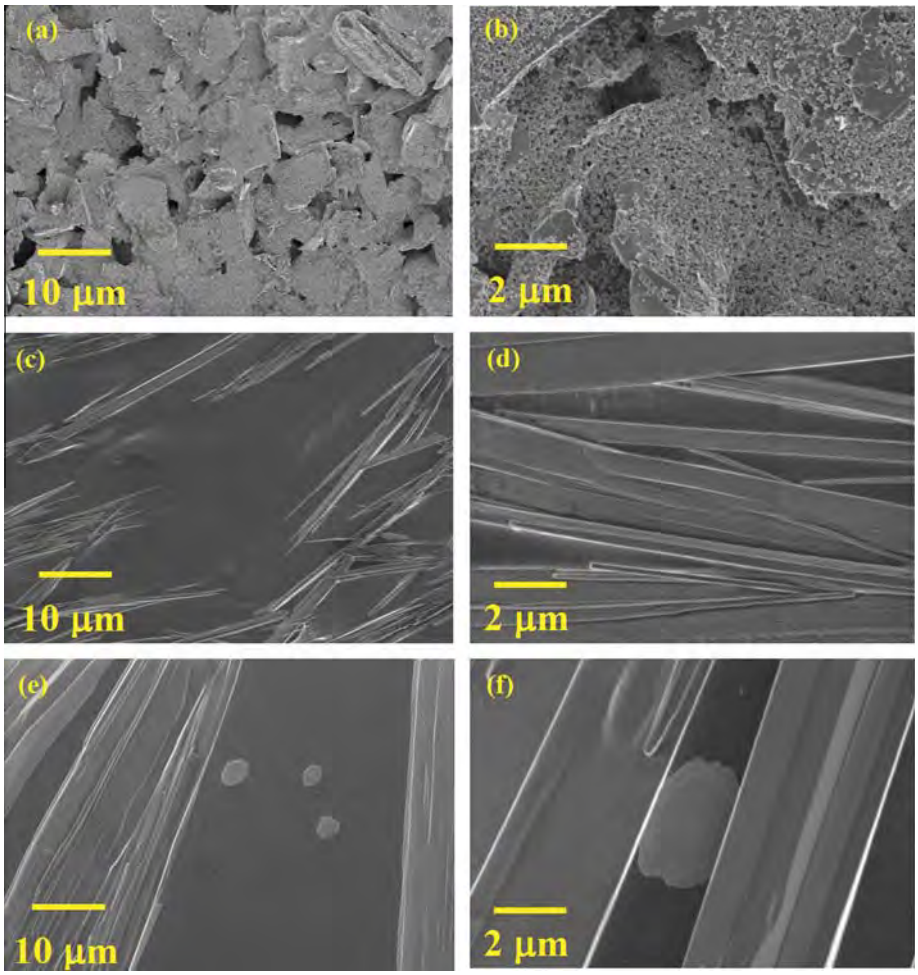

Fig. 1. SEM images of the surfaces of (a and b) SPCE, (c and d) GOD/PEDOT:PSS/SPCE and (e and f) GOD/GP-PEDOT:PSS/SPCE. (a), (c) and (e) are images at low magnification while (b), (d) and (f) are those at high magnification.

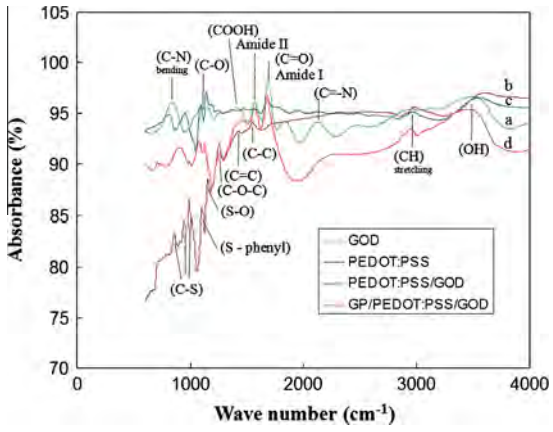

Fig. 2. FTIR spectra of: (a) GOD, (b) PEDOT:PSS, (c) GOD/PEDOT:PSS and (d) GOD/PEDOT:PSS on SPCEs.

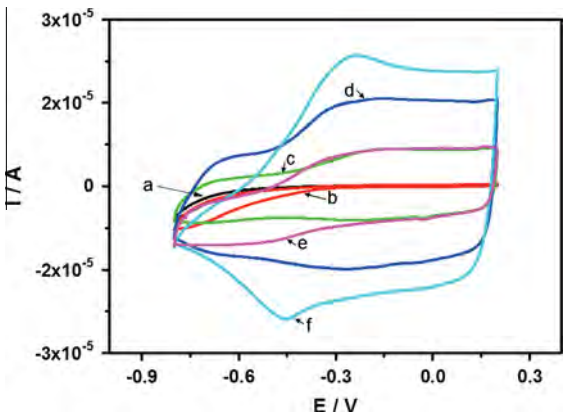

Fig. 3. Cyclic voltamograms of the: (a) SPCE, (b) GOD/SPCE, (c) PEDOT:PSS/SPCE, (d) GP-PEDOT:PSS/SPCE (e) GOD/PEDOT:PSS/SPCE and (f) GOD/GP-PEDOT:PSS/SPCE in PB pH 7.0 at a scan rate of 100 mV/s.

center of GOD, generation by oxidation of $FADH_2$ (the reduced form of FAD), which produces 2 electrons ($2e^-$) and 2 protons ($2H^+$) [27]. The generated electrons will then conduct to SPCE electrode via the shortest resistance path (dotted red arrow lines) through highly conductive graphene sheets dispersed in PEDOT:PSS matrix as illustrated in Fig. 4 while protons will travel to the other pathway (not drawn to avoid confusion) through graphene–PEDOT:PSS into the buffer solution. The analogous reduction process can be explained conversely. Without graphene, electrons and protons will have to go through PEDOT:PSS medium, which has considerable resistance that causes significant potential drop and much lower electron transfer rate. Therefore, graphene plays an important role in facilitating the electron exchange between GOD and SPCE because it forms conductive matrix leading to reduced electrical resistance paths.

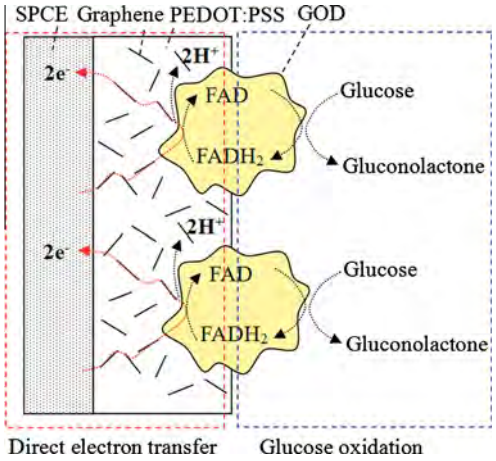

Fig. 4. Mechanisms of the direct electron transfer between GOD and SPCE through graphene in PEDOT:PSS and glucose detection in reduction regime.

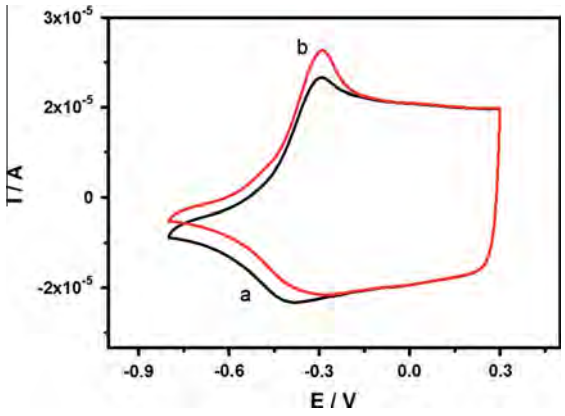

Fig. 5. Cyclic voltamograms of the GOD/GP-PEDOT:PSS/SPCE for: (a) 0 mM and (b) 1 mM D-glucose solution in PB pH 7.0 at a scan rate of 100 mV/s.

The cathodic peak potential for GOD reduction is −0.46 V vs. Ag/AgCl, the peak potential separation (ΔE_p) is 160 mV and the corresponding formal potential is −0.39 V vs. Ag/AgCl while the ratio of the maximum cathodic current over the anodic one is 1.01 (23.4/23.2), which is very close to 1. The potential value is somewhat lower compared with the standard formal potentials (−0.46 V) for the conversion between GOD(FAD) and GOD($FADH_2$) at pH 7.0 [28,29]. In addition, the shapes of oxidation and reduction peaks are not symmetric, indicating that GOD undergoes a quasi-reversible redox process at the GP/PEDOT:PSS electrode. The ratio of the area under oxidation peak over that of reduction one is estimated to be 0.75. The reversibility of redox process may be deteriorated by the presence of the insulating PSS matrix in PEDOT:PSS copolymer that causes some asymmetric electrochemical resistance. Moreover, it can be noticed that graphene and PEDOT:PSS additively give rise to the large background current due possibly to very large catalytically active surface area of PEDOT:PSS and graphene, which was confirmed to be 422.7 $m^2 g^{-1}$ by BET measurement reported previously [18].

3.2.2. Effect of applied potential on glucose detection

The detection potential generally affects the sensitivity as well as selectivity characteristics of current signal for bio-analytes. The optimum detection potential is directly related to oxidation and reduction potentials in CV. Typical CV curves of GOD/GP-PEDOT:PSS modified SPCE in the presence of 0 and 1 mM D-glucose solution in PB buffer (pH 7.0) are illustrated in Fig. 5. It is seen that oxidation peak at about −0.29 V, which is already present due to direct oxidation of $FADH_2$ in the absence of glucose, becomes more clearly pronounced in the presence of 1 mM D-glucose. The increased oxidation current can be attributed to the increased $FADH_2$ concentration generated from the oxidation of glucose to gluconolactone by FAD [27–29] as illustrated in Fig. 4. In contrast, the reduction peak at around −0.37 V, in which FAD is reduced to $FADH_2$, is diminished and reduction current decreases. This behavior is corresponding to the decrease of FAD concentration due to the same glucose oxidation process. Thus, the reduction current will decrease with glucose concentration due to restrained reduction of FAD and glucose concentration can be alternatively determined from the negative change of reduction current [27–29].

The glucose detection in the reduction regime is often preferred over the oxidation one due to lower interferences because of the absence of oxidations of many interfering species. Thus, chronoamperometric detection in reduction regime is employed in this study. Chronoamperometric detection mode offers higher sensitivity than CV and also provides real-time detection capability. The optimum detection potential in chronoamperometric mode may be somewhat different from the CV reduction potential due to the static nature of applied bias. Thus, the chronoamperometric response in a 0.2 mM glucose solution (0.1 M PB at pH 7.0) was optimized by varying the bias potential from −0.1 to −0.5 V in order to determine the actual optimal reduction potential. It was found that the steady-state reduction current rapidly increased as the applied potential varied from −0.1 to −0.4 V and then slightly decreased as the potential increased further. The optimum reduction current was thus attained at around −0.4 V and it was selected as the working potential for all subsequent measurements. It should be noted that direct electron transfer reaction at FAD was predominant over the reaction involving O_2 and H_2O_2 in this case and hence the electrode was not sensing H_2O_2.

3.3. Glucose detection performances of GOD/GP-PEDOT-PSS/SPCE

3.3.1. Concentration dependence characteristics

Amperometric glucose detection in reduction regime was performed over a concentration range of 0–2 mM using the optimized detection potential obtained from above studies. Calibration curve, response time, detection limits are then estimated from the amperometric responses. The amperometric response in reduction regime is defined here as the background subtracted reduction current, which corresponds to the reduction current change that is increasingly negative with glucose concentration. The amperometric response and corresponding calibration curves of GOD/GP-PEDOT:PSS and GOD/PEDOT:PSS modified SPCEs are shown in Fig. 6(a) and (b), respectively. It can be seen that GOD/GP-PEDOT:PSS electrode exhibits higher current response of more than one order of magnitude compared to GOD/PEDOT:PSS one. From the calibration curves (Fig. 6(b)), GOD/GP-PEDOT:PSS and GOD/PEDOT:PSS electrodes have considerably different sensitivities and linear ranges. GOD/GP-PEDOT:PSS has a high sensitivity of 7.23 μA/mM, which is about 13 times higher than that of GOD/PEDOT:PSS. However, GOD/GP-PEDOT:PSS electrode has a relatively narrow linear dynamic range of ~20–900 μM compared to that of GOD/PEDOT:PSS of ~200–1700 μM. Moreover, GOD/GP-PEDOT:PSS offers a very low detection limits (3S/N) of ~0.3 μM compared to ~10 μM for GOD/PEDOT:PSS one. The dynamic range is somewhat below the general range of glucose detection of 10 mM and is thus not sufficient for diabetes applications [32]. Nevertheless, the detection limit and linear dynamic range are better or comparable to other recent reports of highly sensitive glucose biosensors whose detection limits are in the range of 0.1–1 μM and the maximum limit of dynamic range are varied

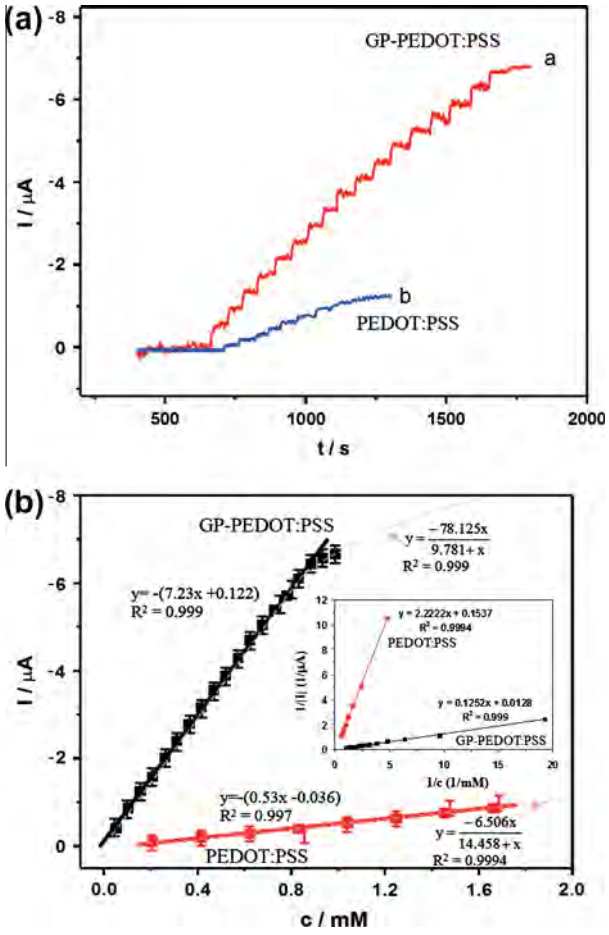

Fig. 6. (a) Amperometric responses and (b) calibration curve of GOD/GP-PEDOT:PSS/SPCE and GOD/PEDOT:PSS/SPCE at −0.4 V upon successive addition of glucose. Inset: corresponding Lineweaver–Burk plots.

between 0.3 and 10 μM [10,21,30–38]. Therefore, graphene provides a dramatic enhancement of glucose detection performance and GP-PEDOT:PSS is a highly promising candidate for enzyme-based biosensors. This can be attributed to efficient direct electrochemistry of grahene on GOD, excellent electron transfer rate, huge reactive surface area and high electronic mobility of GP-PEDOT:PSS composite. The role of PEDOT:PSS is to help stabilizing graphene dispersion, preventing graphene agglomeration and retaining large reactive surface area of graphene as suggested by FTIR and BET data. It should be noted that the error bars in Fig. 6 represent the variation of current response of 10 equally prepared sensors, which confirms the stability and reproducibility of current response of the GOD/GP-PEDOT:PSS electrode.

To further analyze the GOD enzyme performance in PEDOT:PSS and GP-PEDOT:PSS, the Michaelis–Menten (M–M) constant (K_m) of GOD is calculated from Lineweaver–Burk (1/current vs. 1/concentration) plots as illustrated in the inset of Fig. 6(b). The resulting M–M equations for both cases are shown by dotted curve as illustrated Fig. 6(a). It is evident that the enzymatic reaction of GOD in PEDOT:PSS and GP-PEDOT:PSS is very well conformed to Michaelis–Menten kinetics, in which a single substrate reaches equilibrium much faster than the formation of products. The saturation of current for enzyme/GP-PEDOT:PSS electrode can be seen at a concentration above 1 mM while the saturation of current for enzyme/PEDOT:PSS electrode is not apparent because the current is still far below its saturation region. K_m of GOD (denominator of M-M equation in Fig. 6(a)) for PEDOT:PSS and GP-PEDOT:PSS are estimated to be 14.5 and 9.8 mM, respectively. The lower value of K_m in GP-PEDOT:PSS indicates that the substrate's affinity to enzyme is improved due to the presence of graphene in PEDOT:PSS, which in effect results in faster enzymatic reaction. The enzymatic saturation currents (numerator of M-M equations in Fig. 6(a)) for PEDOT:PSS and GP-PEDOT:PSS are estimated to be 6.5 and 78.1 μA, respectively. The much higher saturation current of GP-PEDOT:PSS electrode suggests a much higher enzymatic activity of GOD in GP-PEDOT:PSS electrode. Furthermore, the high saturation current value of GP-PEDOT:PSS electrode indicates that the detection range may considerably be extended beyond the linear range if nonlinear region is allowed to be used with the M–M calibration equation.

3.3.2. Interference study

Specificity is one of the most critical issues for biosensors to be used in real environment. To evaluate specificity of the biosensors, interferences were tested at physiological concentrations of three most important interfering species including uric acid (2 mM), ascorbic acid (2 mM) and acetaminophen (2 mM) as illustrated in Fig. 7. It is evident that ascorbic acid, uric acid and acetaminophen give negligible interference signals. The interferences from these analytes are very low as expected because the working electrode potential is set at a suitably low value of −0.4 V in reduction regime so that only specific reduction by GOD enzymes is predominant.

3.3.3. Repeatability and reproducibility

The repeatability was evaluated from a relative standard deviation (R.S.D.) of the current responses from successive electrochemical measurements to 0.2 mM glucose in 0.1 M PB (pH 7.0) at −0.4 V (vs. Ag/AgCl) on the same modified electrode while the reproducibility was measured in term of a relative standard deviation (R.S.D.) of the average current responses of a set of equally prepared biosensors under the same glucose measurement condition. The repeatability of the current response from a single sensor of PEDOT:PSS and GP-PEDOT:PSS layers were in the ranges of 3.21–4.76% and 4.27–5.65%, respectively. The repeatability values are considered acceptable for clinical diagnostic applications, which generally require sensor's repeatability of less than 5%. The reproducibility values of the current responses from 10 sensors fabricated from the same batch were 7.9% and 8.6% for GOD/PEDOT:PSS and GOD/GP-PEDOT:PSS electrodes, respectively. The reproducibility values are also satisfactory for commercial production.

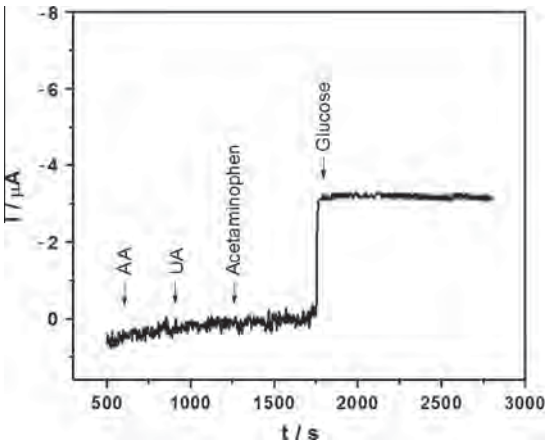

Fig. 7. Amperometric responses of GOD/GP-PEDOT:PSS/SPCE upon additions of ascorbic acid (AA) (2 mM), uric acid (UA) (2 mM), acetaminophen (2 mM) and glucose (0.5 mM), in PB pH 7.0 at potential of −0.4 V.

3.3.4. Storage stability

The stability of the biosensor under storage was determined by measuring the biosensor response in 0.2 mM glucose in 0.1 M PB (pH 7.0) at −0.4 V (vs. Ag/AgCl) everyday and the electrodes were stored at 4 °C under dry condition when not in use. It was found that the current response of the biosensors decreased to 70% of the initial response after 30 successive days. The stability of the sensor is thus promising for practical applications.

4. Conclusion

In conclusion, this report presents the development of highly sensitive enzyme-based biosensor based on GP-PEDOT:PSS modified SPCE for electrochemical detection of glucose. GP-PEDOT:PSS nanocomposite is synthesized by one-step electrolytic exfoliation method and drop-coated on SPCE. GOD enzyme is then immobilized on GP-PEDOT:PSS by glutaraldehyde cross linking. SEM image indicates that GOD/GP-PEDOT:PSS/SPCE surface is smooth and covered with long microstripes of GOD. From CV measurement, direct electrochemistry of GOD at the GP/PEDOT:PSS electrode is observed and graphene plays the main role in a quasi-reversible redox process. GOD/GP-PEDOT:PSS has a high amperometric sensitivity of 7.23 μA/mM, which is about 13 times higher than that of GOD/PEDOT:PSS but has a relatively narrow linear dynamic range of ∼20–900 μM. Moreover, GOD/GP-PEDOT:PSS offers a very low detection limits (3S/N) of ∼0.3 μM, which is better or comparable to other recent reports of highly sensitive glucose biosensors. Furthermore, the sensor has good stability with only 30% loss of enzyme activity after 30 days if always kept under cool storage at 4 °C.

Acknowledgements

Authors would like to acknowledge research grant under project P1201107 from National electronics and computer technology center, National science and technology development agency. A. Tuantranont would like to express his gratitude for Researcher Career Development Grant from Thailand Research Fund (TRF).

References

[1] K. Wang, J. Ruan, H. Song, J. Zhang, Y. Wo, S. Guo, D. Cui, Nanoscale Res. Lett. 6 (2010) 1–8.
[2] Y. Shao, J. Wang, H. Wu, J. Liu, I.A. Aksay, Y. Lin, Electroanalysis 22 (2010) 1027–1036.
[3] X. Kang, J. Wang, H. Wu, J. Liu, I.A. Aksay, Y. Lin, Talanta 81 (2010) 754–759.
[4] S. Alwarappan, A. Erdem, C. Liu, C.Z. Li, J. Phys. Chem. C 113 (2009) 8853–8857.
[5] M. Pumera, A. Ambrosi, A. Bonanni, E.L.K. Chng, H.L. Poh, Anal. Chem. 29 (2011) 954–965.
[6] S. Mao, K. Yu, G. Lu, Nano Res. 4 (2011) 921–930.
[7] K.R. Ratinac, W. Yang, J.J. Gooding, P. Thordarson, F. Braet, Electroanalysis 23 (2011) 803–826.
[8] J. Wang, Electroanalysis 17 (2005) 7–14.
[9] S. Park, N. Mohanty, J.W. Suk, A. Nagaraja, J. An, R.D. Piner, W. Cai, D.R. Dreyer, V. Berry, R.S. Ruoff, Adv. Mater. 22 (2010) 1736–1740.
[10] Q. Yan, B. Huang, J. Yu, F. Zheng, J. Zang, J. Wu, B.L. Gu, F. Liu, W. Duan, Nano Lett. 7 (2007) 1469–1473.
[11] M.J. Allen, V.C. Tung, R.B. Kaner, Chem. Rev. 110 (2009) 132–145.
[12] V. Singh, D. Joung, L. Zhai, S. Das, S.I. Khondaker, S. Seal, Prog. Mater. Sci. 56 (2011) 1178–1271.
[13] C. Soldano, A. Mahmood, E. Dujardin, Carbon 48 (2010) 2127–2150.
[14] G. Wang, B. Wang, J. Park, Y. Wang, B. Sun, J. Yao, Carbon 47 (2009) 3242–3246.
[15] J. Liu, M. Agarwal, K. Varahramyan, Sens. Actuat. B 135 (2008) 195–199.
[16] S.M. Richardson-Burns, J.L. Hendricks, B. Foster, L.K. Povlich, K. Dong-Hwan, D.C. Martin, Biomater. 28 (2007) 1539–1552.
[17] C. Sriprachuabwong, C. Karuwan, A. Wisitsorrat, D. Phokharatkul, T. Lomas, P. Sritongkham, A. Tuantranont, J. Mater. Chem. 22 (2012) 5478–5485.
[18] C. Karuwan, C. Sriprachuabwong, D. Phokharatkul, A. Wisitsorrat, P. Sritongkham, A. Tuantranont, Sensors Actuat. B 161 (2012) 549–555.
[19] J. Lu, L.T. Drzal, R.M. Worden, I. Lee, Chem. Mater. 19 (2007) 6240–6246.
[20] C. Shan, H. Yang, J. Song, D. Han, A. Ivaska, L. Niu, Anal. Chem 81 (2009) 2378–2382.
[21] X. Wu, F. Zhao, J.R. Varcoe, A.E. Thumser, C. Avignone-Rossa, R.C.T. Slade, Bioelectrochem. 77 (2009) 64–68.
[22] M. Zhou, Y. Zhai, S. Dong, Anal. Chem. 81 (2009) 5603–5613.
[23] Q. Zhang, S. Wu, L. Zhang, J. Lu, F. Verproot, Y. Liu, Z. Xing, J. Li, X. Song, Biosens. Bioelectron. 26 (2011) 2632–2637.
[24] D.J. Shirale, V.K. Gade, P.D. Gaikwad, P.A. Savale, H.J. Kharat, K.P. Kakde, A.J. Pathan, M.D. Shirsat, Int. J. Electrochem. Sci. 1 (2006) 62–70.
[25] W. Liang, Y. Zhoubin, Sensors 3 (2003) 544–554.
[26] H.W. Siao, S.M. Chen, K.C. Lin, J. Solid State Electrochem. 15 (2011) 1121–1128.
[27] R. Cui, Z. Han, J. Pan, E.S. Abdel-Halimb, J.-J. Zhuc, Electrochimica Acta 58 (2011) 179–183.
[28] M. Shim, N.W.S. Kam, R.J. Chen, Y.M. Li, H.J. Dai, Nano Lett. 2 (2002) 285–288.
[29] X. Xu, J. Chen, W. Li, Z. Nie, S. Yao, Electrochem. Commun. 10 (2008) 1459–1462.
[30] B.Y. Wu, S.H. Hou, F. Yin, Z.X. Zhao, Y.Y. Wang, X.S. Wang, Q. Chen, Biosens. Bioelectron. 22 (2007) 2854–2860.
[31] Y.-L. Yao, K.-K. Shiu, Electroanalysis 20 (2008) 1542–1548.
[32] P. Lian, X. Zhu, S. Liang, Z. Li, W. Yang, H. Wang, Electrochimica Acta 55 (2010) 3909–3914.
[33] A. Heller, B. Feldman, Chem. Rev. 108 (2008) 2482–2505.
[34] H. Li, J. He, Y. Zhao, D. Wu, Y. Cai, Q. Wei, M. Yang, Electrochim. Acta 56 (2011) 2960–2965.
[35] D. Ragupathy, A.I. Gopalan, K.P. Lee, K.M. Manesh, Electrochem. Commun. 10 (2009) 527–530.
[36] S. Zhao, K. Zhang, Y. Bai, W. Yang, C. Sun, Bioelectrochemistry 69 (2006) 158–163.
[37] S. Zuo, Y. Teng, H. Yuan, M. Lan, Sens. Actuat. B 133 (2008) 555–560.
[38] C. Deng, J. Chen, Z. Nie, S. Si, Biosens. Bioelectron. 26 (2010) 213–219.

Sensors and Actuators B 176 (2013) 428–436

Contents lists available at SciVerse ScienceDirect

Sensors and Actuators B: Chemical

journal homepage: www.elsevier.com/locate/snb

Inkjet-printed sol–gel films containing metal phthalocyanines/porphyrins for opto-electronic nose applications

Johannes Ph. Mensing[a], Anurat Wisitsoraat[b], Adisorn Tuantranont[b], Teerakiat Kerdcharoen[c,d,*]

[a] Materials Science and Engineering Programme, Faculty of Science, Mahidol University, Bangkok, Thailand
[b] Nanaoelectronics and MEMS Laboratory, National Electronics and Computer Technology Center, 112 Pahol Yothin Road, Klong Luang, Pathumthani, Thailand
[c] Center of Nanoscience and Nanotechnology, Department of Physics, Faculty of Science, Mahidol University, Rama 6 Road, Bangkok, Thailand
[d] NANOTEC Center of Excellence at Mahidol University, Nanotechnology Center, Thailand

ARTICLE INFO

Article history:
Received 14 June 2012
Received in revised form
11 September 2012
Accepted 16 September 2012
Available online 8 October 2012

Keywords:
Sol–gel method
Inkjet printing
Optical gas sensing
Metallo phthalocyanine
Metallo porphyrin

ABSTRACT

In this work, five metal porphyrins and phthalocyanines embedded in transparent sol–gel films were deposited by piezoelectric inkjet printing, characterized and used as gas sensors. Explored compounds include magnesium/manganese(III) chloride/zinc 5,10,15,20-tetraphenyl-21H,23H-porphyrin, magnesium 2,3,7,8,12,13,17,18-octaethyl-21H,23H-porphine, and zinc 2,9,16,23-tetratertbutyl-29H,31H-phthalocyanine. Porphyrin/Phthalocyanine was blended with sol–gel solution to produce inks that were printed on glass substrates. The printed films were used as sensing layers for discrimination of volatile organic compounds (VOCs). Printed films were characterized by UV/vis spectroscopy, FTIR spectroscopy, and scanning electron microscopy. The employed sensing compounds are promising materials for optical gas sensors due to selective spectral alterations when exposed to oxidizing and reducing gases as well as VOCs. These alterations were observed by UV/vis spectroscopy and used to distinguish between several VOCs. To do so, a single printed sensing layer was exposed to methanol, ethanol, acetone and isopropanol vapor, respectively. During exposure the absorbance spectrum was continually measured and split into several wavelength intervals. By calculating the area integral of each interval and considering these as separate sensors it is possible to use a single sensing film to emulate sensor arrays. The results showed that the fabricated layers exhibit reversible optical modulations in the UV/vis spectra when exposed to various VOCs. The data have been analyzed by principal component analysis (PCA) and cluster analysis (CA). Results demonstrate the analytes to be distinguishable as isolated clusters in the PCA domains. The best results were obtained from ZnTPP and MgTPP containing films, whereas layers doped with Mn(III)ClTPP give unusable response.

1. Introduction

In the last few decades, the development of new materials for applications in the fields of gas and vapor sensing has become one of the most intriguing challenges for material scientists. These sensors are of great interest because of their richness of potential applications, such as the analysis and monitoring of environmental pollution, diagnostic control of human diseases, quality control for the beverage and food industry or the detection of flammable, explosive, toxic or otherwise harmful gases [1]. Optical transduction offers a number of advantages over other sensing mechanisms, not the least of which is the availability of highly sophisticated instrumentation in the field of optics. The development in this area has been mainly driven by the needs of the telecommunications, entertainment, and computer industries and the demand for more efficient fiber optic communications, projection devices, optical information storage, etc. These advances are tremendously beneficent for optical sensors which make use of changes in optical properties of an active material that is exposed to analyte as transduction means. Examples are modulations in fluorescence, refractive index, scattering, polarization, interference or absorbance. They are used in various fields such as biomedicine, clinical, environmental monitoring and process controlling. Real world applications are, for instance, tracking sources of contamination in industrial processes or triggering alarm when a toxic species exceeds a permitted concentration [2].

Metal phthalocyanines (MePc) and metal porphyrins (MeP) are promising active materials for the development of optical sensors. These compounds, possessing high chemical and thermal stability, play an important role in technical applications as well as in natural processes. For instance, MePcs are used as organic dyes in the

* Corresponding author at: Center of Nanoscience and Nanotechnology, Department of Physics, Faculty of Science, Mahidol University, Rama 6 Road, Bangkok, Thailand. Tel.: +66 866037395; fax: +66 22015843.
E-mail addresses: adisorn.tuantranont@nectec.or.th (A. Tuantranont), teerakiat.ker@mahidol.ac.th, teerakiat@yahoo.com, sctkc@mahidol.ac.th (T. Kerdcharoen).

0925-4005/$ – see front matter © 2012 Elsevier B.V. All rights reserved.
http://dx.doi.org/10.1016/j.snb.2012.09.053

textile, automobile and paper industry, whereas MePs constitute basic building blocks for such vital molecules as heme or chlorophyll. What makes MePcs and MePs especially interesting for optical gas sensing is the fact that they exhibit easily detectable alterations of optical properties when exposed to oxidizing or reducing gases as well as weakly interacting volatile organic compounds (VOCs), due to their open coordination sites for ligation of analyte molecules and their intense coloration. Research of various groups has demonstrated that optical gas sensors based on pure MePc and MeP thin films are suitable for detection and discrimination of VOCs, exhibiting significant solvatochromic effects, even with weakly interacting vapors, e.g. arenes, halocarbones or ketones [1,3–8]. Reported fabrication methods for MePc and MeP thin films include, for instance, the Langmuir–Blodgett technique [7], glow discharge induced sublimation [5], spin coating [9], self-assembly [10], or vacuum evaporation [11]. Moreover, the optical sensing performances of pure metal phthalocyanine and metal porphyrin thin films prepared by these methods have been widely demonstrated. These reports show the direct applicability of MePc and MeP materials as active sensing layers.

One way to enhance the performance of a chemical sensing device is to combine unspecific sensor elements into a sensor array. This approach, employed in commercially available e-nose devices, mimics the functioning principle of the mammalian olfactory system. In order to do so, a sensor array is produced from multiple sensor elements of similar type, which are assembled in close proximity and exhibit cross sensitivity, i.e., the sensor elements react toward the same analytes with differing responses. In this way, complex and ideally unique signal patterns can be obtained. Further analysis with pattern recognition methods allows the identification of analytes. By using changes in the UV/vis absorbance spectrum during exposure to analytes as transduction mechanism, it is possible to consider the entire spectrum as a collection of independent sensors. Interactions between the sensing material and analytes will affect parts of the spectrum unequally, i.e. in some spectral interval the intensity may increase/decrease or red/blue shifts can occur. By dividing the spectrum into several wavelength intervals and continually measuring the area integral of these intervals, one can obtain sensing responses similar to responses obtained with sensor arrays that consist of several physically independent sensors. Data that is gathered in this manner can be used for classification of analytes by applying pattern recognition methods such as PCA and CA. PCA is a variable-oriented method for transforming the original measurement variables into new, uncorrelated variables called principal components (PC). They are ordered so that the first few PCs retain the greatest amount of variance in the original data set and most of the desired information is preserved [14,15]. Cluster Analysis (CA) is an unsupervised, non-parametric discrimination method widely used to distinguish between response vectors in n dimensional space by enhancing their differences. It is employed to identify clusters to which unknown vectors are likely to belong, in order to find a set of clusters for which samples within it are more similar than samples from the other clusters [16].

Inks based solely on a solvent/dye blend exhibit poor printability. In order to formulate inks with better properties, the applicability of a sol–gel method was investigated. The sol–gel technique produces porous glass or glass-like materials, which can be excellent matrices for gas-sensitive molecules. Alkoxides, $M(OR)_z$ (where M^{z+} is a metal/semi-metal ion and R is an alkyl group), are usually used as precursors in the sol–gel processes. In the presence of water molecules, these compounds undergo hydrolysis and then condensation [17]. In this work, silicon alkoxides have been used to produce gels. The sol–gel method makes it possible to print transparent films with high surface areas and porosity, which possess good optical characteristics and appropriate mechanical stability. Furthermore, they are chemically inert and exhibit high photochemical and thermal stability. The entrapment of dopant molecules can be achieved by simply mixing them into the liquid sol–gel before gelation, which also ensures their uniform distribution. Upon solidification of the gel, the dopant molecules will be embedded in the gel matrix [18]. Due to the porosity of the matrix material, it is possible for analyte molecules to diffuse into the layers and interact with the dye molecules leading to detectable optical property changes. MePc/MeP containing sol–gel matrices have also been studied [12]. The study results show that the optical properties of the sol–gel matrix are insignificantly affected by analyte vapor exposure and its effects on optical sensing behaviors of MePc/MeP are minimal. Thus, sol–gel process is suitable for preparation of MePc/MeP inks.

Inkjet printing offers several advantages over other methods for deposition of thin films, such as patterning capability, reduction of waste, high speed, low cost, room temperature deposition, applicability to large areas and flexible substrates. In addition, it provides direct patterning of a surface which does not rely on the use of expensive photolithographic masks. It also allows an operator great freedom with regard to the printed pattern and the thickness of deposited material [19]. Moreover, inkjet printing possesses certain advantages when compared to other common deposition methods for sensor fabrication such as spin coating, dip coating or manual pipetting. For instance, inkjet printing consumes very small quantities of coating material because ejected droplets will form layers only on the desired area and all material printed on the substrate will remain there, as opposed to spin or dip coating of which only a small amount of employed material will constitute the resulting layer. This is especially important when waste must be avoided, e.g. when working with materials which are toxic, expensive or not available in large quantity. Furthermore, properties of deposited layers can be more easily reproduced in terms of shape, thickness and uniformity, which are impossible to control with methods such as manual pipetting. Recently, it has been shown that inkjet printing is applicable to deposit sol–gel layers with embedded proteins [20–22]. However, no research has yet been reported concerning the inkjet printing of sol–gel layers doped with metal phthalocyanine/porphyrin for optical gas sensing applications.

2. Materials and methods

2.1. Sol–gel preparation

Sols containing tetraethyl orthosilicate (TEOS) and phenyl trimethoxysilane (PTMS) were prepared on the basis of the research of Suslick et al. [23]. Pure ethanol and de-ionized water were added into a glass container and stirred vigorously for 10 min. Thereafter TEOS and PTMS were added drop wise into the water/ethanol mixture. No catalysts were used in order to maintain a low reaction rate to avoid clogging of the printing head nozzles when the sol–gel is used as printing ink.

The so-prepared sol had a molar ratio of 1 (TEOS):1 (PTMS):11 (ethanol):5 (H_2O) and was again stirred for ~3 h. After an aging period of approximately one week, the gelation reaction led to an appropriate viscosity. Further aging would lead to increased viscosity due to an increased degree of gelation. Moreover, aged sol solidifies much faster when in contact with humidity. Thus, the aging time and humidity have significant effects on printability and must be properly controlled to ensure suitable viscosity and printability of the sol solution. Under proper process control, the reproducibility of the extended aging process is good with repeatable results obtained from several samples. Then, the sensing materials (depicted in Fig. 1a–d; purchased from Sigma and used as delivered) were added and mixed with the sol by sonication for approximately 1 h.

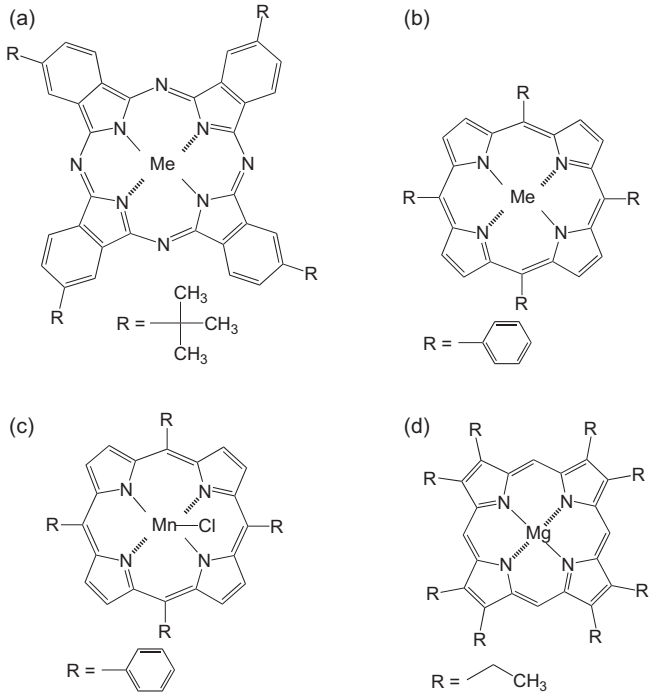

Fig. 1. (a) Metallo tetratertbutyl phthalocyanine (MeTTBPc); Me = Zn. (b) Metallo tetraphenyl porphyrin (MeTPP); Me = Mg, Zn. (c) Mn(III)chloride tetraphenyl porphyrin. (d) Magnesium octaethyl porphyrin.

2.2. Inkjet printing

A Fujifilm Dimatix DMP 2800 piezoelectric inkjet printer was used to fabricate sensing layers. Inks suitable for inkjet printing have to meet certain requirements including the viscosity of 10–12 cP at jetting temperature and surface tension of 28–33 dynes/cm. In addition, the boiling point of the ink should lie above 100 °C in order to avoid clogging of the print head nozzles caused by too rapid drying of the ink. It is also recommended to filter all fluids by 0.2 μm pore size. The printing process was controlled by the "Drop Manager" computer program provided with the printer. Applied printing parameters were 32 V firing voltage and usage of 8 jetting nozzles. A jetting waveform contains a single 20 μs pulse that falls into two steps. The meniscus vacuum was set to 4–4.5 in. H_2O and droplets were ejected at a frequency of 5 kHz. Layers were printed with a drop spacing of 10 μm on a square-shaped area of 5 mm × 5 mm and the number of printed layer was varied from 2 to 8. After drying, the printed layers were further thermally treated for 1 h at 80 °C and 150 °C, respectively, in order to solidify the films and enhance their sensing abilities by removal of the remaining solvent molecules and moisture.

2.3. Optical gas sensing

In order to perform optical gas sensing experiments a home-build gas flow setup was employed. Dry air was used as reference and carrier gas. Two computer-controlled mass flow controllers (MFC) were used to control the flow rate and to function as switching valves, which either direct the gas flow through a flask containing analyte or directly into the sensing chamber. By controlling individually the throughput of the MFCs, and thereby mixing dry air with saturated analyte vapor, it was also possible to set the analyte vapor concentration to the desired values. The glass substrates with the printed films were situated in the sensing chamber and transluminated by a tungsten–halogen light source via fiber optics guiding the light to an Ocean Optics USB40000 UV/vis spectrometer, which monitored the optical absorbance spectra in the range 400–800 nm. In order to evaluate the sensing response behavior of the printed layers, the samples were alternately exposed to dry air and a dry air/analyte vapor mixture with varying concentrations. The mixtures were generated by bubbling dry air through acetone, ethanol, isopropanol or methanol at 25 °C at a flow rate of 70, 175, 350 and 700 sccm, respectively. After that, the analyte flow is mixed with pure dry air to obtain the desired flow rate (700 sccm) and concentration. When exposed to the analytes, spectral alterations, i.e., in- or decrease of optical absorbance, occurred which lead to a changed value of the area integral of the spectra. These values were recorded over the time of the sensing experiments. In order to collect data for PCA and CA, the printed films were alternately exposed to the analyte vapor/dry air mixture for 10 min followed by dry air for another 10 min. The concentrations of the mixtures were (approximately): ethanol 60×10^3 ppm, methanol 100×10^3 ppm, isopropanol 50×10^3 ppm and acetone 170×10^3 ppm. The employed VOC concentrations of up to several thousand ppm are frequently encountered in electronic nose applications, in which the vapor source is situated in a closed flow system to ensure maximal saturation of the carrier gas with analyte molecules.

The optical absorbance spectrum of the sample was continually measured during analyte exposure and divided into 8 wavelength ranges with a width of 50 nm each (400–450, 450–500, 500–550, 550–600, 600–650, 650–700, 700–750, and 750–800 nm, respectively.) The area integral of each range was computed and recorded over time. When the film is exposed to VOC, changes in absorption occur in all the spectral ranges, which were treated as independent elements of an array. Sensor responses were calculated by $\Delta I(\%) = [(I_{gas} - I_0)/I_0] \times 100$; where I_{gas} are the integral values of the 8 ranges during analyte exposure and I_0 are the values during dry air recovery. Hence, $\Delta I = I_{gas} - I_0$ is dependent on the film thickness, it is necessary to remove this dependence by introducing $\Delta I(\%)$ [5]. Six analyte/dry air cycles are performed, resulting in an 8×6 matrix, which is then analyzed by PCA and CA.

3. Results and discussion

3.1. Characterization of printed layers

Heat treatment led to morphological changes resulting from the removal of remaining solvent molecules and further condensation of —Si—O—Si— groups. Films treated at 80 °C showed visible shrinkage due to the above-mentioned phenomena. However, if the layers were heated more strongly, i.e. at 150 °C, the internal stress resulting from the contractive forces became too large and the film became fractured and delaminated from the substrate. Hence, in the following, only films treated at 80 °C were investigated and discussed. Fig. 2 illustrates the thicknesses of films with different number of printed layers measured by a Polytec MSA-400 interferometer. It can be seen that the thickness increases linearly from 9 μm to 23 μm as the number of layers increases from 2 to 8. The error bars in the graph show the thickness standard deviation from 5 samples in each case. The results confirm that the ink-printing method yields high reproducibility with variation of less than 8%. The films have been further investigated by scanning electron microscopy (SEM) and Fourier transform infrared (FTIR) spectroscopy. SEM images show that undoped films appear to possess rather smooth surfaces the porosity of which could not be confirmed with the applied technique due to the limitation of the resolution of the microscope (Fig. 3a). Sol–gel films doped with sensing compounds exhibit more non-uniform surface morphologies as can be seen in Fig. 3b–d. The surface appears to be mainly smooth with clearly observable macropores (pore

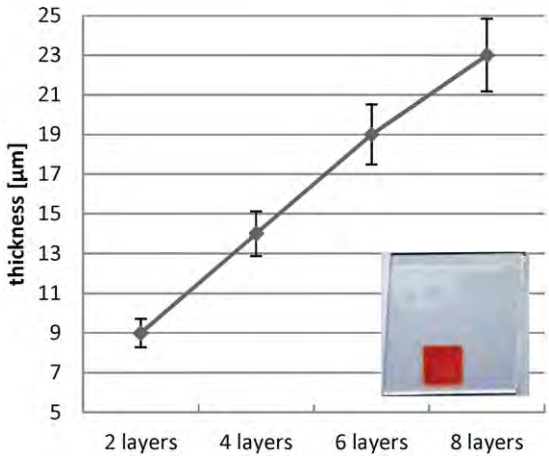

Fig. 2. Film thickness as a function of the number of printed layers. Inset: photograph of a printed film consisting of two layers; the color is due to ZnTPP.

diameters between ~0.2 and 0.5 μm). Areas of higher roughness are distributed randomly throughout the surface (c). Fig. 3d shows the edge of a printed layer on a substrate.

The influence of the heat treatment at 80 °C on the chemical structure of the sol–gel films has been further investigated by FTIR spectroscopy. Spectra of the printed sol–gel films with and without heat treatment (at 80 °C for 1 h) together with an uncoated glass substrate are shown in Fig. 4a. The as-printed film exhibited an absorption band around ~3500 cm^{-1} as associated with the stretching modes of Si—OH and adsorbed water. It also showed small residual features near ~2900–3100 cm^{-1} due to organic residues (alcohol, TEOS or PTMS). H-bonded silanols, which are believed to be located at the pore surfaces, can form chains of different lengths and shapes, giving rise to a corresponding broad band at ~3500–3600 cm^{-1}. Peaks around ~900 cm^{-1}, a more detailed view of which can be found in the inset to Fig. 4a, were due to vibrations of Si—OH or Si—O—. After the heat treatment, the bands related to OH stretching modes decrease in intensity which indicates a reduced amount of OH groups due to a higher degree of condensation [25–27].

The presence of hydroxyl groups is responsible for problems silica gels often suffer from, namely temporal degradation of properties such as white turbidity and shrinkage caused by the absorption of moisture from the air. This behavior can reduce the applicability of the printed films as optical sensors. Hence, heat treatment is advisable in order to reduce or overcome those shortcomings. In future work, this shortcoming will be tried to be overcome by replacing hydrophilic OH groups with hydrophobic —O—Si—$(CH_3)_3$ groups.

UV/vis spectra of layers containing metal porphyrins are dominated by an intense band between 400 and 500 nm, the Soret- or B-band which is related to $n \rightarrow \pi^*$ transitions of the lone nitrogen pair orbital of the macrocycle. These bands can be found in all tetrapyrroles that contain a fully conjugated nucleus. Furthermore, smaller bands between 550 and 630 nm were observed. These are the so-called Q bands which are assigned to $\pi \rightarrow \pi^*$ transitions.

The spectrum of ZnTTBPc-containing films is dominated by two Q bands, Q_I and Q_{II}, at about 680 nm and 630 nm, respectively, and a B-band centered at about 350 nm which lied outside of the observed spectral region [3,7,28,29]. UV/vis spectra are shown in Fig. 4b and exact peak denominations are given in Table 1.

3.2. Optical gas sensing

UV/vis spectra of the prepared layers undergo significant changes during exposure to analyte vapors. Fig. 5a and b shows spectral changes of ZnTTBPc and ZnTPP containing sol–gel layers before and during exposure to ethanol and isopropanol vapor,

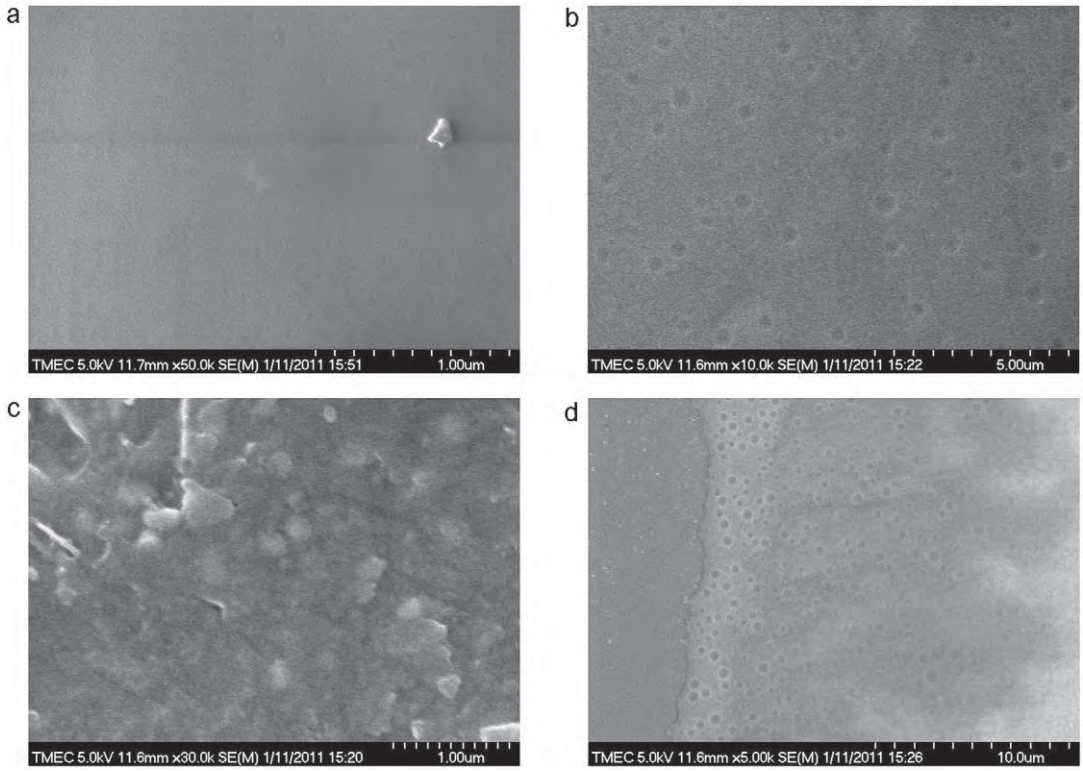

Fig. 3. (a) Undoped sol–gel film. The particle on the surface is probably dirt. (b) Film containing magnesium octaethyl porphyrin. Pores in the sol–gel film. (c) Film containing magnesium octaethyl porphyrin. Portions of the surface appear to be quite rough. (d) Film containing magnesium octaethyl porphyrin. Porous edge area of the printed films.

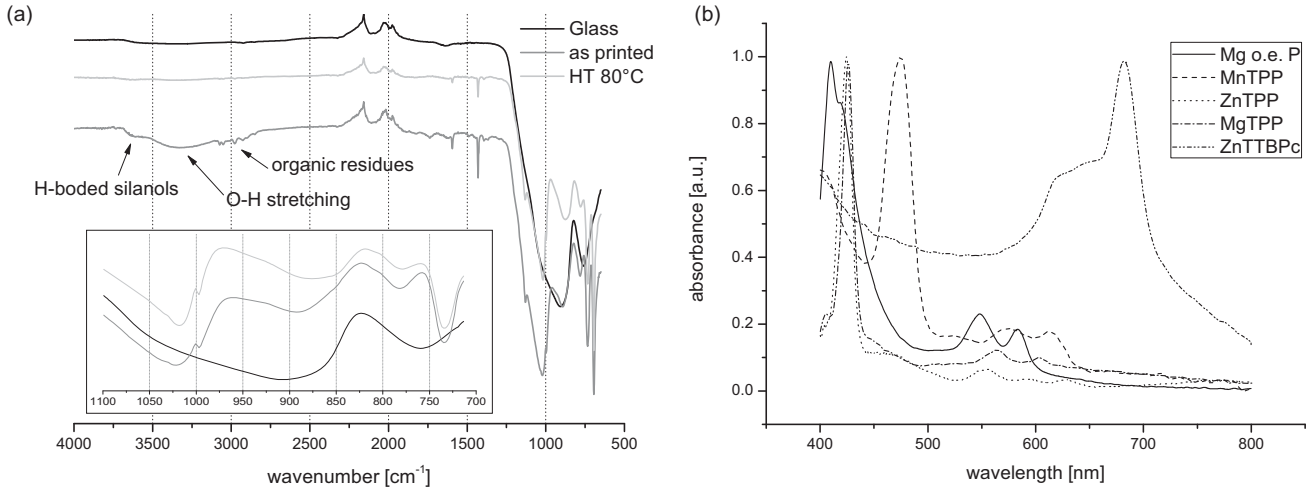

Fig. 4. (a) FTIR transmission spectra of a glass substrate, film as printed and film after heat treatment. Inset: spectra of as printed and heat treated specimen from 1100 cm^{-1} to 700 cm^{-1}. (b) UV/vis absorbance spectra of the investigated layers.

Table 1
UV/vis absorption peaks of inkjet-printed layers containing various sensing compounds between 400 and 800 nm.

Compound	Soret band	Q bands
MgTPP	426 nm (420 nm shoulder)	564 and 603 nm
MnTPP	474 nm	574 and 612 nm
ZnTPP	424 nm (460 nm shoulder)	553, 592 and 627 nm
Mg octaethyl porphyrin	410 nm (420 nm shoulder)	548 and 583 nm
ZnTTBPc	<400 nm	682 nm (630 nm shoulder)

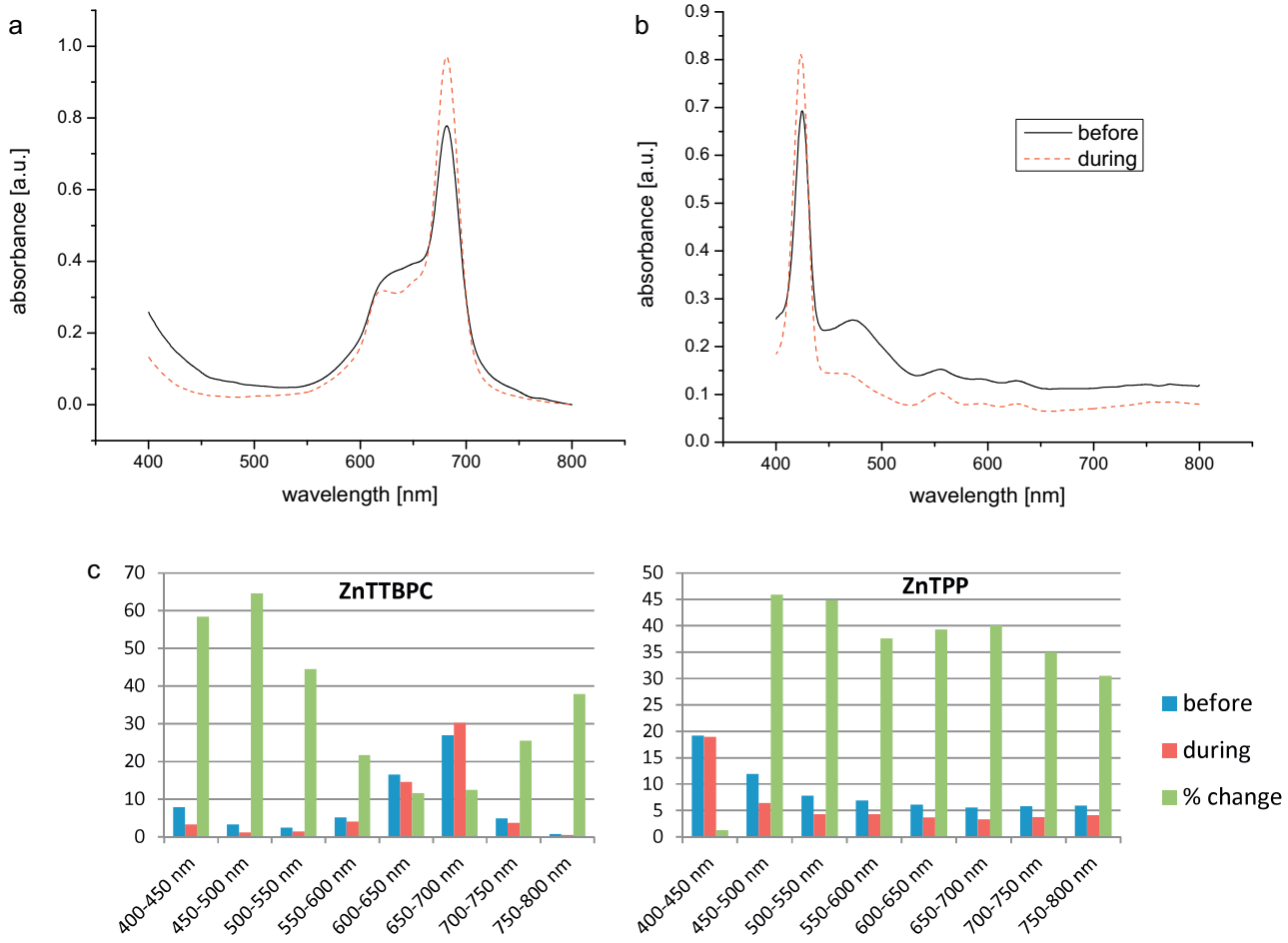

Fig. 5. (a) Spectra of ZnTTBPc-sol–gel film before and during exposure to ethanol vapor. (b) Spectra of ZnTPP-sol–gel film before and during exposure to isopropanol vapor. (c) Sensor responses of ZnTTBP and ZnTPP films in terms of changes of area integral values of the 8 wavelength intervals.

respectively. It can be seen that the spectra change quite significantly upon analyte exposure and absorbance at each wavelength is affected by the presence of analyte, albeit not to the same extent. Moreover, Fig. 5c shows the area integral values of in all wavelength ranges before and during analyte exposure. In Fig. 5c, the column % change denotes the relative response 'intensity'. It can be observed that the % change in various wavelength ranges shows a certain characteristic pattern for the analyte. When the same principle applies to other tested analytes, distinct patterns are obtained. The 'uniqueness' of the response pattern for each analyte differs from one sensing material to another. In some cases, response pattern in different wavelength ranges of a sensing material are too similar, making it unable to distinguish the analytes (cf. the pattern recognition results for Mn(III)ClTPP-containing sample, Fig. 7b).

The explanations for different sensing characteristics based on spectral changes of various dyes and their effects on array sensitivity may be explained based on results of computational methods and vibrational spectroscopy by several groups [28,30–32]. It was found that spectral alterations are mainly due to axial ligation of analyte molecules to the coordination sites of the central metal and subsequent donation (or withdrawal) of some of their charge to (or from) the macrocycle. Also, ligation of molecules leads to out-of-plane displacement of the central ion which in turn changes the molecular symmetry of the MePc/MeP molecules influencing energy states within the compound and thereby leading to spectral changes as well.

All of the employed sensing materials share a similar structure. They consist of a central metal ion, a chelating macrocycle and peripheral substituents. Analyte molecules may interact with all three structural subunits. Hence, varying the central metal ion affects the analyte binding affinity, and also strongly influences the energy states of the molecular orbitals, of the sensing materials. This leads to significant differences in sensing characteristics of MePc/MeP with differing central ions, and since MePc/MeP form complexes with almost all metals and some non-metals, it is possible to create a large variety of MePc/MeP based sensing materials. Moreover, altering the peripheral substituents may also lead to altered sensing behavior, either directly by interactions between substituent and analyte or indirectly by steric effects impairing interaction with the active sensing sites [13]. The spectral response in Fig. 5c confirms that most areas of spectral are affected by the anlyte and each sensing material exhibits unique response patterns, which can unambiguously be assigned to each analyte. Thus, the use of sensor array containing response different materials will enhance sensitivity of pattern recognition.

Optical sensing experiments have confirmed that the investigated MePc/MeP-containing sol–gel layers undergo spectral alterations when exposed to various organic compounds, namely methanol, ethanol, isopropanol and acetone. Fig. 6a and b shows, representatively, the response behavior of the investigated layers within several wavelength ranges when exposed to VOC at different concentrations. The extent of the spectral alteration (in terms of the change of the area integral value of the separate wavelength ranges) increases with rising concentrations. When the films are exposed to the analytes the integral values increase (or decrease) until an equilibrium of adsorption/desorption is established, i.e. a steady state is reached.

The influence of the number of printed layers, i.e. the film thickness, on the sensor performance was investigated. Fig. 6c shows the area integral (400–500 nm) of films containing ZnTPP with different thicknesses when exposed to methanol vapor (100×10^3 ppm, 700 sccm). It is clearly seen that the response increases with increasing the film thickness. Films consisting of two layers show very low optical absorbance and sensing responses due to small amount of dye molecules. As the number of layers increases to four, films show considerably higher responses, reaching a stable

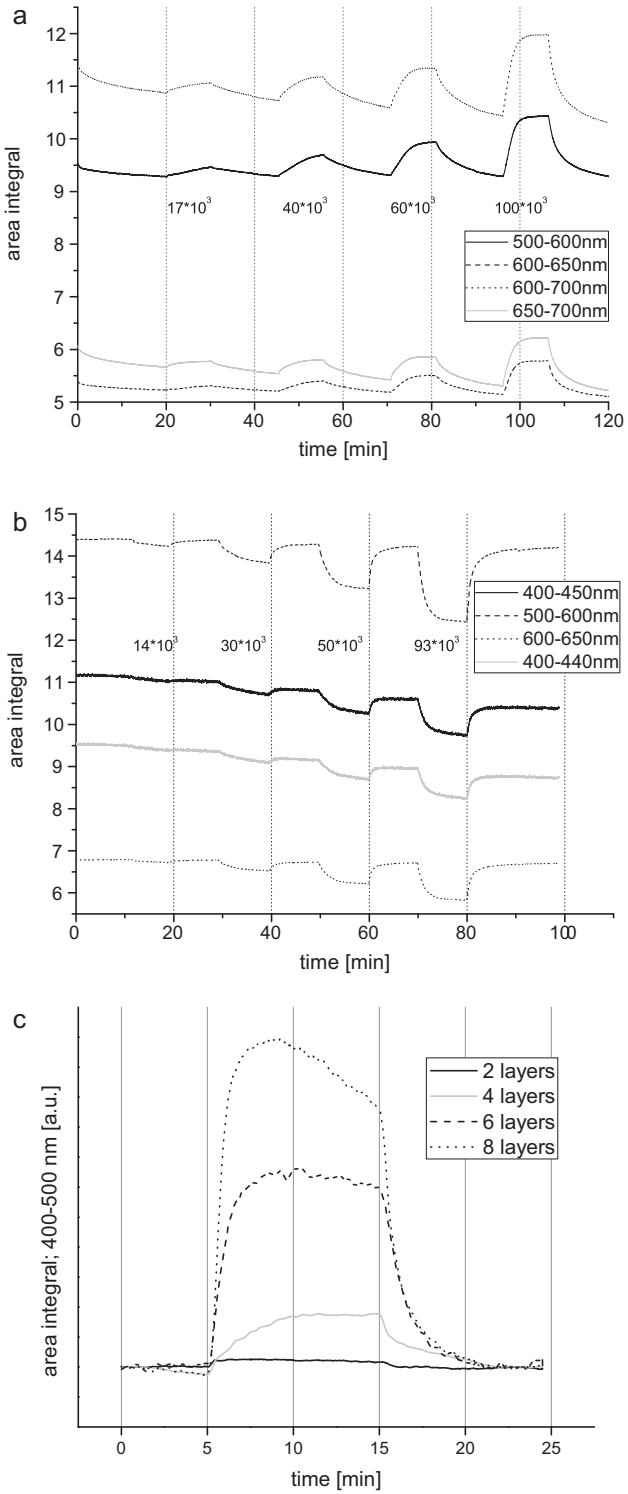

Fig. 6. (a) ZnTTBPc-containing layer; response toward ethanol. (b) ZnTPP-containing layer; response toward isopropanol. (c) Sensing responses toward methanol of ZnTPP containing films of varying thickness in terms of spectral area integral between 400 and 500 nm.

value after approximately 5 min upon exposure. Further increasing the number of layer to six, films exhibit about three times higher response than the one with four layers and a stable state is reached after about 3 min. Adding two more layers leads to even higher absorbance response, however, the initially high response deteriorates during exposure and a stable state is not reached even after 10 min. In addition, it can be noticed that all sensors have

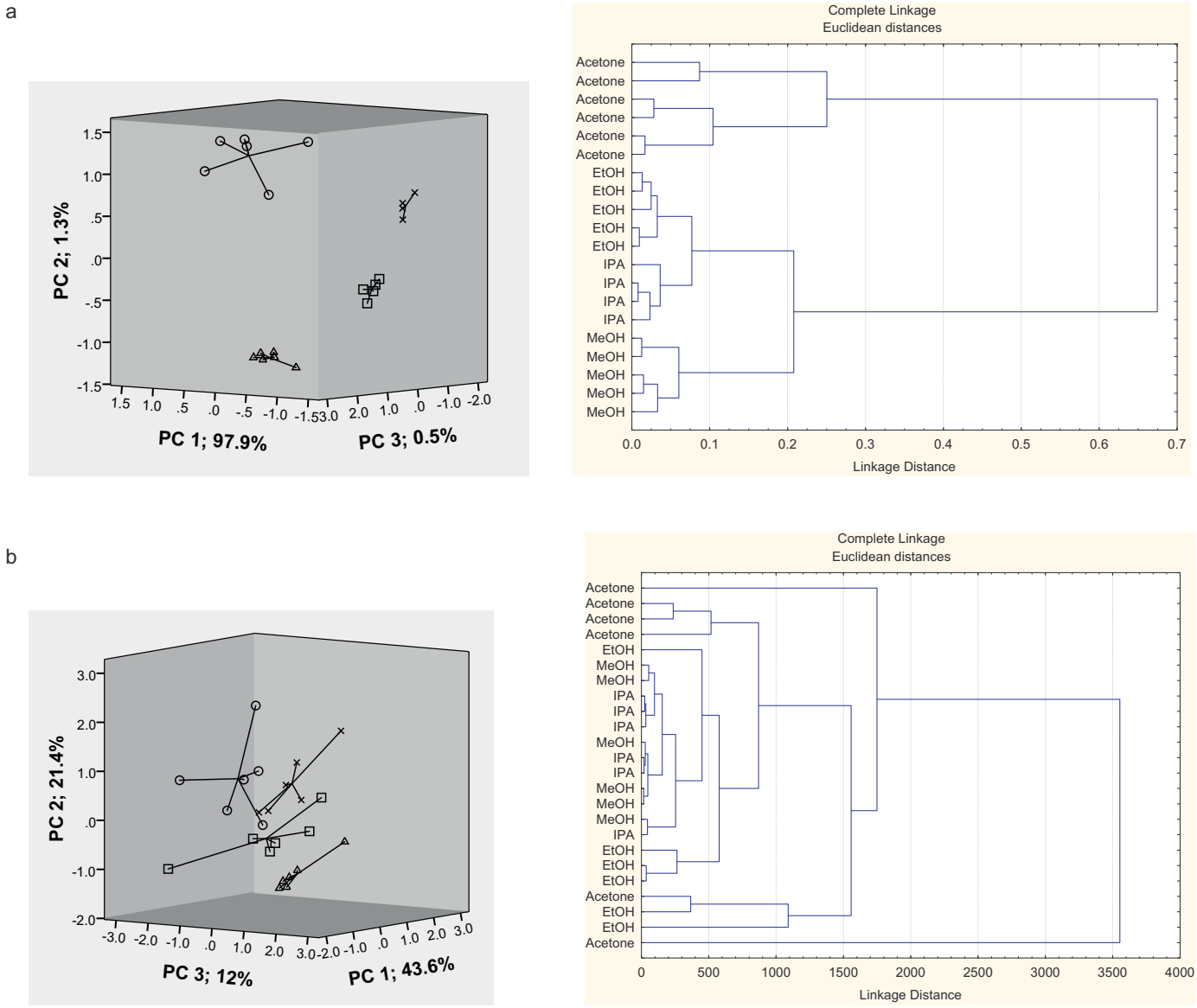

Fig. 7. Results of pattern analyses; left: PCA (◯ = acetone, × = isopropanol, △ = methanol, □ = ethanol); right: HCA. (a) Pattern analysis of a ZnTPP-containing sample. (b) Pattern analysis of a Mn(III)ClTPP-containing sample.

approximately the same recovery time of about 8 min. Thus, the optimal number of inkjet printed layers for this material is six because of the observed shortest response time and moderately high response value. It should be noted that similar results have been observed from other cases employing different dyes.

It can be observed from these results that the sensor sensitivity is on the order of tens of percents over high concentration range up to 10^5 ppm. The sensitivity of the sensor is rather low because the sensor operates at room temperature where physical adsorption dominates. Thus, the sensitivity and detection range are considerably poorer than metal oxide gas sensors operating at an elevated temperature. The applications for this type of sensor are therefore not the detection of trace amount of VOC vapor in breath or ambient but they will be used for high-concentration room-temperature sensing applications such as electronic nose. The observed sensitivity is adequate for this application and comparable to other works on metal phthalocyanine/porphyrin (MePc/MeP) based optical gas sensors for VOC sensing. For instance, VOC sensing properties of various porphyrins were studied in the concentrations ranging from as low as 3 ppm for octanol (vapor pressure of 10 kPa at 128.2 °C) up to 32,000 ppm for butanone (vapor pressure of 10 kPa at −18.1 °C) [7]. In another report, the VOC sensing performance of zinc phthalocyanine was reported in the concentrations ranging from 1500 ppm of ethanol (vapor pressure of 10 kPa at 29.2 °C) up to 170,000 ppm of isopropanol (vapor pressure of 10 kPa at 33.6 °C) [5].

3.3. Pattern analysis

PCA and CA were employed to assess the abilities of the sensing layers to distinguish between analytes, i.e. if exposure to analytes led to unique response patterns. PCA analysis yields plots that are immediately understandable just by looking at them and convey a stronger visual impression than dendrograms obtained from CA analysis. In addition, they contain information about the distribution of variance in the analyzed data set. In contrast, the CA dendrograms are able to show similarities between the analyte clusters more clearly. Both analyses made use of only the digital data gained in the previously described alternating gas flow experiments, without inclusion of any other information (other data, e.g.

temperature, humidity, etc., were kept constant and not included in the datasets.) Suslick et al. [23] showed that CA can be used as a powerful tool to find similarities in the data of various analytes and to group them accordingly. The resulting scatter plots (PCA) and dendrograms (HCA) of ZnTPP and Mn(III)ClTPP are shown in Fig. 7. It was found that sol–gel films containing ZnTPP (Fig. 7a) and MgTPP (not shown) yielded the best results in terms of discrimination between the analytes when analyzed by both PCA and CA as all analytes were clearly distinguishable from each other. As can be seen in the dendrogram (Fig. 7a), the 3 alcohols (methanol, ethanol and IPA) reside on one of the two main branches of the tree diagram, whereas acetone lies on the other main branch. In contrast, samples containing ZnTTBPc (not shown) and magnesium octaethyl porphyrin (not shown) were not able to distinguish all employed analytes. In the case of ZnTTBPc, acetone and methanol are hardly distinguishable in the resulting PCA plots. Furthermore, the HCA result suggests that the variations in the measured values for acetone, isopropanol and methanol are too insignificant in order to form distinguishable clusters. The results for magnesium octaethyl porphyrin containing specimen show that the measured values for methanol and ethanol formed a single cluster in the PCA plot as well as in the dendrogram. Besides, acetone and isopropanol form distinguishable clusters. The results obtained with the Mn(III)ClTPP containing samples (Fig. 7b) suggest that it is not possible to discriminate between the employed analytes with these layers. As can be observed in the PCA plot, the values lie close to one another making it difficult to assign them to separate clusters. Moreover, HCA supports this finding as it is clearly observable that it did not yield a single clearly separated cluster for any of the analytes.

4. Conclusion

Metal phthalocyanine- and metal porphyrin-containing sol–gel layers have been inkjet-printed. The so-obtained films were structurally characterized by various methods and used as sensing layers for optical gas sensing experiments. It was found that the fabricated layers exhibit reversible optical alterations in the UV/vis spectrum when exposed to various VOCs. These alterations were used to obtain data set that was analyzed by simple pattern analysis methods, namely PCA and HCA. The analyses yield data plots and dendrograms in which the values of the analytes clearly form distinguishable clusters.

It has to be noted, however, that not all the employed layers exhibit equal sensing capabilities. Best results are obtained from ZnTPP and MgTPP containing films, whereas layers doped with Mn(III)ClTPP do not exhibit good optical gas sensing behavior.

Acknowledgements

This work has been funded by the Director Initiative Program of NECTEC. Furthermore, Dr. Tuantranont greatly appreciates the career development grant from the Thailand Research Fund (TRF).

References

[1] G. Maggioni, S. Carturan, M. Tonezzer, A. Quaranta, G. Della Mea, Plasma-deposited copper phthalocyanine: a single gas-sensing material with multiple responses, Sensors and Actuators B: Chemical 131 (2008) 496–503.
[2] T.C. Pearce, S.S. Schiffman, H.T. Nagle, J.W. Gardner (Eds.), Handbook of Machine Olfaction: Electronic Nose Technology, Wiley-VCH, Weinheim, 2003.
[3] J. Spadavecchia, G. Ciccarella, P. Siciliano, S. Capone, R. Rella, Spin-coated thin films of metal porphyrin-phthalocyanine blend for an optochemical sensor of alcohol vapours, Sensors and Actuators B: Chemical 100 (2004) 88–93.
[4] G. Guillaud, J. Simon, J.P. Germain, Metallophthalocyanines gas sensors, resistors and field effect transistors, Coordination Chemistry Reviews 178 (1998) 1433–1484.
[5] M. Tonezzer, A. Quaranta, G. Maggioni, S. Carturan, G.D. Mea, Optical sensing responses of tetraphenyl porphyrins toward alcohol vapours: a comparison between vacuum evaporated and spin-coated thin films, Sensors and Actuators B: Chemical 122 (2007) 620–626.
[6] J. Spadavecchia, R. Rella, P. Siciliano, M.G. Manera, A. Alimelli, R. Paolesse, et al., Optochemical vapour detection using spin coated thin film of ZnTPP, Sensors and Actuators B: Chemical 115 (2006) 12–16.
[7] A.D.F. Dunbar, S. Brittle, T.H. Richardson, J. Hutchinson, C.A. Hunter, Detection of volatile organic compounds using porphyrin derivatives, The Journal of Physical Chemistry B 114 (2010) 11697–11702.
[8] M. Tonezzer, G. Maggioni, A. Quaranta, S. Carturan, G. Della Mea, Optical sensing properties of CoTPP thin films deposited by glow-discharge-induced sublimation, Sensors and Actuators B: Chemical 122 (2007) 613–619.
[9] J. Spadavecchia, G. Ciccarella, R. Rella, S. Capone, P. Siciliano, Metallophthalocyanines thin films in array configuration for electronic optical nose applications, Sensors and Actuators B: Chemical 96 (2003) 489–497.
[10] A. Ali Umar, M. Mat Salleh, M. Yahaya, Self-assembled monolayer of copper (II) meso-tetra (4-sulfanatophenyl) porphyrin as an optical gas sensor, Sensors and Actuators B: Chemical 101 (2004) 231–235.
[11] Y.L. Lee, C.Y. Hsiao, R.H. Hsiao, Annealing effects on the gas sensing properties of copper phthalocyanine films, Thin Solid Films 468 (2004) 280–284.
[12] O. Worsfold, C.M. Dooling, T.H. Richardson, M.O. Vysotsky, R. Tregonning, C.A. Hunter, et al., Nitrogen dioxide sensing characteristics at elevated temperature of sol–gel glass thin films containing substituted porphyrin dyes, Journal of Materials Chemistry 11 (2001) 399–403.
[13] D.W. Hatchett, M. Josowicz, Composites of intrinsically conducting polymers as sensing nanomaterials, Chemical Reviews 108 (2008) 746–769.
[14] S.J. Haswell (Ed.), Practical Guide to Chemometrics, Dekker, New York, 1992.
[15] I.T. Jolliffe, Principal Component Analysis, 2nd ed., Springer, New York, 2002.
[16] R. Brereton, Chemometrics, Wiley, Chichester, West Sussex, England, 2003.
[17] C.J. Brinker, G.W. Scherer, Sol–gel Science: The Physics and Chemistry of Sol–gel Processing, Academic Press Inc., San Diego, 1990.
[18] A. Lukowiak, W. Strek, Sensing abilities of materials prepared by sol–gel technology, Journal of Sol–Gel Science and Technology 50 (2009) 201–215.
[19] M. O'Toole, R. Shepherd, G.G. Wallace, D. Diamond, Inkjet printed LED based pH chemical sensor for gas sensing, Analytica Chimica Acta 652 (2009) 308–314.
[20] S.M. Hossain, R.E. Luckham, A.M. Smith, J.M. Lebert, L.M. Davies, R.H. Pelton, et al., Development of a bioactive paper sensor for detection of neurotoxins using piezoelectric inkjet printing of sol–gel-derived bioinks, Analytical Chemistry 81 (2009) 5474–5483.
[21] S. Di Risio, N. Yan, Piezoelectric ink-jet printing of horseradish peroxidase: effect of ink viscosity modifiers on activity, Macromolecular Rapid Communications 28 (2007) 1934–1940.
[22] J. Wang, P.V. Pamidi, D.S. Park, Screen-printable sol–gel enzyme-containing carbon inks, Analytical Chemistry 68 (1996) 2705–2708.
[23] C.J. Musto, S.H. Lim, K.S. Suslick, Colorimetric detection and identification of natural and artificial sweeteners, Analytical Chemistry 81 (2009) 6526–6533.
[25] Almeida, Pantano, Structural investigation of silica gel films by infrared spectroscopy, Journal of Applied Physics 68 (1990) 4225–4232.
[26] S. Sakka, Handbook of Sol–gel Science and Technology: Processing, Characterization and Applications, Kluwer Academic Publishers, New York, 2005.
[27] J. Estella, J.C. Echeverría, M. Laguna, J.J. Garrido, Silica xerogels of tailored porosity as support matrix for optical chemical sensors. Simultaneous effect of pH, ethanol: TEOS and water: TEOS molar ratios, and synthesis temperature on gelation time, and textural and structural properties, Journal of Non-Crystalline Solids 353 (2007) 286–294.
[28] S. Singh, S.K. Tripathi, G.S.S. Saini, Optical and infrared spectroscopic studies of chemical sensing by copper phthalocyanine thin films, Materials Chemistry and Physics 112 (2008) 793–797.
[29] M.-S. Liao, S. Scheiner, Electronic structure and bonding in metal phthalocyanines, Metal = Fe, Co, Ni, Cu, Zn, Mg, The Journal of Chemical Physics 114 (2001) 9780.
[30] S. Uttiya, Effect of structural transformation on the gas-sensing properties of phthalocyanine thin films, Journal of Korean Physical Society 52 (2008) 1575–1579.
[31] G.S.S. Saini, S. Singh, S. Kaur, R. Kumar, V. Sathe, S.K. Tripathi, Zinc phthalocyanine thin film and chemical analyte interaction studies by density functional theory and vibrational techniques, Journal of Physics: Condensed Matter 21 (2009) 225006.
[32] G. Saini, S. Dogra, G. Singh, Effects of chemical analytes on zinc tetraphenylporphine thin films studied by vibrational spectroscopy and density functional theory, Vibrational Spectroscopy 61 (2012) 188–198.

Biographies

Johannes Mensing received his engineering diploma (Dipl.-Ing.) in bio and nanotechnology engineering from the University of Applied Sciences Suedwestfalen in 2009. Since 2009, he is a PhD candidate in materials science and engineering at Faculty of Science, Mahidol University. He is doing research on newly developed, inkjet printable materials for chemical sensing applications.

Anurat Wisitsoraat received his PhD, MS degrees from Vanderbilt University, TN, USA, and BEng degree in electrical engineering from Chulalongkorn University, Bangkok, Thailand in 2002, 1997, and 1993, respectively. His research interests include microelectronic fabrication, semiconductor devices, electronic and optical thin film coating, sensors, and micro electromechanical systems (MEMS).

Adisorn Tuantranont received the BS degree in electrical engineering from King Mongkut's Institute of Technology Ladkrabang, Thailand, in 1995, and the MS and PhD degrees in electrical engineering from the University of Colorado at Boulder in 2001. Since 2001, he has been the director of the Nanoelectronics and MEMS Laboratory, National Electronic and Computer Technology Center (NECTEC), Pathumthani, Thailand. His research interests are in the area of micro electro-mechanical systems (MEMS), nanoelectronics, lab-on-a-chip technology and printed electronics.

Teerakiat Kerdcharoen received BSc and MSc in Chemistry from Chulalongkorn University in 1990 and 1992, respectively. As an Exchange Student, he received his PhD in Physical Chemistry from University of Innsbruck in 1995. Presently, he is a faculty member of Mahidol University. His research interests cover the topics of organic electronics ranging from theoretical modeling of materials to fabrication of devices such as tactile and chemical sensors.

Title: Cytotoxicity assessment of MDA-MB-231 breast cancer cells on screen-printed graphene - carbon paste substrate

Author: U. Waiwijit W. Kandhavivorn B. Oonkhanond T. Lomas D. Phokaratkul A. Wisitsoraat A. Tuantranont

PII: S0927-7765(13)00575-4
DOI: http://dx.doi.org/doi:10.1016/j.colsurfb.2013.09.008
Reference: COLSUB 6008

To appear in: *Colloids and Surfaces B: Biointerfaces*

Received date: 18-4-2013
Revised date: 2-8-2013
Accepted date: 3-9-2013

Please cite this article as: U. Waiwijit, T. Lomas, D. Phokaratkul, A. Wisitsoraat, A. Tuantranont, Cytotoxicity assessment of MDA-MB-231 breast cancer cells on screen-printed graphene - carbon paste substrate, *Colloids and Surfaces B: Biointerfaces* (2013), http://dx.doi.org/10.1016/j.colsurfb.2013.09.008

Cytotoxicity assessment of MDA-MB-231 breast cancer cells on screen-printed graphene - carbon paste substrate

U. Waiwijit[a], W.Kandhavivorn[b], B.Oonkhanond[b], T. Lomas[a], D. Phokaratkul[a], A. Wisitsoraat[a], A. Tuantranont[a*]

[a]Nanoelectronics and MEMS Laboratory, National Electronics and Computer Technology Center, 112 Thailand Science Park, Phahon Yothin Rd., Klong 1, Klong Luang, Pathumthani 12120, Thailand

[b]Department of Biomedical Engineering, Faculty of Engineering, Mahidol University, 25/25 Buddhamonthon Sai 4 Rd., Salaya, Nakorn Cahaisri, Nakorn Pathom 73170, Thailand

*Corresponding author. +66(0)25646900 Ext. 2111, adisorn.tuantranont@nectec.or.th

Abstract

Graphene is a novel carbon-based material widely studied in bio-electrochemical fields because of its high electrical conductivity and excellent electrocatalytic activity. However, its biological applications have been limited due to the lack of understanding of its compatibility with numerous biological entities. In this paper, cytoxicities of MDA-MB-231 breast cancer cells (MDA cells) on carbon paste (CP) and graphene - carbon paste (GCP) substrates are assessed. GCP was prepared by mixing graphene powder into carbon paste with different graphene contents. Cytotoxic effect was evaluated from cell viability, cell adhesion, ROS production and fluorescence staining studies. Cell viability on GCP substrate was found to initially increase as graphene content increases from 0 to 2.5 wt% but then decrease as the content increases further. In addition, the viability decreases with time for all substrates. Similarly, graphene concentration affected the number of adherent cells in the same manner as the cell viability. Likewise, reactive oxygen species (ROS) induced by carbon substrate increased with time and decreased with small graphene inclusion, confirming that low graphene content led to lower cytotoxicity. Moreover, confluence of MDA cells on substrate evaluated using Hoechst 33342 fluorescence staining was also found to be enhanced at low graphene concentration. Therefore, low-content graphene incorporation can effectively improve biocompatibility of carbon-based materials with MDA-MB-231 breast cancer cells, enabling potential applications such as electrochemical electrode for cell study.

Keywords: Cytotoxicity, graphene, carbon paste, electrochemical electrode, substrate

Introduction

Graphene, a few or single layer of carbon atoms tightly packed into a two-dimensional (2D) hexagonal honey-comb lattice, is highly attractive in many scientific areas due to its unique electrical, optical, thermal and mechanical properties. [1-4] In biological fields, graphene-based nanomaterials have been extensively studied for biomedical applications such as drug delivery system, tissue engineering, antibacterial material, electrochemical biosensor, field-effect transistor (FET) biosensor and fluorescence resonance energy transfer (FRET) biosensor. [5-12]

Biocompatibility is an essential requirement for nanomaterials to be employed in biological systems. It is thus important to investigate toxic effect of graphene and its derivatives on biological entities such as mammalian cells and animals. The biocompatibility study of nanomaterials may be divided into two categories. Firstly, toxicity assessment is conducted on cells or animals directly exposed to nanomaterials. There have been some such studies on carbon-based nanomaterials including graphene, carbon nanotubes (CNTs) and their derivatives, which demonstrate that they induce toxicity in cultured cells as well as animal models and toxicity level depends on the carbon concentration. In addition graphene oxide (GO) exhibits dose-dependent toxicity resulting in cell apoptosis and lung granuloma formation to human fibroblast cells and mice, respectively. [13, 14]

For specific applications such as tissue engineering, scaffold implantable devices and electrochemical cell studies, toxicity is evaluated for cells attached on nanomaterial substrate. For instance, it has been reported that chemical vapor deposited graphene substrate not only induces no apparent toxicity but also promotes differentiation of neural cells and stem cells cultured on it. [15-17] From another report, NIH-3T3 cells exhibit similar cell viabilities after 24-hr and 48-hr incubation on different substrate materials including glass, CNTs and graphene. [13] Electrochemical study of cells is another potential biological application of carbon-based nanomaterials especially graphene since graphene have been demonstrated to be highly sensitive for detection of various biochemical analytes such as alkaloid, drug and neurotransmitter. [18] However, there have been only few reports that utilize graphene-based electrochemical sensor for cell culture and cell analysis. Recently, graphene -

polyaniline hybrid paper has been employed for L-929 fibroblast cell study and demonstrated to exhibit excellent electrochemical performance and biocompatibility. [19]

In this work, we investigate cytotoxicity of MDA-MB-231 breast cancer cells on low-cost and disposable screen-printed graphene - carbon paste (GCP) substrates for electrochemical cell study applications. Cell viability, cell adhesion, reactive oxygen species (ROS) production and fluorescence staining are systematically studied on GCP materials with varying graphene concentrations.

Material and Methods

Preparation of GCP substrate

The preparation of GCP substrates are schematically depicted in Figure 1. Firstly, graphene was prepared by the electrolytic exfoliation method reported previously. [20] In brief, a constant potential of 8 V was applied between two graphite rods submerged in polystyrenesulfonic acid (PSS) electrolyte for 24 hours and electrolytically exfoliated graphene dispersion was subsequently precipitated by centrifugation at 1200 rpm. The graphene precipitate was washed successively in ethanol and deionized water to remove PSS. The remaining solid was dried in an oven at 100 °C for 30 minutes. Graphene powder was then mixed into carbon paste (Gwent group of companies, United Kingdom) with varying graphene concentrations (1, 2.5, 5 and 10 wt%). GCP was screen printed in a circular pattern with 6.35 mm diameter on polyvinyl chloride (PVC) substrate using precision semi-automatic screen printer (MK-MINI, Japan). The screen printed substrates were then dried in an oven at 60 °C for 24 hours.

Structural characterization

Detailed structure of graphene-carbon paste was characterized by transmission electron microscope (TEM) (JEOL model JEM-2010) run at 200 keV. TEM samples were prepared by drop coating of 10-times-diluted GCP on carbon/copper grid. The sample dilution was necessary to obtain sufficiently thin GCP coating on the grid. Surface morphology of GCP substrate was examined using scanning electron microscope (SEM) (Hitachi model S-4700) operated at 5 kV accelerating voltage and 10 mm working distance. Chemical bonding of carbon based materials was evaluated by Raman spectrometer (Nova spectra source model 633), which was calibrated using a standard silicon

substrate. Surface chemical composition of GCP substrate was determined by Auger electron spectroscope (EMSL model 680) analyzed at 5 kV accelerating voltage.

Cell culture

MDA-MB-231 breast cancer cells were obtained from scaffold in tissue engineering laboratory, faculty of engineering, Mahidol University. Cells were cultured in Dulbecco's modified Eagle's medium (DMEM, Sigma Aldrich, MO, USA) supplemented with 5% fetal calf serum (FCS, Gibco, CA, USA) and 0.1% gentamycin (Thai government pharmaceutical organization). Cells were maintained at 37 °C in a humidified 5% CO_2 air incubator for 3 days to achieve 80% cell confluence. Cells were then trypsinized with trypsin and resuspended in DMEM medium.

Cell viability measurement

Screen-printed GCP on PVC circular sheets with 6.25 mm in diameter were fitted at the bottom of wells in 96-well plate and 12,000 cells were then plated into each well as illustrated in Figure 1. Three well plates were incubated at 37 °C in 5% CO_2 incubator with varying times (24, 48 and 72 hours). Cell viability was determined by 3-(4,5-Dimethylthiazol-2-yl)-2,5-diphenyltetrazolium bromide (MTT) method. After cell culture on GCP substrate, the media were aspirated and replaced with MTT solution (100 µl, 5 mg/ml). Cells were then incubated for 4 hours at 37 °C in 5% CO_2 incubator. Next, the solution was discarded and cells were lysed with 100 µl of dimethylsulfoxide (DMSO) to obtain purple solution. Finally, the purple solution was removed to empty the wells for absorbance measurement. The percentage of cell viability was calculated from the following formula:

% viability = mean absorbance of sample/ mean absorbance of control x 100

where control was the cells cultured on polystyrene well plate. It should be noted that absorbance of each sample was corrected with background subtraction and the background was denoted as GCP or CP substrate with no cell.

Cell adhesion evaluation

GCP substrates were placed in 96-well plates and coated with 10 µg/ml fibronectin in phosphate buffer saline (PBS, pH 7.4). Fibronectin was then incubated at 4 °C overnight. Next, any remaining active protein binding site were blocked with 1% bovine serum albumin (BSA) in PBS and

incubated at room temperature (RT) for 30 minutes. Treated substrates were then washed 3 times with PBS. Next, 100 µl of cells suspension (20,000 cells) in DMEM with 2% fetal bovine serum (FBS) was added into each well. Three plates were incubated at 37 °C with varying times (3, 6 and 24 hours). Plates were washed again 5 times with PBS to remove unbound cells. Attached cells were treated by adding 50 µl of 96% ethanol and incubated at RT for 10 min. Cell were then stained with 50 µl of 0.1% crystal violet and incubated at RT for 30 minutes. Cells were washed with deionized (DI) water to remove excess stain. Finally, 50 µl of 0.2% Triton X in DI water was added to lyse cells and the absorbance of resulting solution was measured at 570 nm using microplate reader. It should also be noted that the absorbance at 570 nm was corrected with subtraction of background signal of blank GCP or CP substrate coated with 1% BSA. The cell adhesion was also evaluated on control and negative control. Control is the cell-culture on fibronectin coated polystyrene substrate while negative control is the cell culture on polystyrene substrate with no fibronectin.

ROS production determination

The intracellular ROS generation of cells was determined using 10 µM 2',7'-dichlorfl uorescein-diacetate (DCFH-DA) in serum-free DMEM. ROS production was studied on cells incubated on GCP substrates with three different times (3, 6 and 24 hours). Cells were washed with PBS, then dropped with 100 µl of DCFH-DA solution and incubated at 37 °C for 1 hr. Solution was aspirated and then washed again with PBS. Finally, 100 µl of PBS was added and fluorescence intensity at 525 nm was measured by fluorescence microplate reader using 485-nm excitation. The fluorescence intensity of tested substrate is compared with control, which is polystyrene substrate. The ROS measurements were also conducted for positive control, which is cell cultured in serum-free DMEM containing 50 µM of 30% H_2O_2 in and for background, which is just the cultured medium.

Fluorescence staining

After incubation on GCP substrates for 24 hours, cells were washed in PBS. Subsequently, attached cells were stained with 1 µM Hoechst 33342 in PBS for 5 min and then detected by fluorescence microscope. Hoechst 33342 is a cell-permeable DNA stain that emits blue fluorescence at 460-490 nm under ultraviolet excitation.

Results and discussion

Structural characterization

A typical TEM micrograph of GCP with 2.5% graphene concentration is shown in Figure 2. It illustrates a portion of a polygonal thin sheet, which appears to be coated with a thin layer of smooth material. The smooth layer is expected to be the polymeric binder of carbon paste. It should be noted that the carbon nanoparticles in carbon paste are rarely observed in the image due to the large dilution of carbon paste during sample preparation. High resolution TEM image (inset image in Figure 2) of an edge of the sheet demonstrates graphitic fringes, which confirm that the synthesized structure is multi-layer graphene with six to ten sp^2-bonded carbon layers. It should be noted that a graphitic sheet with ten or less sp^2-bonded carbon layers can be considered as graphene since it still exhibits two-dimensional properties.[21]

Figure 3 shows typical SEM micrographs of screen-printed CP and GCP electrodes with different graphene concentrations. It can be seen that screen-printed CP surface is nanoporous and contains only uniform nanoparticles with diameter of 20-30 nm while GCP comprises additional polygonal nanosheets with larger size (~350-400 nm in width and length) dispersed on the surface, proving graphene inclusion in the nanocomposite. In addition, the observed graphene density is in qualitative agreement with the prepared concentration. At the lowest graphene concentration (1 wt%), graphene sheets are well dispersed and mostly isolated on the surface as illustrated in Figure 3 (b). As the graphene content increases, graphene sheets begin to agglomerate into larger and longer cluster as seen in Figure 3 (c)-(e). The agglomeration among graphene sheets is well known to arise from strong van der Waals interactions between them. [18]

Figure 4 illustrates Raman spectra of CP and GCP with different graphene concentrations. It can be seen that all GCPs and CP exhibit G, D and 2D peaks at ~1574 cm^{-1}, ~1330 cm^{-1} and ~2648 cm^{-1}, respectively. The sharp G peak arises from strong in-plane vibration of sp^2 bonds present in graphene as well as carbon nanoparticles. CP exhibits relatively high and broad D peak but very low 2D peak, indicating that CP nanoparticle structure entails highly disordered sp^2 bonds with a low number of second-order zone-boundary defects. [22] On the other hand, GCP with low graphene concentrations (1-2.5 wt%) shows clearly pronounced 2D peak and relatively low D peak, signifying the incidence of isolated graphene sheets, which is in accordance with the SEM observation. Moreover, the 2D peak is relatively broad compared to the corresponding G peak, suggesting that the

structure comprises multi-layer graphene. [23] As the graphene concentration increases, it is evident that 2D peak is suppressed while D peak becomes eminent and the relative peak amplitudes for 2D and D peaks of GCP at the highest graphene concentration becomes similar to those of CP. The results together with SEM observations suggest that the behaviors of aggregated graphene will approach those of graphite particles as the size of agglomerated graphene increases.

Figure 5 (A) illustrates typical Auger electron spectrum of GCP with 2.5% graphene concentration and the inset table shows the corresponding elemental composition. The electrode surface comprises three elements including carbon (C), oxygen (O) and chlorine (Cl) with elemental compositions of 95.2%, 3.3% and 1.5%, respectively. Cl is found in all samples with similar concentration and can be attributed to the residue of the paste binder while C and O are mainly from carbon and graphene powders. It is seen that the graphene-carbon composite material has low oxygen content, indicating its high chemical quality. The oxygen contents of all electrode materials are demonstrated in Figure 5 (B). It can be seen that the oxygen concentration tends to decrease with increasing graphene content, which can be attributed to the fact that the oxygen content of graphene (also shown in the figure) is considerably lower than that of CP. Thus, graphene addition also improves the chemical properties of electrode surface.

Cell viability

Cell viability measured by MTT colorimetric assay on CP and GCP with four graphene concentrations (1, 2.5, 5, 10 wt%) incubated with three different times (24, 48 and 72 hours) are compared as shown in Figure 6. It should be noted that cell viability is calculated relative to the control, whose cell viability is normalized to 100%. For the case of 24-hr incubation, it is evident that cell viability considerably increases from 69% to 84% with 1 wt% graphene addition. As the graphene concentration increases to 2.5 wt%, the viability remains approximately the same. However, the cell viability notably decreases when the graphene concentration increases further and the viability of 10 wt% GCP becomes even lower than that of CP (0 wt% GCP). In contrast, the cell viability only slightly improves with 1 wt% graphene inclusion and further increase of graphene content leads to inferior cell viability in the cases of higher incubation times (48 and 72 hours). Moreover, it can be noticed that the viability decreases with increasing incubation time for all substrates and the decrease is more drastic as the time increases from 24 to 48 hours. Thus, cell viability of GCP substrate depends simultaneously on

graphene concentration and incubation time. For short incubation time (24 hours), low graphene concentrations of 1-2.5 wt% results in moderately improved cell viability while higher concentration adversely affects the viability. At higher incubation times, the viability is only slightly improved with small graphene addition and becomes deteriorated at higher graphene content.

The results are in accordance with some previous cell viability studies on carbon-based nanomaterials. For instance, NIH-3T3 fibroblast cells cultured on carbon-based nanomaterial substrates exhibit similarly decreased cell viabilities compared with those on glass substrate. [13] The mechanisms of cell death induced by carbon-nanomaterials may be attributed to two pathways, necrosis and apoptosis. The hallmark of necrosis is the cell membrane damage due to Lactate dehydrogenase (LDH) release while caspase activation signifies apoptosis. A significant LDH release has been observed from neural Phaeochromocytoma-derived cells (PC-12) after 24-hr exposure to graphene sheet at high concentration (100 µg/ml) while insignificant LDH releases occur at lower graphene concentrations (0.01-10 µg/ml). In addition, caspase-3 activity has found to increase with time indicating that graphene induces cell death through apoptosis pathway. [24] Moreover, rat lung epithelial cells (LE cells) incubated with 0.5-10 µg/ml of MWCNTs have shown a dose- and time-dependent increase in formation of free radicals, accumulation of peroxidative products, antioxidant depletion and loss of cell viability. It has also been demonstrated that MWCNTs induces oxidative stress and stimulates apoptosis signaling pathway through caspase activation.[25]

Cell adhesion

Cells adhesion on a nanomaterial substrate is directly related to cellular response and biocompatibility of the nanomaterial. The interaction between cell and substrate often contributes to cell proliferation and differentiation. The adhesion can be quantitatively determined by colorimetric method, in which adherent cells absorb crystal violet dye and are lysed by Triton-X for absorbance detection. The absorbance, which is proportional to the number of adherent cells on control, CP and GCP substrates incubated for 3, 6, 24 hours are demonstrated in Figure 7. It is seen that the number of adherent cells becomes notably improved with small graphene concentration (1 wt%) but the improvement become relatively less when graphene content increases further. Similar trend is obtained for other incubation times. In addition, the number of cells attached on all GCP substrates is maximized at the same incubation time of 6 hrs. Thus, the presence of graphene nanosheets leads to

the improvement of cell adhesion. Furthermore, the cell adhesion of all CP and GCP substrates are poorer than that of control, asserting some toxicity induced by these substrate materials. Moreover, the cell adhesion of control is 2.5-5 times higher than that of negative control, confirming the effectiveness of fibronectin's adhesive property. This is in agreement with another report, in which the numbers of adherent NIH-3T3 fibroblast cells on graphene and carbon nanotube layers are improved compared with that of bare glass substrate. [17] Generally, cells attach tightly on grown substrate through distinct regions of their plasma membrane called focal adhesions. [26] At the focal adhesion site, cells contact the extracellular matrix (ECM) via transmembrane receptor called integrin. Cell detachment and associated cell death can occur through intracellular signaling pathways of these receptor complexes. [27]

ROS production

The intracellular ROS generation is a commonly proposed toxicological mechanism of nanoparticles. ROS are chemically reactive molecules containing oxygen, which form as a natural byproduct of the normal oxygen metabolism and play important roles in cell homeostasis. [28] In general, ROS are mainly produced inside organelles such as mitochondria, and released towards cytosol. [29] Excessive ROS causes alteration in intracellular redox state and oxidative modifications of proteins, leading to cell death. ROS production can be investigated via enzymatic reaction with 2',7'-dichlorfluorescein-diacetate (DCFH-DA). DCFH-DA, a nonpolar dye, is converted into the non-fluorescent polar derivative DCFH by cellular esterase and DCFH will be then switched to highly fluorescent DCF when oxidized by intracellular ROS and other peroxides. [30] The fluorescent intensity, corresponding to ROS production on control, CP and GCP substrates incubated for 3, 6, 24 hours are illustrated in Figure 8. It is seen that cells cultured on GCP substrates with low graphene concentrations (1-2.5 wt%) produce less ROS than those on CP while higher graphene concentration (5-10 wt%) leads to increased ROS production especially at long incubation time (24 hours). In addition, MDA cells cultured on all substrates exhibit steadily increased ROS production with increasing incubation time. Moreover, CP and GCP substrates induce cells to generate more ROS than the control, confirming that CP and GCP induce toxicity. Furthermore, measured ROS of control is 6-8 time lower than that of positive control, confirming the effectiveness of DCFH-DA activity. ROS production leads to oxidative stress that induces toxicity to cells and disruptions of normal

mechanisms of cellular signaling. It has been reported that GO induces oxidative stress in A549 cells even at low concentrations and higher GO concentrations stimulate ROS production progressively. [31] In addition, aggregated graphene causes mild lung injury and graphene dispersal in a biocompatible block copolymer can mitigate the toxicity while GO leads to severe lung injury characterized by diffuse alveolar damage and pulmonary fibrosis. Furthermore, PC12 cells generate more ROS with increasing graphene concentration from 0.01 to 100 μg/ml and increasing exposure time from 1 to 24 hrs. [24] Moreover, it has been demonstrated that aggregated graphene and graphene oxide, not dispersed ones, induce more ROS generation and cell death in lung epithelial cells. [32] However, the mechanisms of the increased ROS generation of cells on aggregated graphene and graphene oxide are not yet understood. Likewise, rat lung epithelial cells (LE cells) show increased ROS upon exposure to SWCNTs depending on dose and time, which leads to cells death. Additionally, the increased ROS production is found not to be attributed to change in mitochondria but rather due to decrease in glutathione and superoxide dismutase (SOD-1 and SOD-2), which are non-enzymatic and enzymatic antioxidant mechanisms, respectively. [33]

We propose a possible explanation for the observed graphene concentration dependence of GCP's cytotoxicity as followed. At low graphene concentration, graphene is well dispersed in and on carbon nanoparticles. The presence of dispersed graphene reduces toxicity to cell because isolated graphene has weak interaction with cell, leading to low toxicity. At higher graphene concentration, graphene tends to aggregate within the graphitic nanoparticle matrix. The aggregated graphene have properties and behaviors similar to graphitic particles that strongly interact with cell, stimulating cellular signaling to increase ROS generation, leading to poor cell attachment and cell death. Moreover, the lower toxicity by graphene may partly be attributed to the lower oxygen content of graphene surface observed from Auger electron spectra.

Fluorescence staining

DNA fluorescence staining has been used to qualitatively evaluate live cells on nanomaterial substrate. The Hoechst 33342 blue fluorescence staining dyes are cell permeable and can only bind to DNA in live cells. The fluorescence images of MDA cells adhered and grown on CP and GCP substrates for 24 hours are shown in Figure 9. It is seen that the layer of MDA cells on GCP with low concentrations (1-2.5 wt%) is more confluent than that on CP and GCP with higher graphene

283 contents. The results confirm that GCP substrate with low graphene concentration (1-2.5 wt%) has
284 relatively low cytotoxicity and high biocompatibility suitable for cell culture. The results are in
285 accordance with previous study on fluorescence staining of human osteoblasts and mesenchymal
286 stroma cells on graphene substrate, in which graphene is demonstrated to be suitable substrate for
287 cell growth because of more confluent layer formation and higher cell proliferation compared to SiO_2
288 substrate. [17]

289 **Conclusions**

290 In conclusion, GCP substrate induces incubation-time-dependent and graphene-
291 concentration-dependent cytotoxic effects on MDA breast cancer cells. Cell viability, cell adhesion
292 and ROS production are found to improve with GCP substrate containing graphene at low
293 concentration (1-2.5 wt%). In contrast, higher graphene concentration leads to increased toxicity and
294 poorer cell growth. In addition, low graphene concentration also leads to lower ROS production and
295 oxidative stress on the cultured cells on GCP substrate. Therefore, GCP substrate with low graphene
296 content offers relatively high biocompatibility compared to CP substrate and can potentially be used
297 as electrochemical electrode for cell analysis.

298 **Acknowledgements**

299 This work was financially supported by National Electronic and Computer Technology Center, a
300 member of National Science and Technology Development Agency (NSTDA), Thailand. A.
301 Tuantranont would like to express his gratitude for Researcher Career Development Grant from
302 Thailand Research Fund (TRF).

303 **Reference**

304 [1] P. Avouris, Z. Chen, V. Perebeinos, Carbon-based electronics, Nat Nanotechnol 2 (2007)
305 605-615.
306 [2] R.R. Nair, P. Blake, A.N. Grigorenko, K.S. Novoselov, T.J. Booth, T. Stauber, N.M.R. Peres,
307 A.K. Geim, Fine structure constant defines visual transparency of graphene, Science 320 (2008)
308 1308-1308.
309 [3] C. Lee, X.D. Wei, J.W. Kysar, J. Hone, Measurement of the elastic properties and intrinsic
310 strength of monolayer graphene, Science 321 (2008) 385-388.

311 [4] S.S. Chen, Q.Z. Wu, C. Mishra, J.Y. Kang, H.J. Zhang, K.J. Cho, W.W. Cai, A.A. Balandin,
312 R.S. Ruoff, Thermal conductivity of isotopically modified graphene, Nature Materials 11 (2012) 203-
313 207.
314 [5] S.B. Liu, T.H. Zeng, M. Hofmann, E. Burcombe, J. Wei, R.R. Jiang, J. Kong, Y. Chen,
315 Antibacterial Activity of Graphite, Graphite Oxide, Graphene Oxide, and Reduced Graphene Oxide:
316 Membrane and Oxidative Stress, ACS Nano 5 (2011) 6971-6980.
317 [6] Y. Wang, W.C. Lee, K.K. Manga, P.K. Ang, J. Lu, Y.P. Liu, C.T. Lim, K.P. Loh, Fluorinated
318 Graphene for Promoting Neuro-Induction of Stem Cells, Advanced Materials 24 (2012) 4285-4290.
319 [7] H.X. Chang, L.H. Tang, Y. Wang, J.H. Jiang, J.H. Li, Graphene Fluorescence Resonance
320 Energy Transfer Aptasensor for the Thrombin Detection, Analytical Chemistry 82 (2010) 2341-2346.
321 [8] W.B. Hu, C. Peng, W.J. Luo, M. Lv, X.M. Li, D. Li, Q. Huang, C.H. Fan, Graphene-Based
322 Antibacterial Paper, ACS Nano 4 (2010) 4317-4323.
323 [9] Y. Ohno, K. Maehashi, K. Matsumoto, Label-Free Biosensors Based on Aptamer-Modified
324 Graphene Field-Effect Transistors, Journal of the American Chemical Society 132 (2010) 18012-
325 18013.
326 [10] Z. Liu, J.T. Robinson, X. Sun, H. Dai, PEGylated Nanographene Oxide for Delivery of Water-
327 Insoluble Cancer Drugs, Journal of the American Chemical Society 130 (2008) 10876-10877.
328 [11] L. Tang, Y. Wang, Y. Li, H. Feng, J. Lu, J. Li, Preparation, Structure, and Electrochemical
329 Properties of Reduced Graphene Sheet Films, Advanced Functional Materials 19 (2009) 2782-2789.
330 [12] Q.O. Zeng, J.S. Cheng, L.H. Tang, X.F. Liu, Y.Z. Liu, J.H. Li, J.H. Jiang, Self-Assembled
331 Graphene-Enzyme Hierarchical Nanostructures for Electrochemical Biosensing, Advanced Functional
332 Materials 20 (2010) 3366-3372.
333 [13] S.R. Ryoo, Y.K. Kim, M.H. Kim, D.H. Min, Behaviors of NIH-3T3 Fibroblasts on
334 Graphene/Carbon Nanotubes: Proliferation, Focal Adhesion, and Gene Transfection Studies, ACS
335 Nano 4 (2010) 6587-6598.
336 [14] K. Wang, J. Ruan, H. Song, J.L. Zhang, Y. Wo, S.W. Guo, D.X. Cui, Biocompatibility of
337 Graphene Oxide, Nanoscale Research Letters 6 (2011).
338 [15] H.L. Fan, L.L. Wang, K.K. Zhao, N. Li, Z.J. Shi, Z.G. Ge, Z.X. Jin, Fabrication, Mechanical
339 Properties, and Biocompatibility of Graphene-Reinforced Chitosan Composites, Biomacromolecules
340 11 (2010) 2345-2351.

[16] T.R. Nayak, H. Andersen, V.S. Makam, C. Khaw, S. Bae, X.F. Xu, P.L.R. Ee, J.H. Ahn, B.H. Hong, G. Pastorin, B. Ozyilmaz, Graphene for Controlled and Accelerated Osteogenic Differentiation of Human Mesenchymal Stem Cells, ACS Nano 5 (2011) 4670-4678.

[17] M. Kalbacova, A. Broz, J. Kong, M. Kalbac, Graphene substrates promote adherence of human osteoblasts and mesenchymal stromal cells, Carbon 48 (2010) 4323-4329.

[18] R. Hanna, R. Jerzy, G. Iwona, K.t. Katarzyna, Electrochemical Sensors and Biosensors Based on Self-Assembled Monolayers: Application of Nanoparticles for Analytical Signals Amplification, Functional Nanoparticles for Bioanalysis, Nanomedicine, and Bioelectronic Devices Volume 1 1112 (2012) 293-312.

[19] X.B. Yan, J.T. Chen, J. Yang, Q.J. Xue, P. Miele, Fabrication of Free-Standing, Electrochemically Active, and Biocompatible Graphene Oxide-Polyaniline and Graphene-Polyaniline Hybrid Papers, ACS Applied Materials & Interfaces 2 (2010) 2521-2529.

[20] C. Sriprachuabwong, C. Karuwan, A. Wisitsorrat, D. Phokharatkul, T. Lomas, P. Sritongkham, A. Tuantranont, Inkjet-printed graphene-PEDOT:PSS modified screen printed carbon electrode for biochemical sensing, Journal of Materials Chemistry 22 5478-5485.

[21] A.W. Robertson, J.H. Warner, Atomic resolution imaging of graphene by transmission electron microscopy, Nanoscale 5 4079-4093.

[22] Z.H. Ni, Y.Y. Wang, T. Yu, Z.X. Shen, Raman Spectroscopy and Imaging of Graphene, Nano Research 1 (2008) 273-291.

[23] A. Ferrari, J. Robertson, Interpretation of Raman spectra of disordered and amorphous carbon, Physical Review B 61 (2000) 14095-14107.

[24] Y.B. Zhang, S.F. Ali, E. Dervishi, Y. Xu, Z.R. Li, D. Casciano, A.S. Biris, Cytotoxicity Effects of Graphene and Single-Wall Carbon Nanotubes in Neural Phaeochromocytoma-Derived PC12 Cells, ACS Nano 4 (2010) 3181-3186.

[25] P. Ravichandran, A. Periyakaruppan, B. Sadanandan, V. Ramesh, J.C. Hall, O. Jejelowo, G.T. Ramesh, Induction of apoptosis in rat lung epithelial cells by multiwalled carbon nanotubes, Journal of Biochemical and Molecular Toxicology 23 (2009) 333-344.

[26] K. Burridge, K. Fath, T. Kelly, G. Nuckolls, C. Turner, Focal adhesions: transmembrane junctions between the extracellular matrix and the cytoskeleton, Annu Rev Cell Biol 4 (1988) 487-525.

[27] A. Howe, A.E. Aplin, S.K. Alahari, R.L. Juliano, Integrin signaling and cell growth control, Current Opinion in Cell Biology 10 (1998) 220-231.

[28] T.P. Devasagayam, J.C. Tilak, K.K. Boloor, K.S. Sane, S.S. Ghaskadbi, R.D. Lele, Free radicals and antioxidants in human health: current status and future prospects, J Assoc Physicians India 52 (2004) 794-804.

[29] D. Han, E. Williams, E. Cadenas, Mitochondrial respiratory chain-dependent generation of superoxide anion and its release into the intermembrane space, Biochem J 353 (2001) 411-416.

[30] R.P. Rastogi, S.P. Singh, D.P. Hader, R.P. Sinha, Detection of reactive oxygen species (ROS) by the oxidant-sensing probe 2 ',7 '-dichlorodihydrofluorescein diacetate in the cyanobacterium Anabaena variabilis PCC 7937, Biochemical and Biophysical Research Communications 397 (2010) 603-607.

[31] Y.L. Chang, S.T. Yang, J.H. Liu, E. Dong, Y.W. Wang, A.N. Cao, Y.F. Liu, H.F. Wang, In vitro toxicity evaluation of graphene oxide on A549 cells, Toxicology Letters 200 (2011) 201-210.

[32] M.C.D. G R S. Budinger, Daniela Urich, Saul Soberanes, Sergio E. Chiarella, Angel Gonzalez, Kathryn A. Radigan, Navdeep S. Chandel, Mark C. Hersam, and Gokhan M. Mutlu, Graphene Oxide But Not Graphene Causes Severe Acute Lung Injury And Pulmonary Fibrosis In Mice, Am. J. Respir. Crit. Care Med. 183 A2283.

[33] C.S. Sharma, S. Sarkar, A. Periyakaruppan, J. Barr, K. Wise, R. Thomas, B.L. Wilson, G.T. Ramesh, Single-walled carbon nanotubes induces oxidative stress in rat lung epithelial cells, J Nanosci Nanotechnol 7 (2007) 2466-2472.

Figure 1. Schematic of the GCP substrate fabrication process and the experimental set up for cell culture.

Figure 2. Typical TEM micrograph of GCP with 2.5% graphene concentration. Inset: High resolution TEM image of an edge of the sheet demonstrating graphitic fringes.

Figure 3. Typical SEM images of screen-printed (a) CP electrodes (b) GCP with 1 wt% graphene concentration, (c) GCP with 2.5 wt% graphene concentration, (d) GCP with 5 wt% graphene concentration and (e) GCP with 10 wt% graphene concentration.

Figure 4. Typical Raman spectra of GCP with 1, 2.5, 5, 10 wt% graphene concentration and CP materials.

Figure 5. (a) Auger electron spectrum of GCP with 2.5% graphene concentration. Inset: the corresponding elemental composition table and (b) Graph of oxygen contents of all electrode materials.

Figure 6. MTT-assays cell viabilities of MDA cells cultured on CP and GCP substrate for 24, 48 and 72 hrs. Data are expressed as mean $\pm$ SD (n=6) of duplicate in three independent experiments.

Figure 7. Cell adhesion assays of MDA cells cultured on control, CP and GCP substrate for 24, 48 and 72 hrs. Data are shown as mean $\pm$ SD (n=6) of duplicate in three independent experiments.

Figure 8. ROS production from MDA cells on control, CP and GCP substrate for 3, 6 and 24 hrs. Data are expressed as mean $\pm$ SD (n=6) of duplicate in three independent experiments.

Figure 9. The Hoechst 33342 fluorescence staining nuclei of MDA cells on CP and GCP substrate for 24 hrs. (Scale bar 50 μm)

410 Highlights

411 We investigate cytotoxicity of screen-printed graphene - carbon paste (GCP) material towards MDA-
412 MB-231 breast cancer cell.

413 We will apply the screen-printed graphene - carbon paste as electrode for cell study by
414 electrochemical sensors.

415 The screen print technique is simply for preparation graphene-based electrodes which low-cost and
416 disposable electrode.

417

418

*Graphical Abstract (for review)

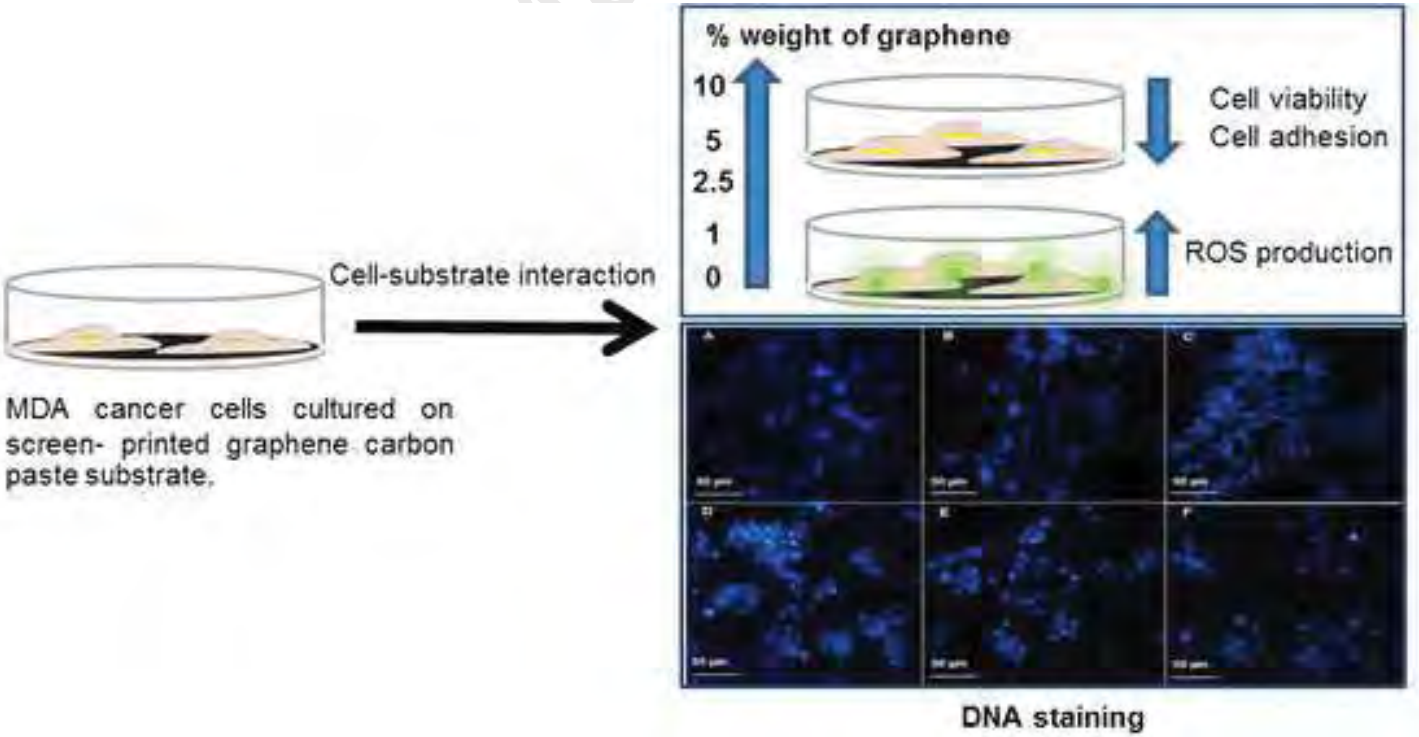

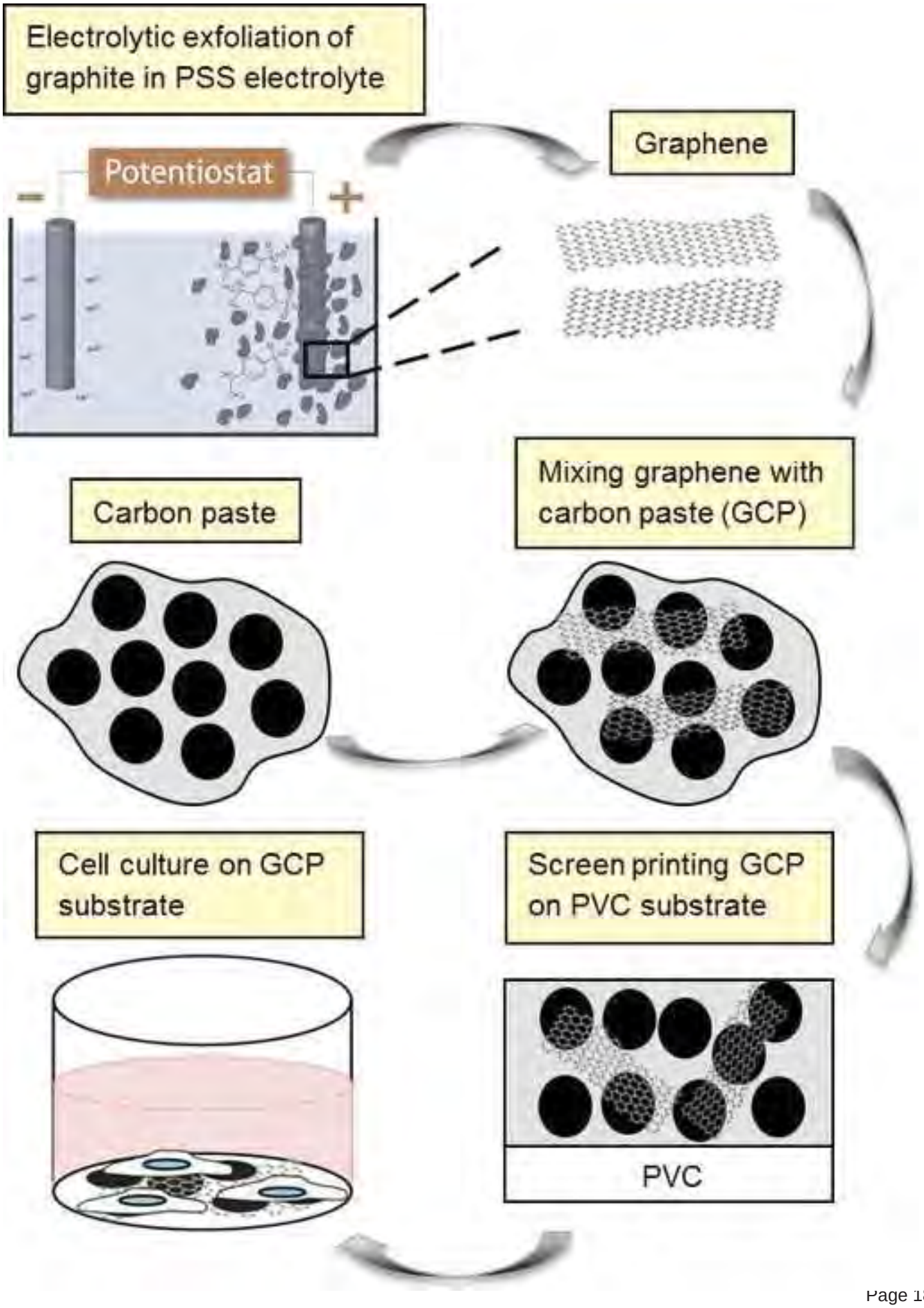

Figure(s)

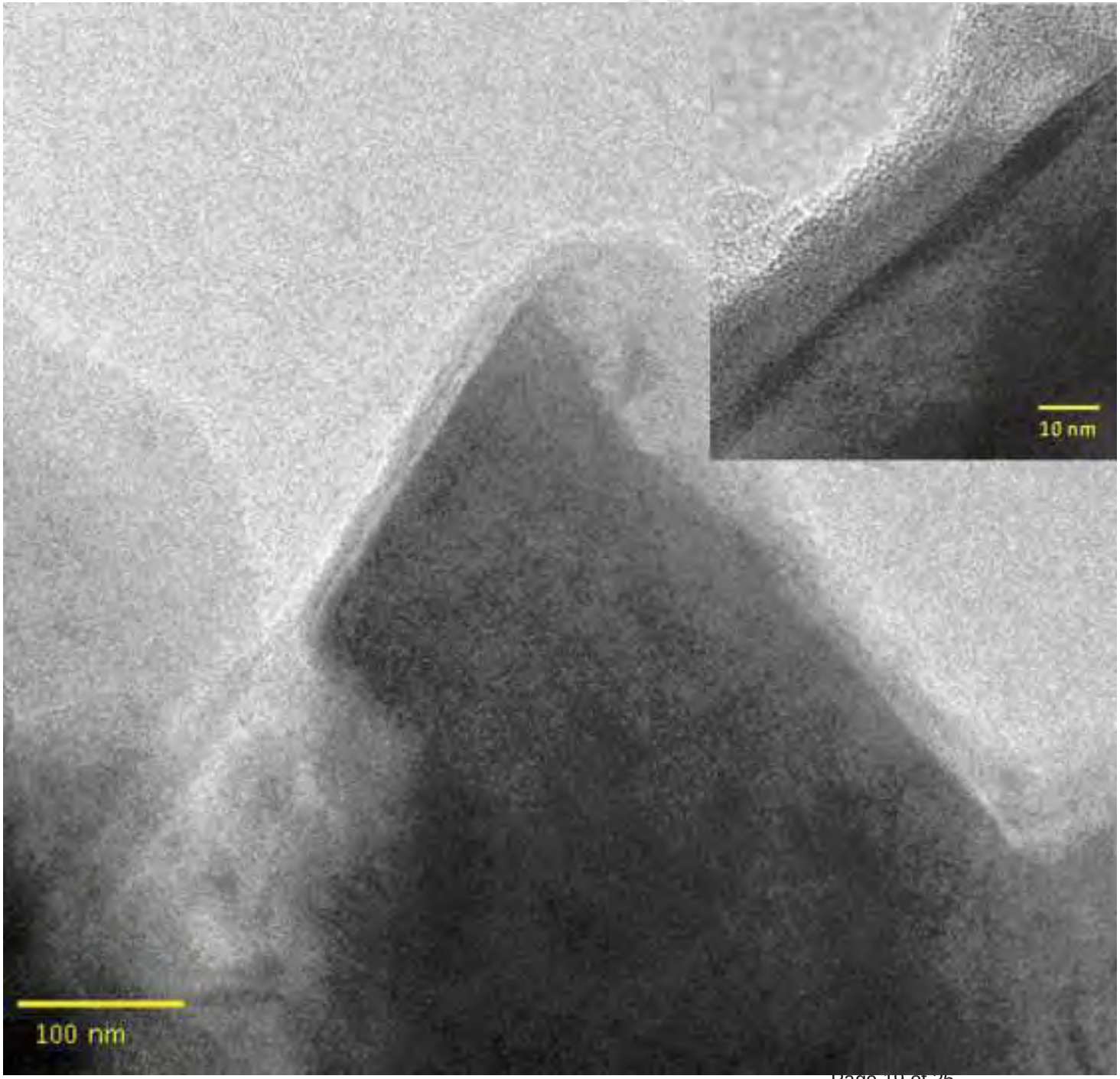

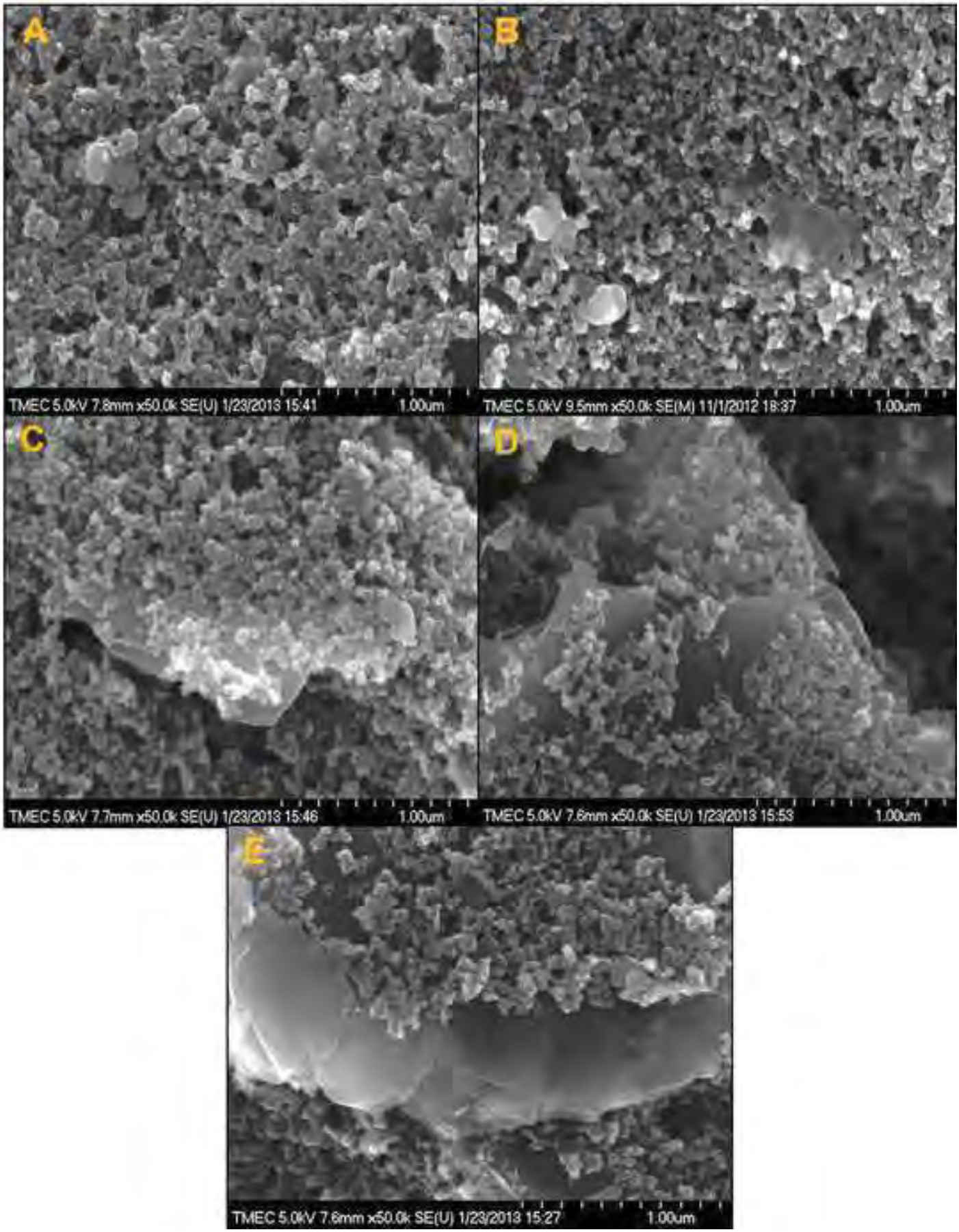

Figure(s)

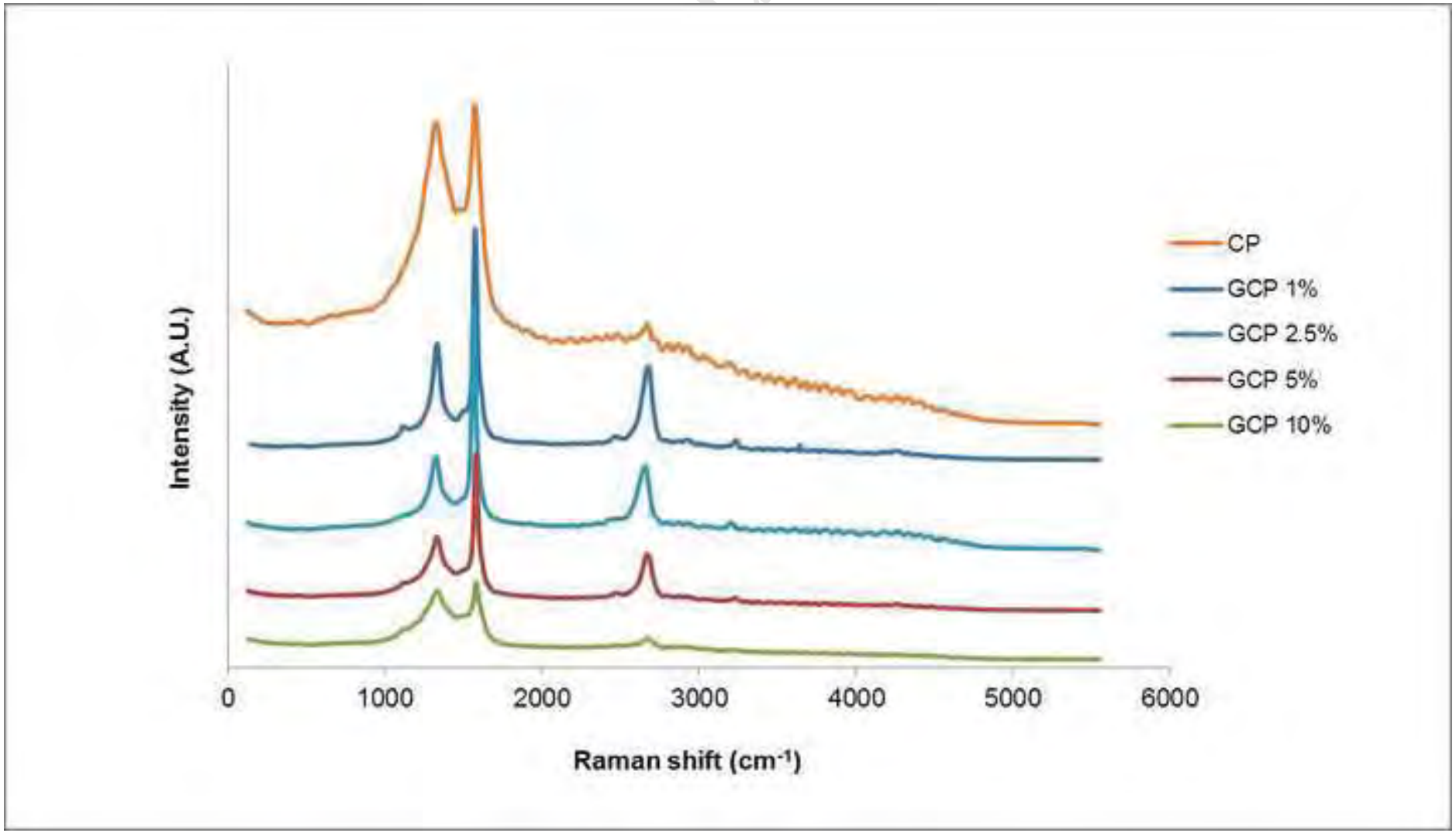
Intensity (A.U.)
0
1000
2000
3000
4000
5000
6000
Raman shift (cm-1)
CP
GCP 1%
GCP 2.5%
GCP 5%
GCP 10%

Figure(s)

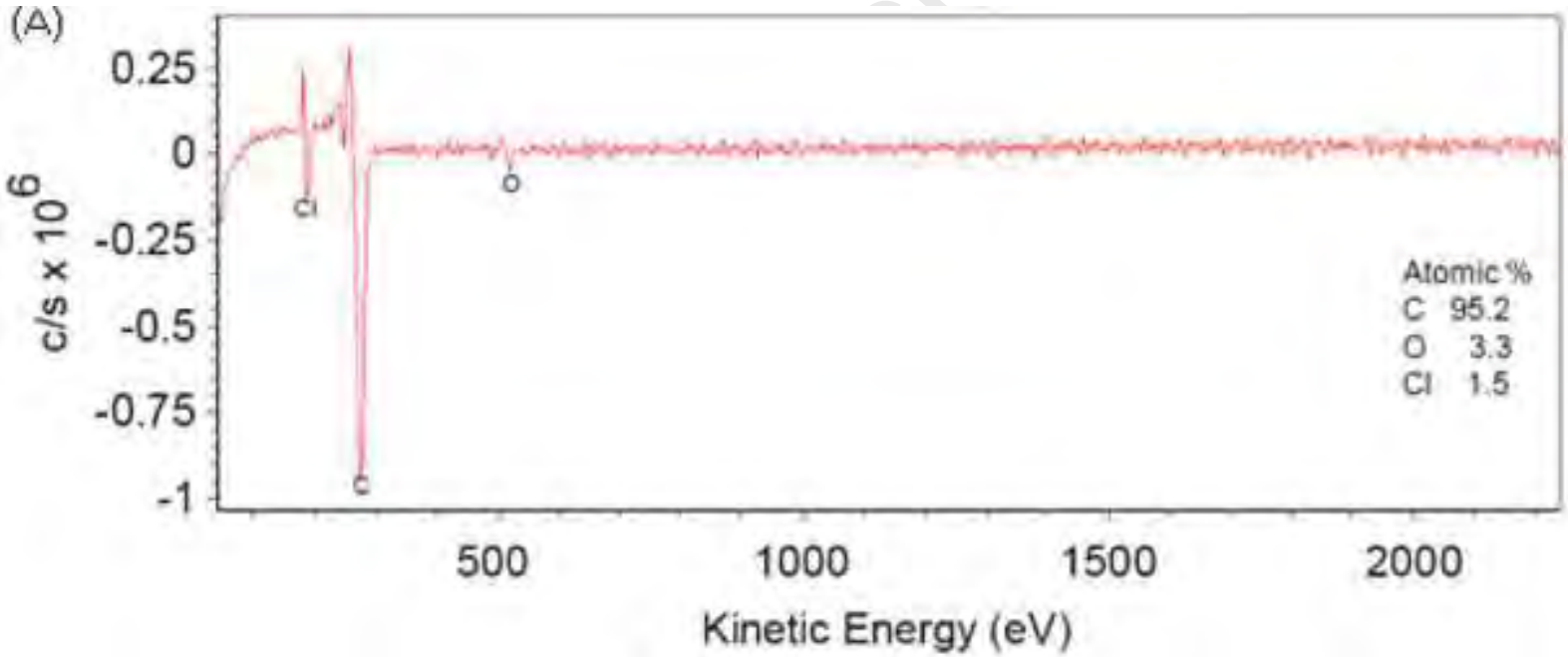
(A)
0.25
0
-0.25
-0.5
-0.75
-1
c/s x 10^6
Cl
O
C
Atomic %
C 95.2
O 3.3
Cl 1.5
500
1000
1500
2000
Kinetic Energy (eV)

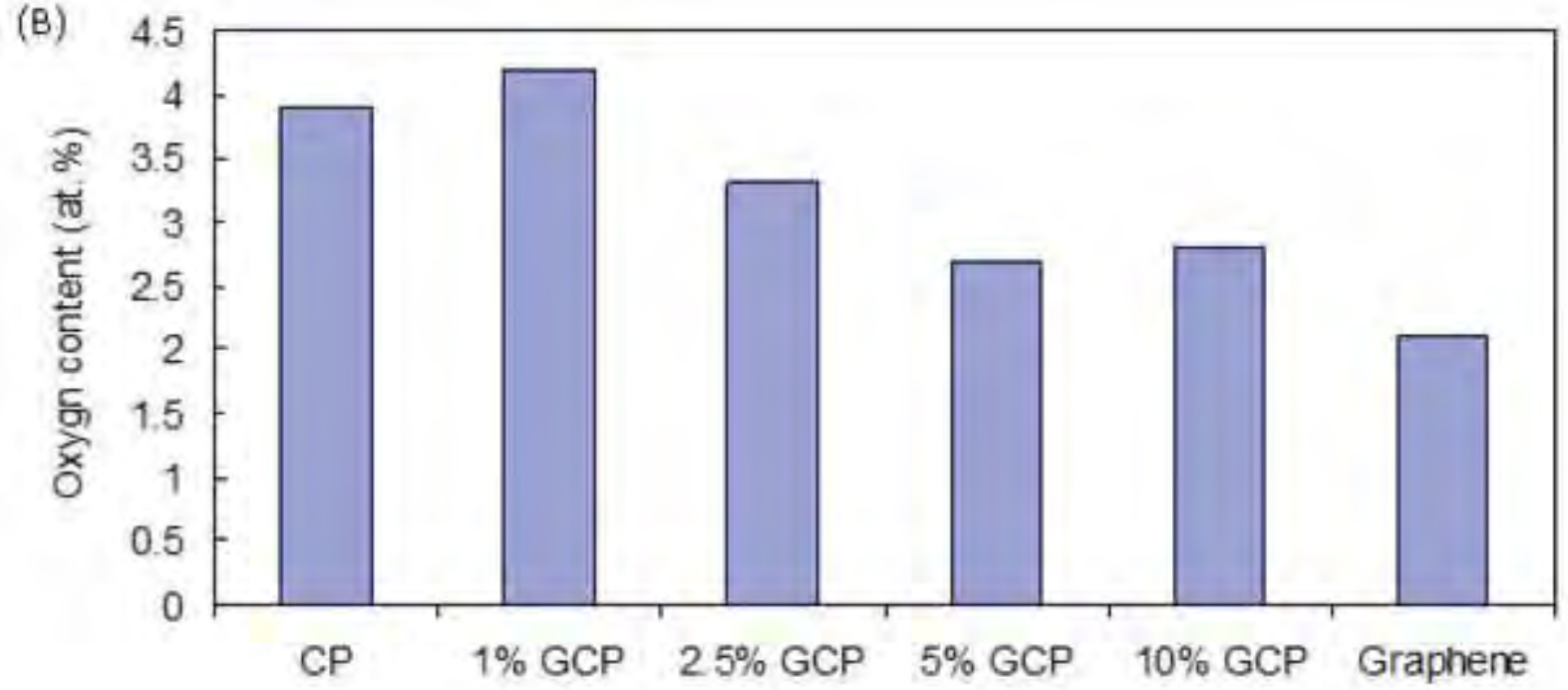
(B)
4.5
4
3.5
3
2.5
2
1.5
1
0.5
0
Oxygn content (at.%)
CP
1% GCP
2.5% GCP
5% GCP
10% GCP
Graphene

Figure(s)

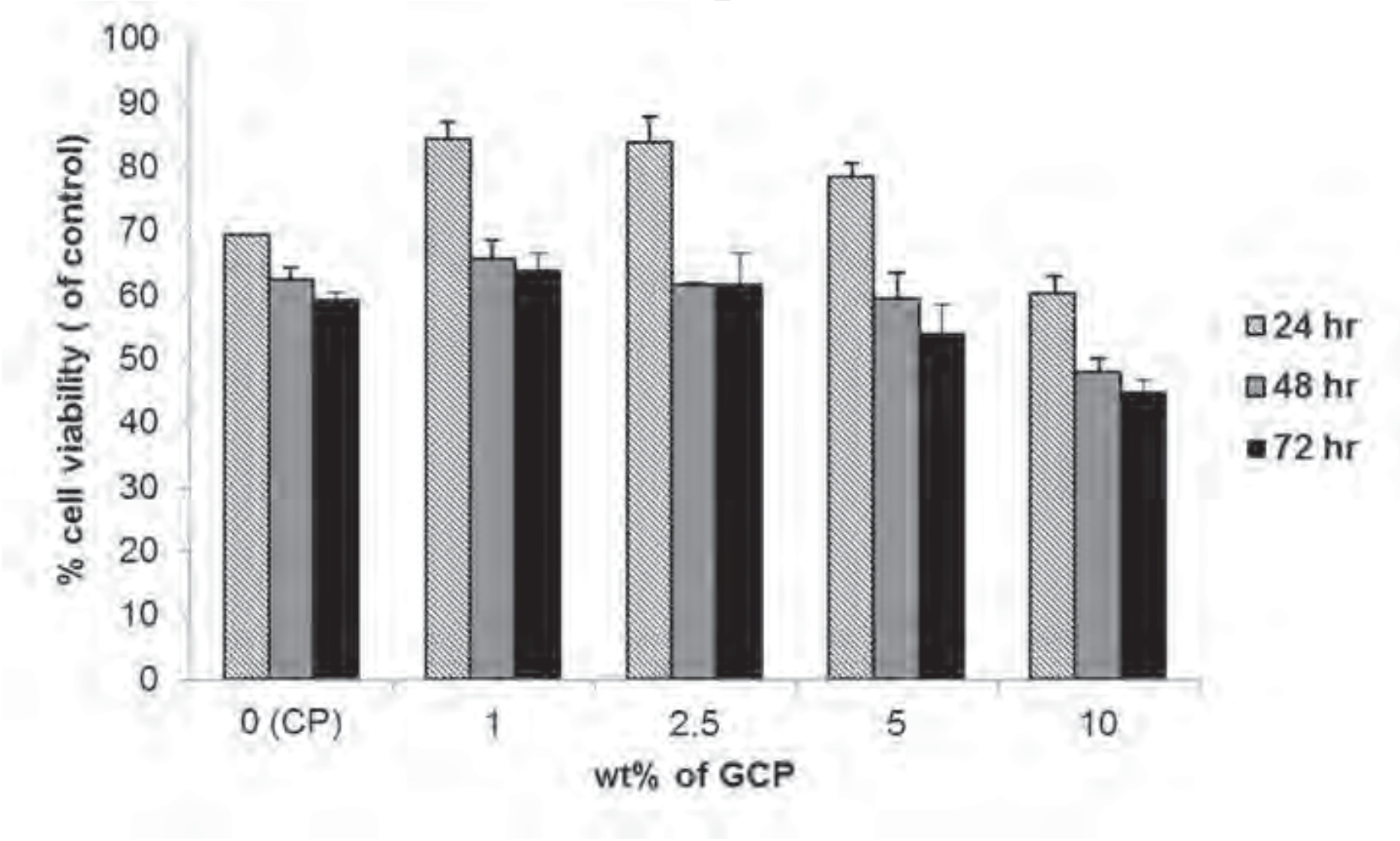
100
90
80
70
60
50
40
30
20
10
0
% cell viability (of control)
0 (CP)
1
2.5
5
10
wt% of GCP
24 hr
48 hr
72 hr

Figure(s)

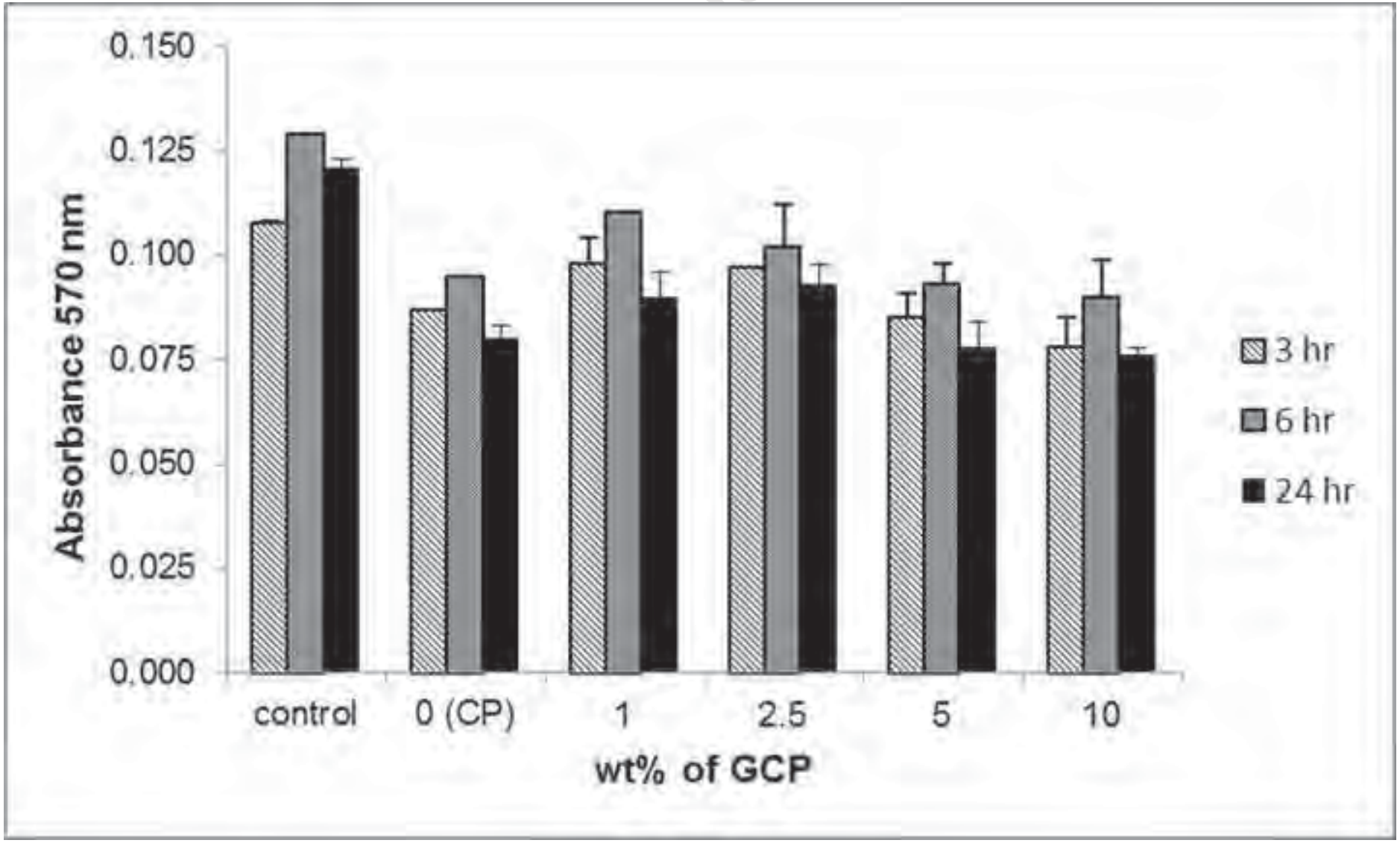
0.150
0.125
0.100
0.075
0.050
0.025
0.000
Absorbance 570 nm
control
0 (CP)
1
2.5
5
10
wt% of GCP
3 hr
6 hr
24 hr

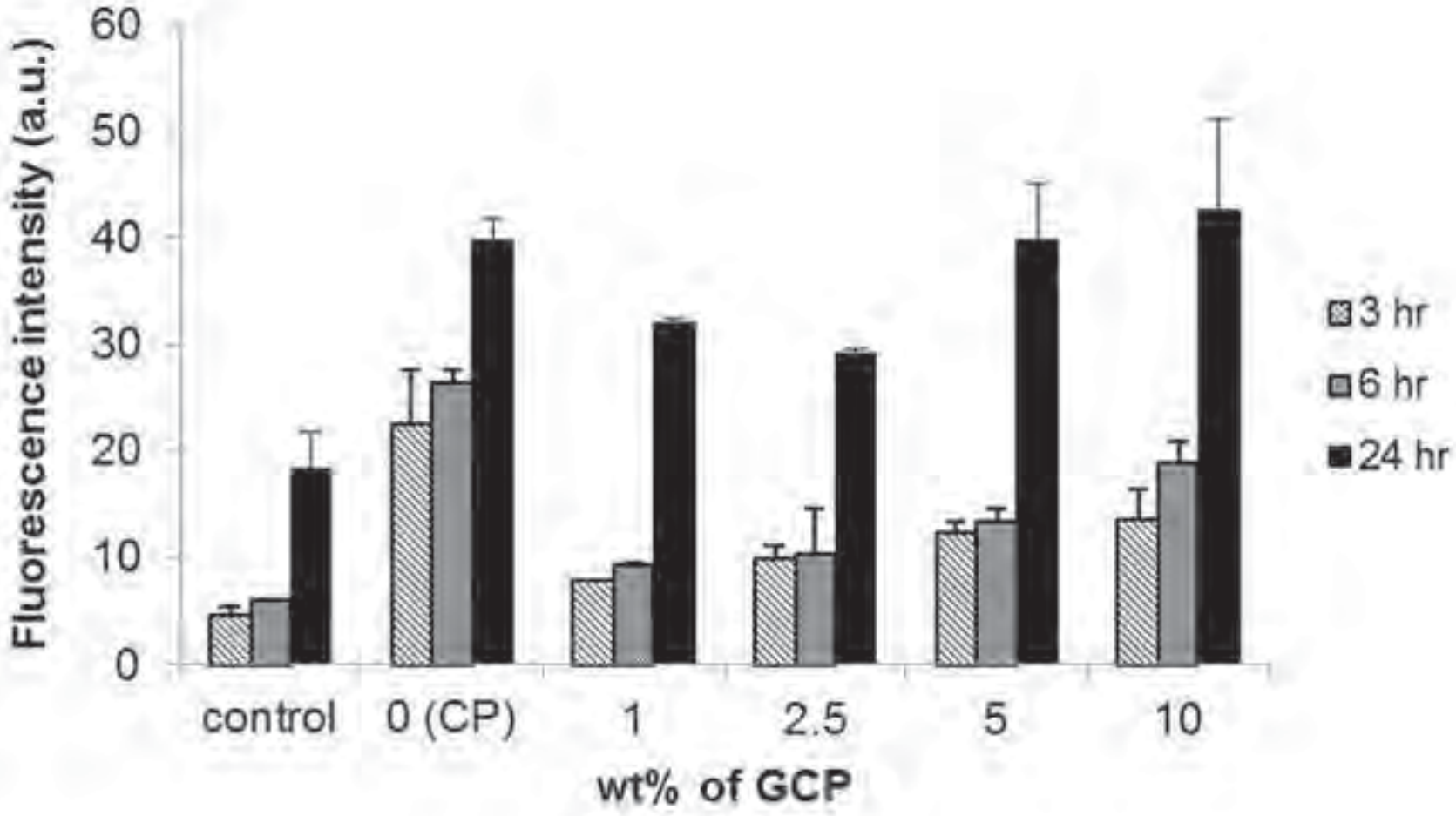
Fluorescence intensity (a.u.)
60
50
40
30
20
10
0
control
0 (CP)
1
2.5
5
10
wt% of GCP
3 hr
6 hr
24 hr

Figure(s)